Irradiation and DC yield potential of solar highways in the Netherlands

Carlotta Ferri

TU Delft

Irradiation and DC yield potential of solar highways in the Netherlands

by

Carlotta Ferri

to obtain the degree of Master of Science in Sustainable Energy Technology
at the Delft University of Technology,
to be defended publicly on Tuesday September 3, 2019 at 2:00 PM.

Student number:	4749723	
Project duration:	December 3, 2019 – August 27, 2019	
Thesis committee:	H. Ziar,	TU Delft, EEMCS, daily supervisor
	Dr. O. Isabella,	TU Delft, EEMCS, supervisor
	Prof. Dr. A. H. M. Smets,	TU Delft , EEMCS
	Dr. G. Agugiaro, TU Delft	Architecture and the Built Environment

This thesis is confidential and cannot be made public until August 26, 2021.

TU Delft

Preface

”I would put my money on the sun and solar energy. What a source of power! I hope we don’t have to wait until oil and coal run out before we tackle that.”

Thomas Edison, 1931

Abstract

With cities getting more densely populated and more energy-demanding, infrastructure integrated PV technology has gained more interest from researchers, companies and governmental institutions. Among the many urban surfaces that have been studied to be used to generate solar energy, roads are one of the most enticing but controversial as well. Questions regarding their feasibility and costs arise, such as if they can withstand traffic load or if they will ever be cheap enough to compete with conventional systems. However, it is first of all crucial to understanding if their energy potential will be sufficient to make solar road installations a reasonable investment to begin with.

As rooftop irradiation maps start to become the hotspot in the branch of solar energy modelling, the same attention should be directed to solar roads. This research aims to develop a modelling methodology to easily and quickly estimate the potential of solar roads and provide the first irradiation and DC yield potential map of solar highways in the Netherlands. The map could serve as a useful tool for advisory of research, private industry and governmental projects that helps to individuate optimal sites for solar road installation in the Netherlands.

The average irradiation along highways is found to be around 880 KWh/m^2/y, 35% less than the potential of an optimally tilted conventional PV installation in South Holland. The most irradiated highways result to be A31, A5 and A200, with average irradiation between 980 and 1000 KWh/m^2/y. The analysis of the sky view factor along the highways discloses that in most of the cases highways are in almost free horizon conditions. This makes them an appealing location for PV installations.

The DC yield potential of solar highways is obtained assuming three different technologies: monocrystalline silicon, polycrystalline silicon and CIGS. The energy output is modelled using a solar road-specific temperature model, which accounts for conductive heat exchange between the layers. The scenario of having the entire Dutch highways network renovated into solar roads is considered unrealistic. Therefore, a glueable solar road technology is assumed, similar to the one developed by the French company Wattway by Colas.

Solar highways can generate on average a DC yield of 138 kWh/m^2/y in the Netherlands if polycrystalline silicon is assumed. This value can increase up to 174 kWh/m^2/y if monocrystalline silicon technology is implemented. In total, covering the entire Dutch highways network with solar road modules could generate between 3.4 and 6.6 TWh/y of electricity. This could be used to power 36% of the national street lighting demand.

In addition to that, a model is developed that aims to address another compelling question regarding solar road feasibility: what is the impact of traffic? Two case studies are conducted on two of the four busiest roads in the Netherlands, the A12 and A16, based on real traffic data. It is found that traffic accounts for an average of 3% reduction of solar road irradiation potential, with a maximum reduction of 7% in particular locations, such as bridges and in the nearby of ramp roads. The value, comparable with inverter conversion losses, does not significantly impact on the output power but still needs to be taken into consideration when designing the PV system of a solar road.

The research presented here aims to spark the interest from the research, the industry and the government towards solar road applications. By giving a first estimate of the irradiation and DC yield potential of the whole Dutch highways network, this aims to act as a springboard for improvements and further development in solar road modelling.

Acknowledgment

After nine months of intense work, dedicated to producing the results presented in this report, there are many persons that need to be mentioned as they contributed in different ways to the success of this research project. First of all, I would like to mention Prof. Olindo Isabella, who introduced me to the topic and always provided me with the resources and contacts I needed at each step of the project, regardless of his very busy agenda. My gratitude goes also to my daily supervisor, Hesan Ziar, who has not only conducted my research through these nine months, but also supported me in each moment, empowering and encouraging me. It has been a pleasure to discuss with him the ideas and problems that I encountered while developing my thesis.

The whole PVMD group helped me to develop this project, by giving feedback during the group meetings or informal chats. In particular, I would like to mention Andres, who has always been available to provide me with all the help needed when it comes to PV system modelling, Martijn, who kindly shared his MATLAB skills to help me in the development of my ideas for the project, Gregory, who I thank for all the papers that he shared with me and for his commitment to getting in contact with Wattway, and last but not least Arturo, who helped me to move the first steps in the ArcGIS software. However, the daily support, that brought me to successfully finish my thesis, came from my office mates and dear friends Eliora, Leo, Sukanya, Rayen, Emilio, Ignacio and Maarten. I would like to thank them not only for the academic but also personal support that they always gave to me. I would also like to thank Mohamed for his precious help in handling and representing the massive quantity of data I had to deal with.

Without the precious collaboration with the Civil Engineering department, my project would not have been as interesting and exciting as it was. Therefore, I would like to thank Prof. Hans van Lint for accepting the collaboration between the PVMD group and the Department of Transport and Planning. A mention is also needed for Tìn, who provided for me the real traffic data that are at the base of the traffic shading model. I would like to thank him for his availability and commitment, but also for the feedback that he provided to my work.

I thank Stan Klerk for the relevant collaboration with TNO, which provided me with insight into the innovative and unique SolaRoad technology and measured data from the pilot site in Krommenie. I would also like to mention Pierre Trotobas from Wattway, who was available to answer my questions about the solar road technology developed by Colas and to meet Gregory and Stefaan on my behalf at Intersolar Munich. I also want to mention Gautham and thank him for having introduced me to the enticing concept of solar roads. It is thank to him if today I can present my thesis about the potential of solar highways in the Netherlands.

The experience in the board of the Energy Club opened many doors for me and made me know many inspiring persons that brought me where I am now. I would like to thank the whole board of 2018 that thought me the importance of team-work. In particular, I would like to mention Sukanya, who I discovered to be not only a precious start-up co-founder but also a dear friend, who always generously helped me throughout these months. Eveline also deserves my gratitude, especially for having helped me in finding a suitable third thesis committee member, Giorgio Agugiaro, who I would also like to thank for the availability and interest towards my research.

Eventually, I want to thank my family, that always sponsored me in all my initiatives, believing in my capabilities and passions. Also, the whole staff of Il Tartufo was like a family for me in Delft and I want to thank them for making me feel welcomed since the first day of work in the kitchen. Last but not least, all my friends, spread around the world, deserves my sincere gratitude for their endless support.

Contents

List of Figures

List of Tables

Abbrevations

All the technical abbreviations used in this report are listed here below and explained in the text when they are mentioned for the first time.

AM Air Mass

ASL Anti-Skid Layer

AoI Angle of Incidence

DC Direct Current

EV Electric Vehicles

IIPV Infrastructure Integrated Photo Voltaic

LED Light Emitting Diode

LiDAR Light Detection and Ranging or Laser Imaging Detection and Ranging

PVC Polyvinyl Chloride

PVF Polyvinyl Fluoride

PVNB Photo Voltaic on Noise Barrier

PV Photo Voltaic

SCF Sun Coverage Factor

STC Standard Test Conditions

SVF Sky View Factor

1 Introduction

In this chapter, the motivation of the research is introduced. It is explained how roads are recognized to have a high irradiation potential that has been left unused until now. The research objectives are listed and the methodology is explained. The questions that will be answered in details in the report are also indicated. Eventually, an outline of the structure and content of the report is provided.

1.1. Motivation of the research study

In the last decade infrastructure integrated PV (IIPV) technology has gained more interest from the side of both industry and research, as it is a promising technology for the realization of sustainable urban energy supply. In particular, it would support the increased power demand in the urban environment. In fact, according to Statistics Netherlands and the Ministry of Economic Affair, cities are getting more densely populated and energy demanding, especially on roads due to the increasing advent of electric vehicles (EVs) and the electrification of public transport system [10]. Additionally, decentralized power conversion through IIPV shows a potential economic benefit from the minimization of grid dependence and transmission losses for urban infrastructures like buildings, street lighting, etc [19].

What IIPV technology offers in addition to conventional photovoltaic systems is the resolution of the land constrain issue [26] [19]. In fact, providing power with a reasonable energy density from photovoltaic technology requires a great amount of land. In [26], the author claims that if the US should be entirely powered by photovoltaic energy, 181 m^2 per person of land area would need to be covered with photovoltaic modules, which corresponds on average to 0.6% of the US land area. Considering a total US area of 9.8 million km^2 it results in 54,000 km^2, a dimension comparable with the area of the Netherlands. This land competes with housing, transportation and even more with agriculture. In fact, optimal sites for photovoltaic systems installation are found to correspond with cultivated land since both the two sectors need an area that is potentially well-insolated, flat and horizon-free, has road adjacency to facilitate the transport of goods/materials but also the connection for workers and access for machinery/maintenance. Hence, a scaling up of photovoltaic power conversion could raise a future conflict between the agriculture and sustainable energy sector [32].

All this considered, the idea of integrating photovoltaic technology in already existing built-up surfaces becomes very enticing because no additional space is needed and only a limited infrastructure adjustment is required. According to A. S. Dezfooli et al. in [16], roads have a great irradiation potential, absorbing up to 40 MJ/m^2 daily and an interesting study of S. Najem in [50] already disclosed the correlation between cities' road network size and their solar potential. After [19], harvesting energy from solar roads would permit to maximize the utilization of land dedicated to transportation.

Roads are additionally a source of heat in the urban areas, contributing to the well-known effect of the urban heat island. According to C. Efthymiou et al. in [23], photovoltaic roads could reduce the urban surface temperature in comparison with conventional pavements due

to the fact that a share of light is reflected or converted into electricity. The study revealed that incorporating solar modules in the road surface, would allow a decrease of 5° on the road surface and of 3° in the ambient temperature.

In addition, considering that urban areas are responsible for 40% of the total CO2 emissions, different methods have already been approached to make the road construction sector more sustainable: bituminous asphalt containing waste material, solar asphalt and implementation of PV technology for electricity demand on streets [16].

The Netherlands Organisation for Applied Scientific Research (abbreviated to TNO from the Dutch name Nederlandse Organisatie voor Toegepast Natuurwetenschappelijk Onderzoek) claims that the Dutch road network, which accounts for around 135.000 km, can harvest enough electricity to power all the cars in the country with clean energy. The organization recognizes a great potential for solar roads linked with electric mobility (e-mobility) [66]. In fact, electric vehicles cannot be considered a revolution towards a sustainable product, unless they are powered with electricity generated from renewable sources. Solar roads would play a decisive part, providing clean power where it is needed. Additionally, this could become a great opportunity to revolutionize the transportation sector, including new smart functions in the road itself, such as sensors to collect traffic and temperature data, generation of variable road marking, integrated LED lights, wireless energy transfer to vehicles (inductive charging) and even automatic vehicle guidance [65].

The aim of this research project is to provide a first map of the Dutch highways network, which drafts the irradiation and DC yield potential of solar roads for three different potential PV technologies: monocrystalline silicon (mono c-Si), polycrystalline silicon (poly c-Si) and copper indium gallium selenide (CIGS). Additionally, for two highways a study of the traffic shading has been conducted and insightful information about the evaluation of traffic impact on solar roads output has been provided. Highways have been selected for this first research project due to the wide data availability. However, the same method can be applied to many other roads category.

The solar road map could serve for advisory and counselling of both the private industry and the government for future projects related to solar roads. The map is a useful tool for recognizing the optimal sites in terms of irradiation, traffic shading and the optimal technology in terms of DC output and costs. Additionally, the study provides a general overview of the feasibility of solar roads in the Netherlands and discloses the potential of this revolutionary technology.

1.2. Research objectives

The objective of this research project can be summarized in the following three points:

1. *Development of a method to estimate the irradiation and DC yield of solar highways in the Netherlands*: this objective will be achieved by modifying an existing irradiation and DC yield model for conventional PV systems to adapt it for solar roads simulation. This includes improving the accuracy of low altitude irradiation simulation, applying a more appropriate temperature model and introducing traffic shading. In the report the following research questions related to the methodology are answered:

   (a) How can roads be localized in the LiDAR data?

   (b) How can further correction factors be implemented in the irradiation model and what is the improvement achieved in terms of accuracy?

   (c) How can the irradiation and DC yield model be adapted to solar road technology simulation?

   (d) How can the model account for traffic shading?

2. *Evaluation of the model sensitivity*: the resolution of input data is tuned to analyze the deviation of the model results. Knowing the sensitivity of the model allows the method to be applied in situations when less data or computational power is available. In the report the following research questions related to the sensitivity of the model are answered:

(a) What is the loss of accuracy in the results if the azimuth resolution of the skyline profile is reduced?

(b) What is the potential gain in computational time?

(c) What is the loss of accuracy in the results if the relative density between the analyzed points is reduced?

3. *Evaluation of the irradiation and DC yield potential of solar highways in the Netherlands*: the model will be used to generate a map of the irradiation and DC yield potential of solar highways in the Netherlands, using GIS software. The information stored in the map will not only used to evaluate the potential of solar highways in different locations but also study how the surrounding affects the system output, for example, to analyze the actual impact of traffic on solar road irradiation and DC yield. In the report the following research questions related to the model outputs are answered:

   (a) What are the statistics (average, maximum, minimum and standard deviation) of annual irradiation potential for solar highways in the Netherlands?

   (b) What are the statistics (average, maximum, minimum and standard deviation) of annual DC yield potential for solar highways in the Netherlands?

   (c) What is the total DC yield potentially achievable with solar highways in the Netherlands?

   (d) What is the impact of traffic shading on the potential of solar highways in the Netherlands?

1.3. Report outline

Chapter 2 first gives an introduction about solar road technology and the state-of-the-art. It follows an explanation of the basic principles of PV system modelling with a focus on modelling methods for irradiation. The approach chosen for the research is then introduced, mentioning the reasons that make this method the most suitable for the purpose of the project.

Chapter 3 deepen into the modelling methods. The data used and the model inputs are further described. A sensitivity analysis of the approach is conducted, based on the model inputs, considering the possibility of limited data quality or computational power. Eventually, the developed method is validated, comparing the obtained results with the data measured at the existing TNO SolaRoad infrastructure in Krommenie, Amsterdam.

Chapter 4 focuses on the main changes made to the model in order to account for traffic shading and module temperature in a solar road. The traffic shading model is then applied to two the highways A12 and A16.

Chapter 5 the model results are reported. Different examples and case studies are conducted in order to evaluate the irradiation and DC yield model, evaluate the potential function of the map and compare the results with the output of conventional PV systems. The generated maps of irradiation and DC yield potential for solar highways in the Netherlands are depicted. The effect of traffic shading is analyzed and discussed, using two explanatory examples.

Chapter 6 summarizes the conclusions drawn and gives an overview of the research findings. Eventually, in Chapter 7 recommendations are provided for the continuation and improvement of the research.

2

Theoretical background

In this chapter, a brief history of methods to harvest energy from roads is given and some of the main designs studied or realized until now are briefly described. It follows an introduction about PV system modelling with a more in-depth description of the approach chosen for the purpose of this research.

2.1. Technology background

2.1.1. Insight in photovoltaic power conversion

To fully understand some concepts at the base of the research project here reported, an insight into some definitions related to photovoltaic (PV) systems is necessary:

- The working principle of solar cells is based on the so-called *photoelectric effect*, which consists of the generation of electrons from a material that has absorbed photons with an energy above a material-specific threshold. This causes the photovoltaic effect, which generates a potential difference at the junction of two different materials exposed to electromagnetic radiation.
- The term *irradiance*, often indicated with a capital I, refers to the power density at a certain point of the surface and is usually given in [W/m^2]. In this report, a capital G is used to indicate irradiance values.
- The above term should not be mistaken for the term *irradiation*, which is misleadingly often indicated with a capital I as well. This refers instead to the integration of the irradiance on a surface for an interval of time and it is given in energy unit, usually in [kWh/m^2].
- When it is referred to the *DC yield (output)*, it is meant the energy converted by a PV system in direct current or before the inverter or power conditioning.

2.1.2. Harvesting energy from roads

The first idea to harvest the solar energy concentrated on road surface through a so-called "solar asphalt" dates back to 1979 when its application has been seen in snow-melting systems in Switzerland (SERSO) [41]. One of the first Dutch projects related to solar energy harvesting from road surfaces was carried in 1998. A pipework was invented that was able to transport deep groundwater under the surface of a concrete road and harvest heat. The project was very successful and could potentially provide heat or cool for 100 family houses or equivalent in energy consumption for each road kilometre [33]. The project adopted the solar collectors concept and implement it in a road surface: in summer, the fluid circulates in the pipes beneath the road and collects heat. The heat is stored, for example in an insulated tank. In winter, the fluid is reheated and pumped back in the pipes below the road surface and can be used to defrost the street or to provide heating to the neighbouring buildings.

(a) Solar road concept developed by the american start-up Solar Roadways in 2006

(b) TNO SolaRoad concept, developed in 2011 and installed in Krommenie, Amsterdam, as fist pilot project

Figure 2.1: First solar road concepts based on PV technology

This concept is also recognized as a valid solution for the so-called urban heat island effect in cities since it decreases the temperature of roads and consequently the energy needed for cooling the surrounding. Additionally, heat can be stored for the cold months, providing clean energy [56].

After the Dutch Ministry of Transport announced the Road to the Future programme, more projects related to innovation in road constructions started. Among them, also hybrid systems ideas arose, where not only thermal but also electric energy is harvested from solar energy. Many projects recognized the potential of photovoltaic energy in street lighting. In [45] and [74], results showed that the solar-powered LED lighting system can be economically valuable because shorter transmission line needs to be installed in comparison with a grid-powered system. This reduces transmission losses and therefore the total power consumption, but decreases also material requirements for copper cables. An economic analysis showed that the payback period for the investment was only 1.1 years longer for solar-powered LEDs in comparison with grid powered LEDs [18]. A more innovative project, called EC-fics (Energy Conversion in a fully-integrated-clean-system), developed an integrated systems of solar-energised thermos-couple panels, enclosed in the asphalted road, windmills installed on top of light masts and photovoltaic panels installed on the top of a perimeter noise-reducing biomass collector [33].

In [33], [53], [69] and many more, photovoltaic technologies are further included in the road environment and installed on motorways noise barriers to provide energy for street lighting, signals and/or to the power grid. The first project was realized in Switzerland in 1989 and now the application of PV on noise barriers (PVNBs) has greatly increased all around Europe. After [51], central Europe could potentially provide 680 GWh per year (still only 0.02% of the electricity generation in Europe in 2017 [7]), going hand in hand with the increasing legislation on sound protection from motorways and railways.

What is revolutionary in PVNBs is that no additional land is required and installation costs can be shared with the investment costs for the sound barrier. New technologies such as bifacial modules or hydrogenated amorphous silicon (a-Si:H) could have a big potential in this application, as confirmed in [31], where a bifacial PVNB was fabricated and tested.

However, all the solutions considered above are restricted to either thermal-energy or low-power density electricity generation. These technologies cannot, therefore, be applied on a large scale but can only supply in situ consumption [19]. The increasing demand of power supply also along the roads, driven by the advent of EVs and the necessity of a transition of the public transport to sustainable energy sources, brought the idea of more efficient use of road surfaces.

In 2006 a U.S. start-up Solar Roadways started developing modular solar roads with integrated PV cells and LED sources (Figure 2.1a). The solar road is able to convert power and to emit light in the form of road signage and street lines [62]. It also incorporates a heating system in the surface layer that can adjust the road temperature. In a middle layer, the electronic components are encapsulated, such as microprocessors that control heating, LEDs, sensors and communication circuit between them [62] [56].

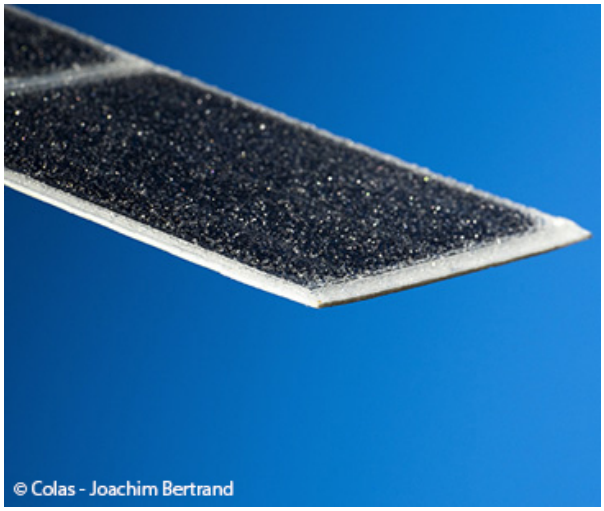

Figure 2.2: Wattay solar road concept developed by Colas in 2015. The thickness of the solar road modules is claimed to be less than 1 cm.

A different concept has been launched by TNO in 2011 (Figure 2.1b. It was the first solar road pilot project in the Netherlands, called SolaRoad, and consisted of a 70 m cycle path in Krommenie, North-Holland, built with precast concrete block, upon which a polycrystalline silicon module is installed [66]. The pilot project harvested a cumulative annual energy yield of around 78 kWh/m^2 [19]. However, based on the best performing modules, the energy yield expectation for the SolaRoad is set between 85 and 90 kWh/m^2. This value is smaller than the electricity yield obtained by other infrastructure integrated PV (IIPV) systems, but it remains appealing because it makes use of the area with PV potential otherwise left unused.

In 2015 the French construction company Colas, in collaboration with the National Institute for Solar Energy, unveiled its innovative product Wattway (Figure 2.2). The technology consists in modular PV cells encapsulated in a resin that can stand the weight of a truck with less than 10 millimetres thickness. Different than the Roadways and the first TNO concept, Wattway modules can be directly glued on the road surface. Therefore, it can be applied to already existing roads without the need for additional civil work. A modular pack of Wattway has a peak power of 345 W$_p$ and show a conversion efficiency up to 15%. In 2016, the company started to launch many trials sections in France, but also worldwide, mainly on parking slots, to test the first prototypes. Eventually, in December 2017, the first world's solar road was inaugurated in the French village of Tourouvre. It counts 1 km covered by 2,800 m^2 Wattway modules and it is said to generate enough electricity to power up to 5,000 average French households [70].

In their work, V. Prasanth et al. presented a study case of the highway A12, which connects the Hague to Arnhem, where inductive EVs power charging together with renewable energy generation is analyzed. Interesting part of this project is the double employment of photovoltaic technologies: on the noise barriers and on the emergency lane. The latter is built as TNO SolaRoad with an estimated conversion efficiency of 9,69%. In the result of the modelled study case, it is observed that the photovoltaic modules installed on the acoustic-walls do not convert enough power (less than 10% of the total energy output of solar energy sources), while the SolaRoad contributes for the highest share of the hybrid system in spring and summer, overtaken by wind power sources in autumn and winter [69].

Other promising uses of roads infrastructure for energy harvesting are roadside PV deployment and Solar Arch. The idea of Solar Arc is to integrate PV panels into arches over highways. In the work of Sharma and Harinarayana, the potential of two highways in India has been analyzed, discovering that the Solar Arches can harvest around 80 kWh/m^2 every year [18].

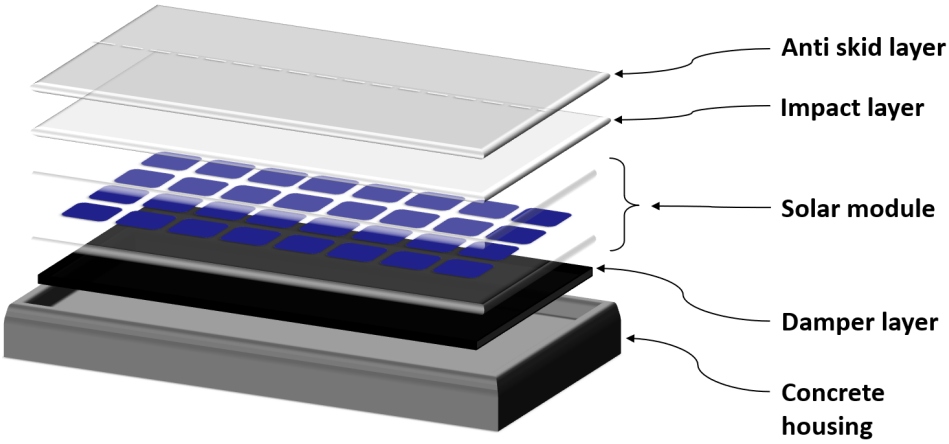

Figure 2.3: Sketch of a TNO SolaRoad section

2.1.3. Solar roads design

The first issue that solar roads implementing photovoltaic technology face is the necessity of innovative design since they need to meet requirements for both pavement structures and photovoltaic modules. Roads surfaces need to support traffic load, rutting (caused by vehicles tires), fatigue cracking, rainwater drainage flow and skid forces [16]. On the other hand, photovoltaic modules require minimization of the solar cells shading, strong cells interconnection, weatherproof structure and diodes to avoid reverse current [52]. Additionally, solar roads need to be designed to withstand snow accumulation and removal, salt-based winter road maintenance and freezing in cold regions, while overheating should be considered in the hotter climates and at the same time they need to be modular and easy to maintain, have a low weight to facilitate testing and installation and require readily available components and materials to sink the costs [52]. Therefore, a new design needs to be studied to optimize technology integration in the infrastructure.

Many projects mentioned in Section 2.1.2 consider the fabrication of a new building concept that should replace the conventional asphalt road. In the Krommerie project, TNO built its SolaRoad laying on the ground prefabricated elements. These are composed of a concrete housing, that hosts (starting from the bottom) a damping layer, a bottom glass, the poly c-Si solar cells, a top glass and a transparent anti-skid layer on the top [66] [19], as represented in Figure 2.3.

In this design, the major variation from conventional rooftop PV panels design is the presence of the anti-skid layer, which provides adequate friction on the road surface, and the damping layer, which protects the module from mechanical stress [19].

In [52] a new pavement design structure is studied to withstand high traffic load and incorporate photovoltaic cells. Cantilevered glass panes, already very common in floors design, is suggested as a surface layer where vehicles can drive on. This consists of multiple glass layers so that if one fails the others will still support the design load. Below it, an optical layer of multiple fibreglass is placed and several cut-outs in the structure are used to host the cells. Cell interconnection is also improved in resistance, replacing the traditional thin-coated ribbon with an insulated wired.

However, it is not realistic to expect all the Dutch roads to be rebuilt as following the construction procedure applied in the above-mentioned designs. What is instead more probable to see, employed in the near future on a larger scale, is a PV technology that can be directly applied on the asphalt surface.

In [16], two different prototypes of solar road elements are developed: a solar panel and a solar pavement. The solar panel consists of three substructures. From the top to the bottom: a transparent polycarbonate sheet (Plexiglas), rough enough to provide skid and slipping resistance, monocrystalline silicon solar cells placed in a rubber layer, and eventually aluminium is used to keep the layers together. While the solar panel is thought to be

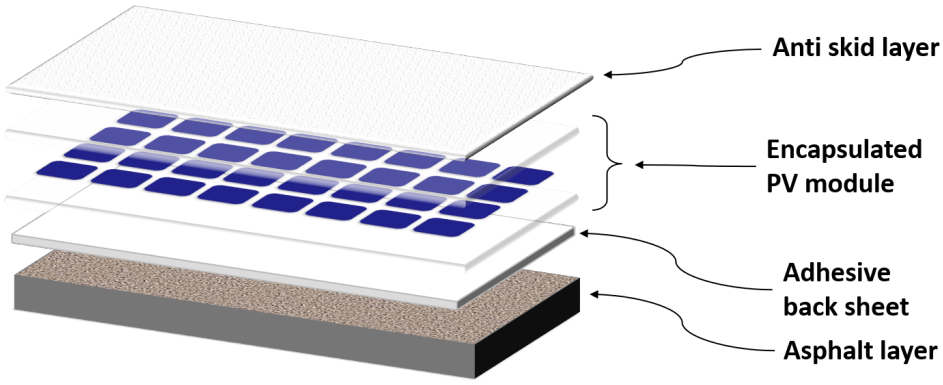

Figure 2.4: Sketch of the concept applied in this project, inspired by the Wattway solar road technology

embedded in asphalt, the solar pavement needs an asphalt layer, upon which two rubber layers are placed: the bottom one containing the electric system and the top one the solar cells. On the top, a surface porous layer protects the cells and drain the water. The two solar road solutions are tested for skid, loading and fatigue resistance, drainage, and power conversion. The solar pavement performs better than the solar panel in all the structural tests, but its power conversion efficiency (PCE) is more affected by the encapsulation method. In fact, solar cells below a Plexiglas sheet (solar panel) showed a PCE reduction of 26%, while cells under rubber layers (solar pavements) performed with a 50% lower efficiency [16]. Unfortunately, these design still do not meet all the requirements to be implemented in a road construction project and further research is therefore needed. For this reason, in this research a different usage of the technology is considered, assuming a concept closer to the one used for Wattway.

In the solar road developed by Colas, each panel contains 15x15 cm^2 poly c-Si cells, embedded in a multilayer substrate made of resins and polymers of 7 mm thick. This layer has been studied to be translucent enough to allow sunlight to pass through, and resistant enough to withstand heavy traffic. The surface meets the standard of skid-resistance of conventional asphalt and has been filed in many patents.

Figure 2.4 shows a guess of how the technology could be represented, based on literature research and informal exchange of information with the company.

It is beyond the scope of this research to evaluate the feasibility of this technical solution and the detailed explanation of the choice of material and construction method.

2.1.4. Photovoltaic technology in solar roads

Besides the structural and electrical design of solar roads, the choice of the most suitable photovoltaic technology also plays a crucial role. The options go from monocrystalline and polycrystalline silicon cells to thin-film technology and more innovative solar cells [52].

No research about the implementation of different photovoltaic technologies in solar roads can be found. Only in [19] a theoretical model is utilized to estimate the module identity factor (MIF) of polycrystalline silicon, monocrystalline silicon and CIGS. The model assumes a system with the same composition, optical and thermal characteristics as the TNO SolaRoad in Krommenie and evaluates its performance in different conditions of temperature and irradiance.

The MIF is the proportion of actually available energy yield to the estimated one and can be obtained by the ratio of energy yield considering varying efficiency on energy yield with constant (rated) conversion efficiency. Consequently, the lower the MIF value, the lower the technology performance due to thermally and irradiance losses.

Among the analysed technologies, CIGS technology shows the highest efficiency reduction in all the simulated locations, even if the thermal coefficient chosen was slightly better than the one for polycrystalline silicon. This aspect of thin-film technology is confirmed also in the study of [37], where it results that CIGS implementation for surfaces exposed to a vast amount of irradiation is critical. According to [19] the best performing solution were

Figure 2.5: TNO SolaRoad pilot site in Krommenie (July 2019)

monocrystalline cells, due to higher conversion efficiency and a better thermal coefficient.

2.1.5. Solar roads state of the art

The first SolaRoad pilot project was opened in 2014 on the bike road next to the N203, in Krommenie (Figure 2.5). The SolaRoad section was initially 70 meters long and 1,7 meter wide. However, during the pilot, multiple versions of the solar pavement have been added. Different coating technologies, solar module designs and cell types have been tested. Therefore the SolaRoad is now 90 meters long and 1,7 meter wide.

The SolaRoad, which is connected to the grid, was expected to deliver between 50 and 70 $kWh/m^2/y$ of energy yield. However, the system overperformed after the first year of operation and 73 $kWh/m^2/y$ were produced. Two years after, 93 $kWh/m^2/y$ were achieved by the improved version of the system. The application of thin-film modules in the last version of the solar road delivered until now lower energy output of 41 $kWh/m^2/y$.

With time, the yield decreased back into the expected range, due to transmittance losses of the top layer. It has been observed that this layer can be strongly impacted by the weather condition, which caused the delamination of the road structure in many points of the road (Figure 2.6). However, an improved version has already been developed [63].

After the success of the first trial, many other projects started in the Netherlands and in France. The latest ones are the 100 m bus lane and the 50 m parallel road in Spijkenisse and Haarlemmermeer, respectively, both in the Netherlands. Opened on the 7th of March 2019, these projects represent the first application of the TNO SolaRoad technology under heavy traffic conditions. The first observations revealed damages to the road surfaces and deformations after a week after the opening. These were probably caused by stresses of heavy traffic [63]. Based on these results, the following projects will take a step back to light traffic in order to further improve the technology.

In these terms, the story of Wattways can provide a better insight into the application of solar roads in vehicles traffic conditions. Starting from October 2015, already more than 40 trial sites have seen the Wattway solar road technology being applied not only in France but

Figure 2.6: Soiling and delamination of the top layer occurred in the SolaRoad pilot site in Krommenie (July 2019)

Figure 2.7: The Wattway pilot route in Tourouvre-au-Perche, Normandy, France (Photograph: Christophe Petit Tesson/EPA)

worldwide in order to test the technology in real conditions. The most relevant is the first installation in the town of Tourouvre, Figure 2.7, where in December 2016, 1 km of a road lane has been covered with 2,800 m^2 of Wattway PV modules.

The initial forecasts foresaw 790 kWh/d (103 kWh/y/m^2) of energy conversion, enough to power the demand of 3-5,000 people. However, after the first year, the effective energy output resulted to be only 50% of the expected one (149,459 kWh/y or 53 kWh/y/m^2) and in the second year it dropped to 25% (78,397 KWh/y or 28 kWh/y/m^2). In July 2019, the cumulative energy generated accounts for 37,900 kWh [17].

In the Netherlands, another trial has been conducted by BAM Infra on the N401 near Kockengen, in the region of Utrecht. A 20 m lane with an area of 50 m^2 has been covered with 48 Wattway modules in May 2018. The test should have run for 2 years, but BAM Infra decided to end the test after the first year, after having collected enough information. In this year of trial, the electricity output resulted to be 2,200 kWh/y (44 kWh/y/m^2) [28].

A better result for the solar road technology has been reported in the site of Ecommoy, a village in Pays de la Loire region, France. Inaugurated on June 2018, the solar road was designed to meet 30 % of the electricity need of the town hall and to supply power to the electric vehicles for car-sharing. Since April 2018, the road has generated 3720 kWh (77.5 kWh/m^2/y) and the goal has been almost reached. In fact, Wattway was able to supply one-fourth of the town hall consumption and providing electricity for the EV charging station.

Besides energy conversion efficiency, other characteristics of the Wattway technology have been analyzed. Through camera research, the reaction of the drivers has been observed and no abnormal behaviour has been registered by cars driving on the solar road section. However, the module pavement has been found to increase the noise generated by traffic of about 1.3 dB(A) [1]. The consideration of this aspect will be decisive in case of application in urban environments. In addition to that, it has been measured as a decrease in skid resistance with time. The road surface became smoother, reducing vehicles grip. This aspect is of great importance to ensure road safety and accounts for one of the reasons why the duration of the trial has been shortened. Another issue is the wear out of the coating layer after winter.

Giving a brief look at the involved costs, solar roads are still far from being competitive with conventional modules. The Wattway pilot project needed a € 5 million state subsidy to be realized, not considering the costs for past and still ongoing R&D. Solar road costs about 17€/kW in comparison with 1.3€/kW for a traditional solar installation [57]. Nevertheless, the company aims to make the technology price comparable with conventional modules, eventually (Personal communication by Pierre Trotobas, July 2019 at Intersolar Munich, Munich, Germany).

To recap, to the solar road technology has been recognized a great potential but it still needs to be further developed and tested for use on busy motorways. Additionally, the cost of materials and fabrication will need to considerably drop in order to be competitive in the market and for the technology to show a short payback time. In the future, Wattway by Colas will focus on improving the robustness and the conversion efficiency of their product.

However, Etienne Gaudin, managing director at Wattway, underlines that the choice of the location is critical when installing solar roads. Since it is not possible to adjust the module to the optimal tilt and orientation, an accurate study of the most suitable location needs to be conducted. The production of Wattway modules has been observed to vary from 40 to 120 kWh/y/m^2 in different sites. At this point, this research becomes an important tool for companies and for the government to conduct a preliminary study of potential sites for solar roads in the Netherlands.

2.2. PV system modelling background

2.2.1. Conventional modelling of irradiation and power output

With the development of building added photovoltaics (BAPV) and successively IIPV, numerous software tools and models have been developed to estimate the solar irradiation and energy output potential not only on roofs, but also of facades, and many other urban surfaces. To give an insight into conventional PV system modelling approaches, the most relevant input and equations are here summarized.

The first variable that influences the output of a PV system is undoubtedly the weather conditions, which limit the solar irradiance of a specific location. The irradiance is defined as the power density of the incident light at a certain point of a surface, measured in [W/m^2] [20]. The total solar irradiance, commonly addressed as global horizontal (GHI), is generally divided into two components: the direct normal (DNI) and the diffuse horizontal irradiance (DHI).

The DNI indicates the direct beam of the sunlight. With beam, it is meant a 5° field of view concentric around the Sun [58]. It is normally measured with a pyrheliometer, an instrument with a cylindrical shape that follows the sun with a solar tracking system to measure the direct beam solar irradiance. From a narrow window, the light enters the instrument, where commonly a thermopile converts the heat into an electrical signal and later into W/m^2.

The GHI is instead the amount of irradiance that reaches a horizontal surface. The most common instrument to measure it is the pyranometer, which has a hemispherical measurement angle. The response of a pyranometer is directly proportional with the cosine of the light beam incident angle. If it cannot be measured, the GHI can be indirectly obtained from the other irradiance components, as explained in Equation 2.1:

[1] An increase of 1.3 dB(A) means that the final value is $10^{1.3/10}$ or 1.35 times larger than the initial one.

$$GHI = DHI + DNI * cos(\theta_Z) \tag{2.1}$$

where θ_Z the zenith angle, defined as the angular distance between the zenith and the sun position in the projected skydome. Eventually, the DHI is defined as the irradiance on a horizontal terrestrial surface that has been scattered or diffused in the atmosphere. It can be measured with a pyranometer where the direct light beam is artificially blocked.

Another important aspect to consider about light is its spectrum. This is influenced by several atmospheric factors and, among them, water vapour and CO_2 are recognized to have the largest absorption bands. This means that a concentration of these two molecules variates the spectral component of the incident light on the module. In extreme conditions, this can affect the conversion efficiency of the system.

Air temperature needs to be considered in a PV system model since the ambient air, through convective heat exchange, tends to cool down the modules, positively impacting on their performance. Wind speed, precipitation and air pressure are also commonly included in a PV system thermal model.

To model the actual irradiance that reaches the plane of array (POA), diverse methods are applied to the different components. They are depicted in a simplified manner in Figure 2.8.

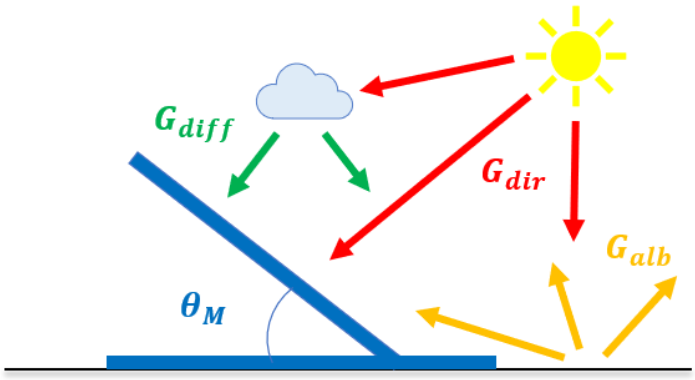

Figure 2.8: Irradiance components on a POA

The POA direct beam, hereafter referred to as G_M^{dir}, is obtained from the DNI and the angle of incidence (AoI). A shading factor (SF) can be also implemented as shown in Equation 2.2. It takes into consideration the surrounding objects and varies from 0 when the sun is shaded by an obstacle on the horizon to 1 when there is no shading.

$$G_M^{dir} = DNI * cos(AoI) * SF \tag{2.2}$$

The AoI depends on the altitude (a_S) and azimuth (A_S) of the Sun (the position of the Sun in the projected sky dome), and on the module orientation (A_M) and tilt (θ_M). It can be obtained as shown in Equation 2.3 and illustrated in Figure 2.9.

$$cos(AoI) = cos(a_M) * cos(a_S) * cos(A_M - A_S) + sin(a_M) * sin(a_S) \tag{2.3}$$

where a_M and A_M are the coordinates of the module normal direction projected in the skydome, and a_M=90°-θ_M.

The POA ground reflected irradiance G_M^{alb} considers the reflectance of the surrounding ground surface and the reduced incident light due to the module tilt, as expressed in Equation 2.4 and 2.5.

$$G_M^{alb} = GHI * \alpha * (1 - SVF_M) \tag{2.4}$$

$$SVF_M = \frac{1 + cos(\theta_M)}{2} \tag{2.5}$$

where α is called albedo, the fraction of the GHI that is reflected by the ground, and SVF_M is the sky view factor (SVF) considering only the module tilt as reduction factor of the sky visibility,

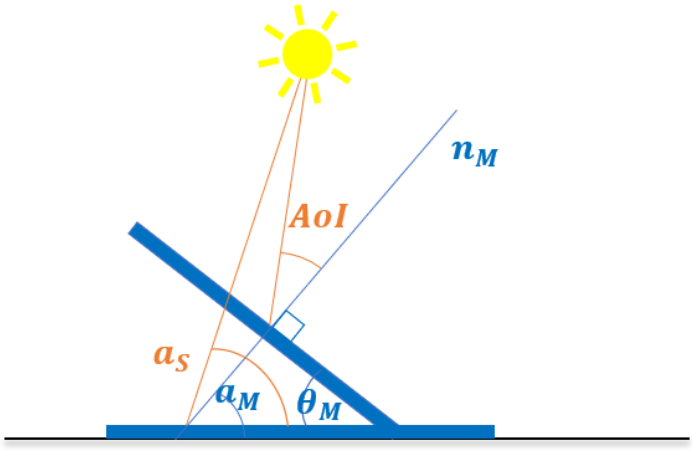

Figure 2.9: Angle of incident on a POA, with n_M the normal to the POA

which means in a so-called situation of free horizon. In a more realistic implementation of the model, the SVF describes the complex skyline profile in a specific location. It varies from 0 when the surrounding objects completely cover the sky to 1 when there is a situation of complete free horizon. Both of these two extreme values are less likely to be found in real measurements. Therefore, the SVF mostly lies in between. In a different way than the SF, the SVF does not depend on the time and the position of the sun but on the geometry of the skyline solely. This factor will be discussed more in details in Section 3.4.

The POA diffuse irradiance G_M^{diff} can be further divided into an isotropic component (the irradiance from the skydome), a circumsolar diffuse component (the scattered irradiance concentrated immediately around the Sun) and a horizon brightening component. There are several models that consider one or more of these components: the isotropic and the Sandia sky diffuse model [58], and the Hay and Davies sky diffuse model [35], further implemented in the Reindl model [25], where an additional term is accounted for the horizon brightening, otherwise excluded. A different approach is followed by Perez [59] in a more complex model that utilizes empirical coefficients instead of diversifying the three diffuse irradiance components. Finally, shading of the array, soiling effect and increased reflection losses need to be considered.

Most of the irradiation potential models are based on obtaining the hourly irradiance received by the POA, taking into consideration the light intensity, its distribution in the sky projection, the module tilt and orientation, and the skyline profile of the surrounding [30]. By integrating the hourly irradiance for one year, the annual irradiation is then obtained for a specific location.

The models utilize the sun path projection and Digital Surface Models (DSM) to obtain the shading profile of the objects that surround the examined point or surface through the methods developed in [60], [39] and [40]. Additionally, meteorological data, observed with an hourly frequency in the location are required in order to generate the decomposition model with the main three components of solar irradiance. From the DHI and DNI values, the transposition model generates the POA irradiance as a sum of the three contributions [20], as it is shown in Equation 2.6:

$$G_M^{tot} = G_M^{dir} + G_M^{diff} + G_M^{alb} \tag{2.6}$$

The hourly irradiance values are then further inserted in a thermal and electrical model to obtain the energy output potential. Thermal models go from a simple steady-state approach, which considers the nominal operating cell temperature (NOCT) as constant in time, to the Duffie-Beckman model until the more complex fluid dynamic model, based on a thermal energy balance between the module and the ambient temperature [20]. Electrical models mainly consider the efficiency curve of the inverter. The Sandia National Laboratory developed an empirical equation that models the relationship between the DC input and AC output of a

PV system inverter [24].

As it can be noticed, this modelling approach consists of repetitive expensive calculations and, nevertheless, a high amount of meteorological data from the installation site. These are not always available and limit therefore the potential of PV system modelling. Additionally, the wider the area that it is necessary to consider in the model, the more input data become necessary.

In the particular case of research among solar road potential in the Netherlands, considered the extent of the studied surface and the heterogeneity of the national weather conditions, a time and resource-efficient approach is determinant. When the model aims to consider a wider area that is not a single location anymore, the above-mentioned approaches become very inefficient. Therefore, a different modelling method has been considered for the purpose of this research project.

2.2.2. Simplified irradiation model

In [13], a new modelling approach is developed by A. Calcabrini et al., based on the fact that weather conditions are similar from one year to each other. Hence, it is reasonable to replace weather data with climate data to estimate the annual irradiation on a POA. In fact, climate data are obtained from a several years evaluation of weather data, which instead describe the weather of a single year.

If the meteorological inputs are fixed, the irradiance of a surface is mainly dependent on the surrounding shadowing obstacles. Hence, the simplified model obtains the annual irradiation at a given location using only two indicators that depend on the skyline profile: the sky view factor (SVF) and the sun coverage factor (SCF).

As already introduced, the SVF is defined as the ratio of the radiant flux collected by the surface from the visible portion of the sky, to the one that the surface would receive in free horizon conditions [36], i.e. it represents the portion of the sky in which the diffuse radiation from the Sun is not blocked by surrounding objects or decreased by the module tilt itself, and reaches the POA, approximated to its array's central point [20]. The geometrical parameter can be obtained from a projection of the skyline profile as explained further in Chapter 3.4.

However, a method solely based on SVF cannot offer meaningful results, since only the diffuse isotropic and the ground reflected irradiance can be represented [61]. Therefore, it is necessary to introduce a second factor. The SCF is defined in [13] as "the ratio between [the] time that the sun is behind the module or blocked by the skyline per year and the annual sunshine duration at the same location with a clear horizon". This modelling approach differs from the aforementioned ones because of this factor, as it is not based on irradiance input. In fact, the SCF does not depend on the light intensity, but only on the amount of time that the sun is actually covered by the skyline profile of the surrounding. The SCF becomes 0 if the horizon is completely free from objects and 1 if the sky view is completely blocked. To balance the accuracy loss of this method, the factor is very easy and fast to obtain by simply comparing the skyline profile and the sun path projected on the same skydome.

In [13] the SVF and SCF are introduced in the irradiation model, respectively, by linear and cubic functions. The correlation between these indicators and the annual irradiation has been empirically obtained from simulations on both real and synthetic skyline profiles. The annual sum of the simulated isotropic diffuse and albedo components, referred as I_Y^{SVF} is plotted against the corresponding skyline profiles' SVFs, while the annual sum of the direct and circumsolar components I_Y^{SCF} is compared with the SCFs of the respective skyline profiles. The coefficients that describe the curve fitting are valid for a specific module tilt angle and orientation inside a definite climate region.

Eventually, the final annual irradiation I_Y can be expressed in Equation 2.7 with the use of these empirical coefficients c_1,...,c_5:

$$I_Y = I_Y^{SVF} + I_Y^{SCF} \tag{2.7}$$

where,

$$I_Y^{SVF} = (c_4 + c_5 * \alpha_{gnd}) * SVF \tag{2.8}$$

$$I_Y^{SCF} = \sum_{i=1}^{3} c_i * (1 - SCF^i) \tag{2.9}$$

It is important to mention that the correlation coefficients do not include the ground albedo α_{gnd}, which can be introduced in Equation 2.8. The albedo coefficient is equal to 0 when the ground surface is black, while it is 1 if the ground is completely reflective. Different values for this coefficient were defined depending on the mounting ground material beneath the module [58].

Additionally, from [13] it can be stated that when the sky view is completely obstructed the estimated annual irradiation results to be zero, whereas, in a condition of the free horizon, it is given by

$$I_{Y(max)} = \sum_{i=1}^{4} c_i \tag{2.10}$$

2.2.3. Simplified DC yield model

Once the annual irradiation potential of a system is known, its operative efficiency needs to be calculated to obtain the annual DC yield output. The operative efficiency of a PV system is generally lower than the conversion efficiency of the single module because it is affected by module temperature and irradiance level.

Even if temperature and irradiance vary with time, the variation of the performance ratio for PV systems generally remains below 10% throughout the year [14]. Therefore, the method proposed for the irradiation model can be applied for a DC yield model as well. This results in an annual DC yield output that can be obtained from Equation 2.11.

$$E_Y = E_Y^{SCF} + E_Y^{SVF} \tag{2.11}$$

Where

$$E_Y^{SVF} = (d_4 + d_5 * \alpha_{gnd}) * SVF \tag{2.12}$$

$$E_Y^{SCF} = \sum_{i=1}^{3} d_i * (1 - SCF^i) \tag{2.13}$$

The DC yield coefficients $d_1, \ldots, d_5$ are valid for a specific PV module type and tilt. This represents a limitation in the application of this model to generate an energy potential map in urban areas, where the tilt angles and orientation significantly vary. Instead, this approach results to be highly suitable for estimating the potential of solar roads, where the tilt angle is approximated to be zero everywhere and one single module type is considered.

3

Methods for modelling irradiation and power output

In this chapter, the modifications applied to the irradiation model, in order to improve its results for the case of 0° tilted modules is presented. First, the model inputs are introduced and described, then the methods to process the given inputs are explained. A sensitivity analysis of the model, based on the input data resolution is conducted and the results are presented. Eventually, a comparison with measured data at the TNO SolaRoad pilot project in Krommenie is used to validate the irradiation model.

3.1. The analemma

The position of the Sun in the projected skydome throughout the year can be depicted in a so-called analemma. It represents the position of the sun for each hour of the day, indicated by azimuth and altitude, projected in a 90°x360° matrix.

In Figure 3.1 the analemma with a resolution of one hour is depicted. The analemma shows the number of hours throughout the year in which the sun can be found in a certain azimuth and altitude of the projected skydome. As the input of the irradiation model, the analemma here represented will be further improved to increase the accuracy of the model.

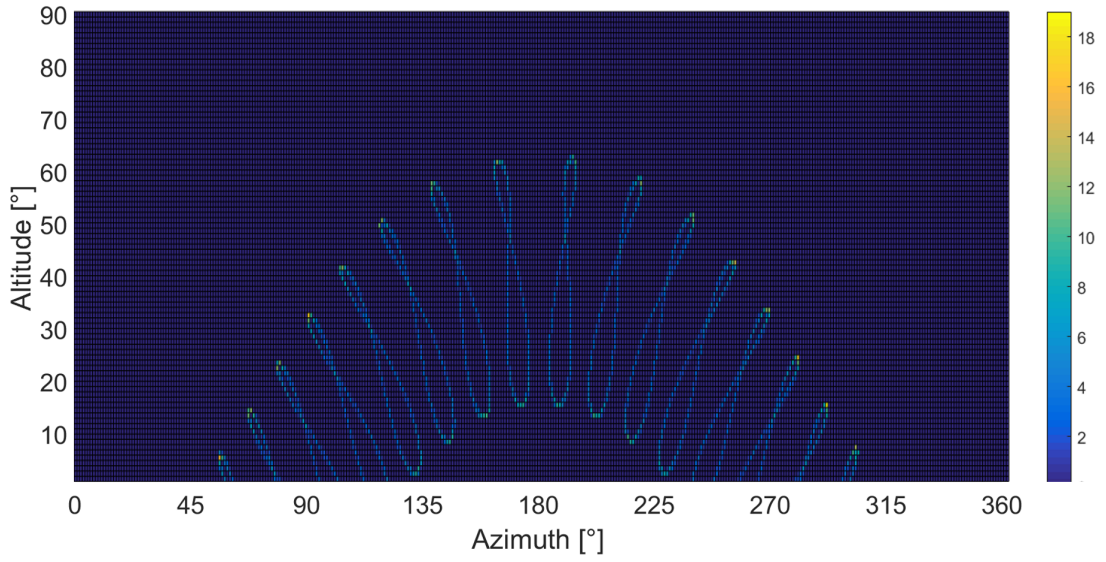

Figure 3.1: The cumulative time [h] in which the sun shines throughout the year

3.1.1. The optical air mass correction factor

In [13], the author explicitly mentions that in the coefficients-based method "the SCF is not an irradiance-weighted parameter - that is, blocking the sun one hour in the morning and blocking the sun one hour at midday contribute in the same amount to reduce the SCF value". In some cases, this can cause a weak correlation with the hourly irradiation values.

One of the possible ways to improve this correlation is with the introduction of the concept of optical air mass (AM), usually expressed in [kg/m^2]. The AM is defined as the ratio of an actual path length that the Sun has to travel through the Earth atmosphere to the minimal possible distance, which is the case of the sunlight passing the atmosphere when the Sun is at its zenith [20]. In this case, the optical air mass is called the air mass 1 (AM1). With the variation of the angle θ_Z (defined as the difference between the zenith and the Sun altitude), the AM can be obtained from Equation 3.1.

$$AM := \frac{1}{\cos\theta} \tag{3.1}$$

In order to correct the irradiation coefficients so that they consider the varying light intensity throughout the day, the variation of solar radiation depending on Heart's position due to the presence of atmosphere needs to be included. The atmosphere is the limiting factor for UV light to access the terrestrial surface. In fact, the atmosphere blocks most of the photons with energy within the wavelength that defines UV light (approximately between 10 and 400 nm of wavelength). A photon crossing the atmosphere interacts with its matter through mainly two processes: scattering and absorption. Which of the two processes actually take place, it depends on the wavelength of the photon/radiation and the size of the interacting atmospheric particles [46]. These particles can be air molecules, but also dust or aerosols. Especially, water vapour, oxygen, ozone and carbon dioxide are responsible for absorbing short-wavelength radiation [20]. It is straightforward that if the sunlight needs to travel through more atmosphere because it has a low altitude, then more photons will be scattered or absorbed and will not reach the Earth's surface.

In several publications, Christian A. Gueymard analyses different models that aim to simulate the extinction processes of light through the atmosphere. In [21] and [22], the author individuates the presence of different optical masses that contributes to the extinction of light in the atmosphere through absorption and scattering: the optical air mass, based on the Rayleigh scattering, the water vapour, ozone and NO_2 optical air masses, based on the absorption by the gas molecules, and eventually a mixed gas and aerosol optical masses. The author investigates the broadband modelling method, which considers that the upper layers of atmosphere contain NO_2 and O_3 that directly receive the extraterrestrial spectrum. Instead, the light that reaches the following layers is modified by the overlaying optical masses.

The AM model referred above in Equation 3.1 is highly simplified and it is not very appropriate for high zenith angles. In fact, at θ_Z=90°, the AM value tends to infinity, whereas the path length of sunlight through the atmosphere clearly is not. Basically, the equation does not take into consideration the sphericity of the Earth.

An empirical correction proposed by Gueymard in [22] considers the scattering of light due to Earth's curvature, as reported in Equation 3.2 and graphically represented in Figure 3.2.

$$AM(\theta_Z) = \left[cos\theta_Z + \frac{0.48353 \cdot \theta_Z^{0.095846}}{(96.7412 - \theta_Z)^{1.754}}\right]^{-1}. \tag{3.2}$$

This correction of the AM value is not expected to have relevant effect in an urban environment since the sunlight at high zenith angles (low sun altitudes) is mainly blocked by low skyline profile objects. However, this equation is inserted into the model in order to improve its performances in (almost) free horizon situations, which can be oftener encountered along highways in the Netherlands.

Figure 3.3 depicts the AM in a projected sky matrix in which the x-axis represents the 360° of azimuth and the y-axis the 90° of altitude (complementary to the zenith angle, a_S=90°-θ_Z). The AM varies from 1 kg/m^2, when a_S equals 90°, to around 38 kg/m^2, when a_S reaches

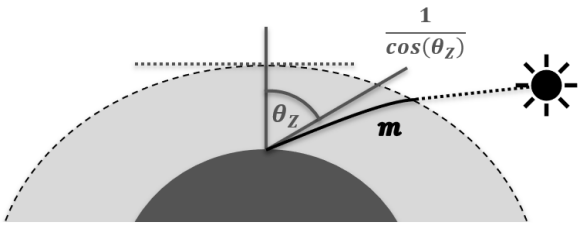

Figure 3.2: Optical air mass simply calculated with the solar zenith angle, θ_Z, and m, as modelled by Gueymard. The dark thick line indicates the bending of the sunlight path due to atmospheric refraction (modified from [34])

0° (38.0868 after [38]). As it can be observed, the model here proposed does not reach the last value of 38 kg/m^2 expected for AM(θ_Z=90°). This is because the lowest value of the matrix count for an altitude of 1°, which in the literature is found to be around 26 kg/m^2 (26.2596 kg/m^2 after [38]), confirming the AM26.3 obtained with the Gueymard model at a_S=1°. This imprecision at horizon level becomes irrelevant after the further implementation of the correction factor based on the angle of incident of light, introduced in Chapter 3.1.2.

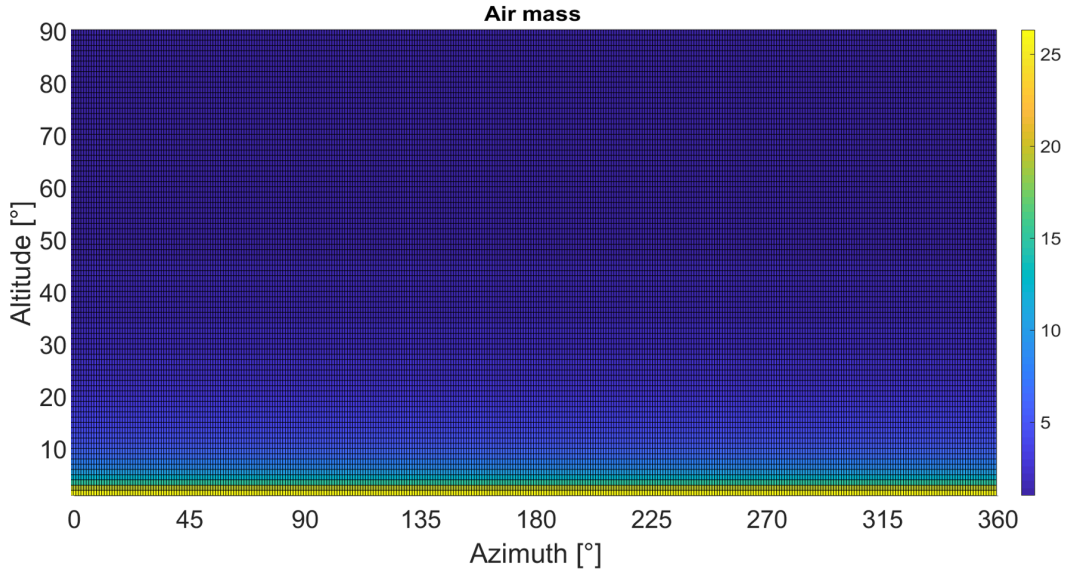

Figure 3.3: AM in a projected sky matrix [kg/m^2]

The SCF only considers the direct sunlight, as it is said in [13]: “it is easy to imagine a case where the direct and circumsolar irradiation components cannot be estimated using the sky view factor. [...] Therefore, to estimate the irradiation due to these other two components, we introduce a new indicator: the sun coverage factor”.

In 1970, experiments conducted in the Mojave Desert of California disclosed a clear correlation between direct irradiance and sun altitude. The irradiance intensity is observed to reduce with decreasing a_S (or increasing θ). This phenomenon is related to an increase of optical air mass and therefore the increase of scattering and absorption of light beams in the atmosphere. Following this physical concept, the irradiance of a point consequently increases together with its altitude too. This because the direct sunlight needs to pass through less atmosphere [48].

The relation between direct irradiance component, sun altitude and point elevation (only within the first km of altitude) can be obtained with the empirical Equation 3.3, adapted from [48].

$$I_d(AM(t), h) = I_0 \cdot (1 - 1.4 \cdot h) \cdot e^{-0.357 \cdot AM(t)^{0.678}} \tag{3.3}$$

with I_0 the solar constant 1361 [W/m^2] [20] and h the altitude of the point of observation [km].

In the particular case of this project related to solar roads in the Netherlands, the location elevation will be irrelevant. However, it may be useful for future application of the method in different areas of the world.

All this considered, a correction factor f_{AM} based on optical air mass is introduced in the model. The factor is defined as the ratio of the actual direct beam at a specific point h and AM to the direct beam at AM1, as expressed in Equation 3.4. This because the $I_d(AM1)$ indicates the maximum direct irradiation that after passing the atmosphere can actually reach the terrestrial surface. AM1 describes the situation of the Sun positioned at the zenith (a_S=90°), where the shortest possible path of atmosphere needs to be overcome (around 100 km).

$$f_{AM} = \frac{I_d(AM(t))}{I_d(AM1)} \tag{3.4}$$

Figure 3.4 and 3.5 represent the correction factor based on AM and its effect on the analemma respectively. As it can be observed, the effect of this correction is limited to the first 15-20° of altitude. The impact of this correction will be therefore mainly observed in (almost) free horizon conditions.

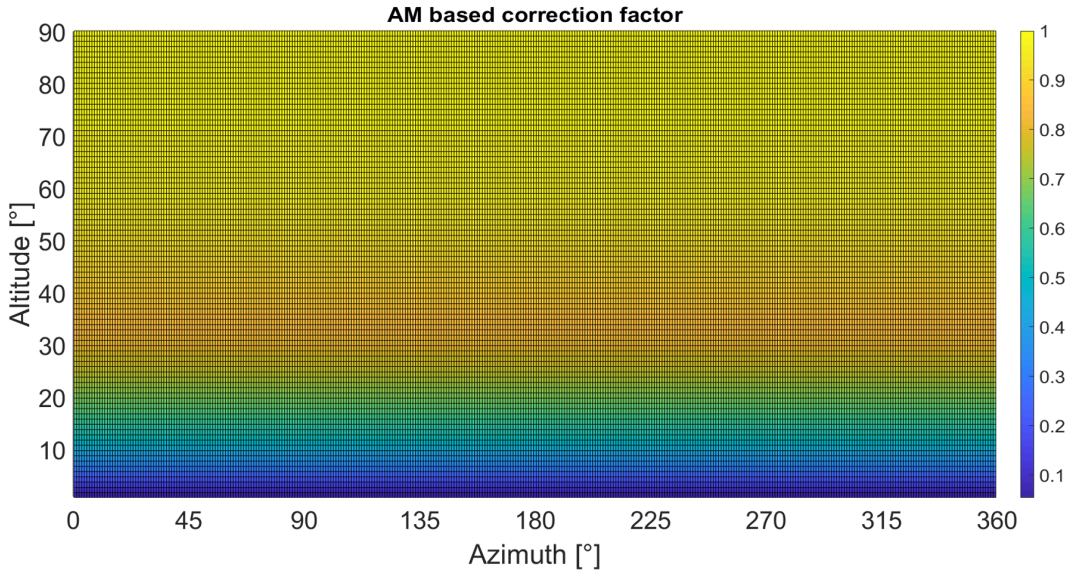

Figure 3.4: The AM correction factor in a projected sky matrix

3.1.2. The AoI correction factor

As already presented in Equation 2.2, the direct irradiance on the POA is directly proportional to the cosine of the AoI, expressed in Equation 2.3. This is commonly called the ”cosine effect” or ”cosine law” and considers that when the altitude of the Sun is not aligned with the normal to the POA, the direct beams that reach the module surface are reduced, proportionally to the angle that quantifies this misalignment (the AoI). Figure 3.6 represents this effect and shows that the solid angle, from which the sunbeams can reach the module surface, becomes smaller with increasing AoI.

Hence, the correction factor f_{AoI} can be obtained with the cosine of the AoI:

$$f_{AoI} = cos(\theta_M) \cdot cos(\theta_Z) + sin(\theta_M) \cdot sin(\theta_Z) \cdot cos(A_S - A_M) \tag{3.5}$$

where θ_Z is the zenith angle (90°-a_s), A_M is the orientation of the module and A_S the sun azimuth. Figure 3.7 and 3.8 represent the correction factor based on AoI and the final effect on the analemma of the superposition of the AM and AoI correction factors, respectively.

From Equation 3.5, it can be stated that for modules with a tilt angle equal to zero, which corresponds to the approximation considered in this report for solar roads, the correction factor can be reduced to the single cosine of the zenith angle. As it can be observed also in

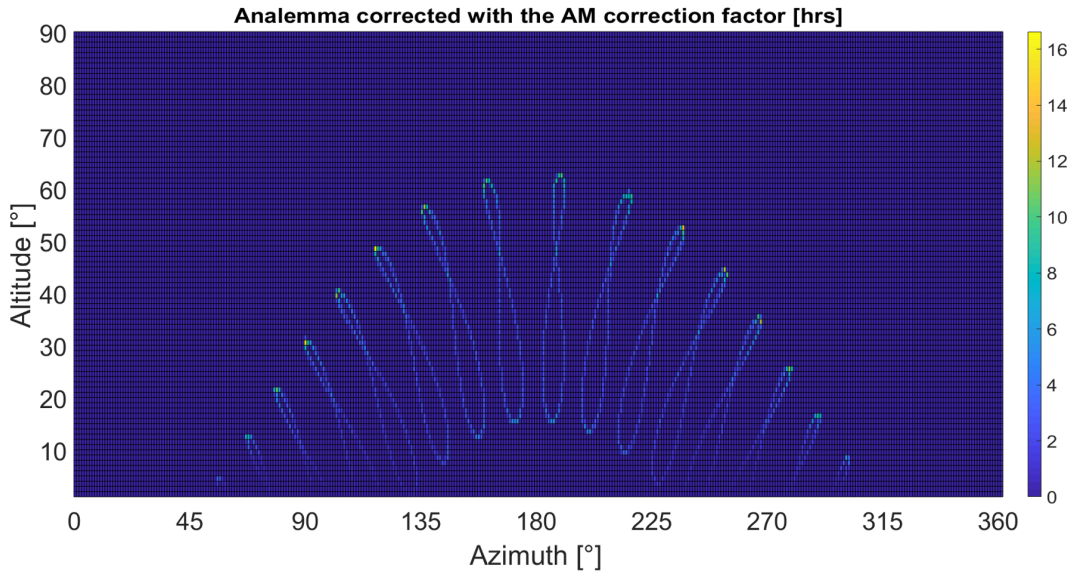

Figure 3.5: Analemma adjusted with the AM correction factor [hrs]

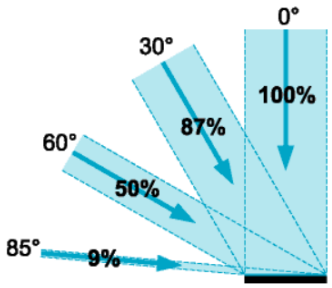

Figure 3.6: The Lambert's cosine law: reduction of the direct beams depending on the angle of incidence [9]

Figure 3.7, this correction will significantly reduce the direct irradiance at altitudes up to 40-50°. In Figure 3.8, it can be noticed how the product of the two correction factors strongly reduces the amount of irradiation received by a solar road. In particular, the irradiation coming from a sun altitude up to 10° is completely invisible for a PV module placed on a horizontal surface.

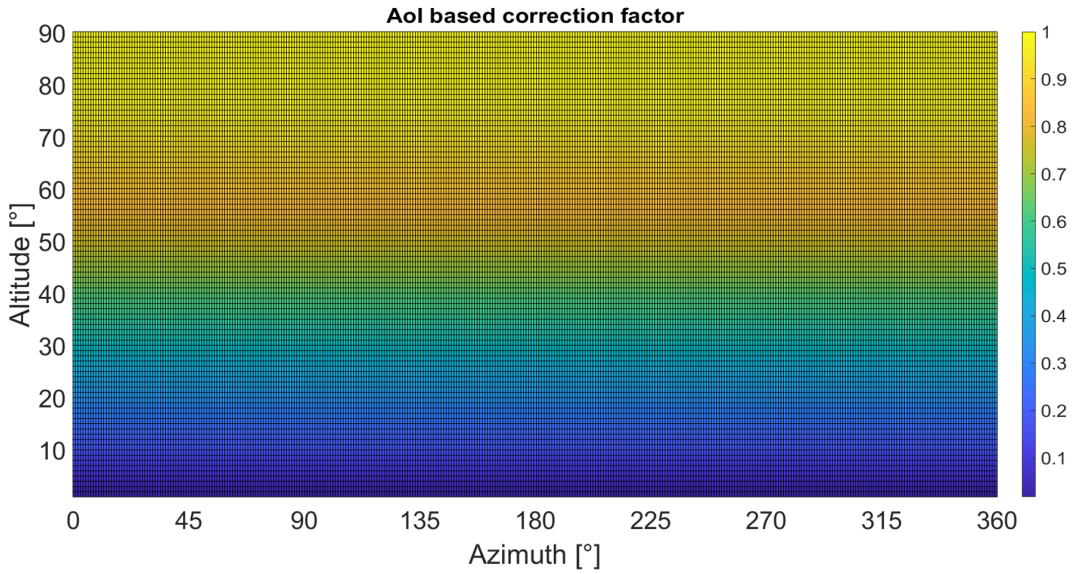

Figure 3.7: The AoI correction factor in a projected sky matrix

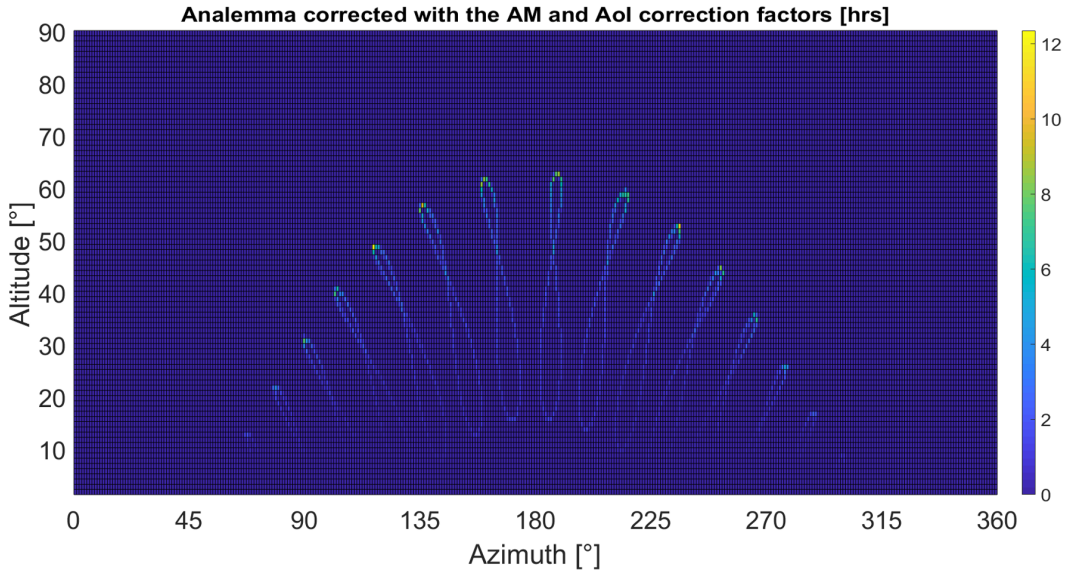

Figure 3.8: Analemma adjusted with the AM and AoI correction factors [hrs]

Figure 3.9: Irradiation map of the Netherlands (source: SolarGIS)

3.1.3. Generation of irradiation coefficients for solar roads

After having applied the improvements described in the previous sections, the irradiation coefficients for solar roads in the Netherlands can be generated. To increase the accuracy of the model, it is chosen to divide the Netherlands into two parts, the South-West and the North-East. This is due to the fact that the country shows a variation of irradiation potential moving from South-West to North-East, as it can be recognized in Figure 3.9. The climate data of two cities within these sections, Delft (52.010000, 4.357000) and Leeuwarden (53.202402, 5.795840) respectively, were used to generate the irradiation coefficients for the area.

As in Equation 2.7 and already explained in Section 2.2.2, five coefficients are generated that account for the different components of irradiance. Tables 3.1 and 3.2 report the obtained coefficients. It can be noticed that, with an assumed 0° tilt angle, no ground reflectance is considered. Therefore, the coefficient c_5 results to be zero.

Table 3.1: Irradiation coefficients for South-West Netherlands

Θ_M	c_1	c_2	c_3	c_4	c_5	Sum
[°]	[kW/m^2]	[kW/m^2]	[kW/m^2]	[kW/m^2]	[kW/m^2]	[kW/m^2]
0	549	147	-81	411	0	1026

Table 3.2: Irradiation coefficients for North-East Netherlands

Θ_M	c_1	c_2	c_3	c_4	c_5	Sum
[°]	[kW/m^2]	[kW/m^2]	[kW/m^2]	[kW/m^2]	[kW/m^2]	[kW/m^2]
0	482	257	-163	406	0	982

3.2. Input data

A more detailed description of the procedure of data processing that is applied in this project can be found in the manual in Appendix F.

3.2.1. Highways of the Netherlands

The list of the national Dutch highways is provided by the Ministry of Infrastructure and Water Management in https://www.rijkswaterstaat.nl/wegen/wegenoverzicht/index.aspx. Out of 38 national highways, 36 of them are considered. For A35 and A37 no data are available at the moment in which the study is conducted.

3.2.2. LiDAR data

As explained in Section 2.2.2, the two main inputs to obtain the yearly irradiation of selected locations are the irradiation coefficients and the skyline profile, which describes the surrounding objects projected on the POA. This is usually obtained with an HORIcatcher, a device of Meteonorm which is able to capture a 360° image of the horizon using a fish-eye lens.

However, if a vast area wants to be analyzed, this approach results to be very time consuming if not impracticable. A more feasible solution to obtain the skyline profile from the side along the motorways of the entire Netherlands is instead the use of a digital surface model (DSM). A DSM captures and represents the natural and built features on Earth's surface (differently than a terrain model or DTM, which only include bare Earth elevation data). It could be considered as a 3D image of the natural and built environment of an area.

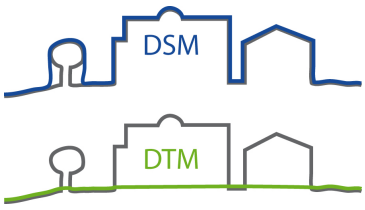

Figure 3.10: Illustration of the difference between DSM (above) and DTM(below)

These models are generated with a measurement system called LiDAR (Light Detecting and Ranging) and are normally collected in a regional or national database. The Netherlands provides the DSM of the entire country as Actueel Hoogtebestand Nederland (AHN) in an online open-source dataset (pdok.nl). The data, represented in Figure 3.11, are the results of a collaboration between the central government and the provinces.

LiDAR is an optical remote-sensing technique which implements a laser light beam to sample the surface of Earth, collecting x,y,z measurements. As depicted in Figure 3.12, the measurement is performed by a moving vehicle (usually an aircraft, helicopter or a car) where a scanner system, a GPS and an inertial navigation system (INS) are incorporated. The latter is used to measure roll, pitch, and heading of the LiDAR system.

Laser pulses are emitted from the scanner system, they reach the Earth surface and are reflected back to the vehicle where they are collected. The time of return of the emitted beams is then converted into a height model of the scanned area. For more detailed information about how LiDAR data are collected, it is possible to refer to [1].

The improvement that the use of LiDAR data brings to the solution approach is straightforward. LiDAR data represent a good replacement for real-life measurement, providing urban elevation profiles in a digital form. On the other hand, the accuracy and method of data

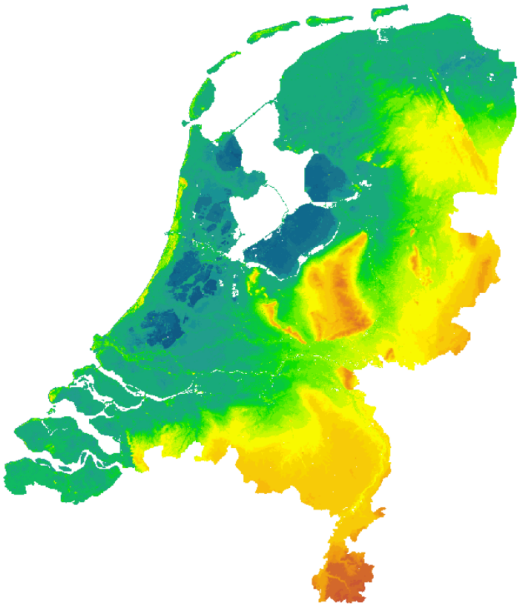

Figure 3.11: Map of the Actueel Hoogtebestand Nederland [12]

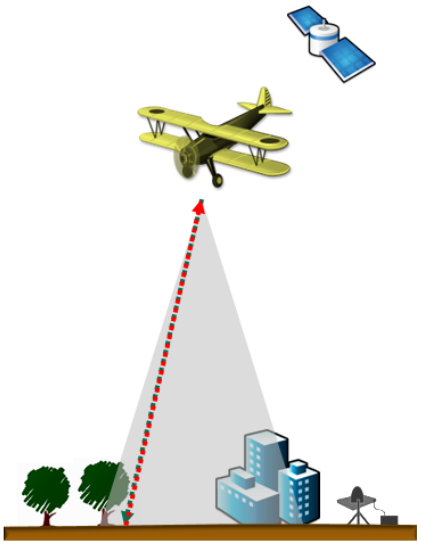

Figure 3.12: Representation of LiDAR system measurement [1]

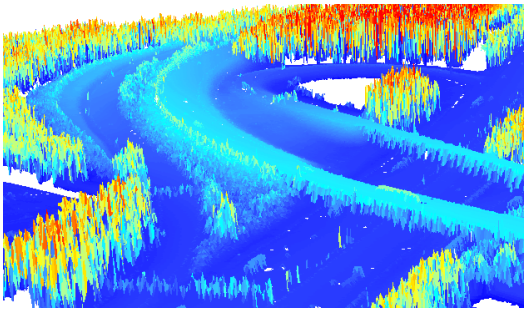

(a) LiDAR DSM of a bridge and aligned trees

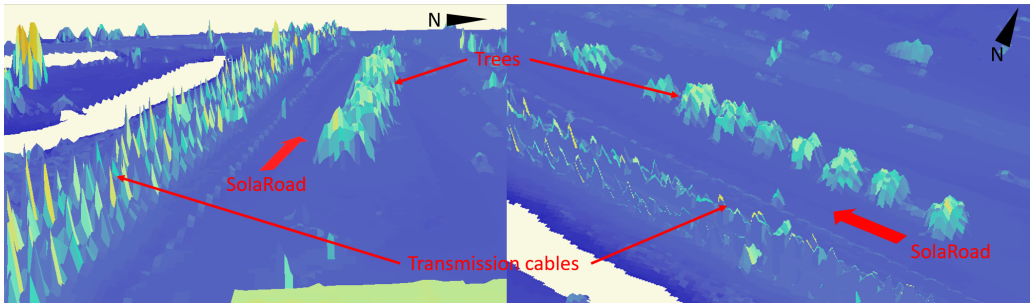

(b) LiDAR DSM of aligned trees and cable lines along the TNO SolaRoad in Krommenie

Figure 3.13: Temperature variation of solar road modules simulated in Delft for one year

extraction still define some limits to the implementation of LiDAR data.

First of all, the data are likely to be outdated. The measurements are conducted on a regular basis of some years. Hence, they will not represent changes in the urban or rural landscape which instead varies in a shorter period of time. Additionally, a scan of the entire national area takes more than one year. Therefore, data from different regions will also be dated differently. The LiDAR data utilized in this project (AHN3) are the most recent ones and were collected between 2014 and 2019 (AHN1 are dated 1997-2002 and AHN2 are dated 2007-2012). Appendix A shows the progress in LiDAR detection for AHN3 in the Netherlands.

Secondly, the resolution of the output data is limited. The most detailed images that can be extracted from the online open-source represents the surface of the Netherlands in pixel of 0.5 x 0.5 m^2. This resolution is the one applied in the model presented here.

In the last instance, LiDAR data present some intrinsic errors. The most relevant one is that they cannot represent vertical surfaces. This is due to the fact that the measurements are taken from above the ground and therefore no information is given about the real shape of the detected objects, which are simply seen as perpendicular walls. This does not represent an issue in the majority of the cases, such as for buildings since the walls are perpendicular to the ground. However, features like trees, bridges or even hanging cable lines and traffic shields are represented as monolithic blocks with vertical walls. Figure 3.13 gives an idea of how the 3D elevation model from LiDAR data represent a bridge, trees and transmission cables.

This aspect of LiDAR data represents an obstacle when it comes to estimating the irradiation potential of solar roads in the proximity of these objects. For instance, if it is desired to evaluate the potential of a solar road collocated close to an underpass, the irradiance coming from below the bridge cannot be evaluated with the method presented above, since the LiDAR data itself represent the sides of the bridge as a wall standing perpendicularly from the ground.

3.2.3. Road maps

LiDAR data represent the surface area but do not give any additional information about the detected items. It is therefore impossible to recognize the different objects, if not for the user to visually identify them. Basically, the user can recognize from the LiDAR image where a

Figure 3.14: Map of the Hectopunten of the Netherlands

road is collocated, but the software cannot apply the same method, if not with a complex machine learning approach. Assuming that this technology is not available - which is true for the majority of the cases - it is necessary to collocate highways in the LiDAR data using coordinates of a geographic system. Again, if a vast area wants to be analyzed, a manual work results to be very time consuming and inaccurate.

The solution that is found in this research project is the superposition of the LiDAR images with the Nationaal Wegenbestand (NWB) map, represented in Figure 3.14. The NWB is a dataset of the governmental open-source pdok.nl which illustrates the entire road network of the Netherlands.

The coordinates of highway location markers are used to represent the roads routes. In fact, each point of the map corresponds to a so-called hecto-point. This is a location marked along a road each 100 m (the word comes from the SI prefix ”hecto-”, meaning ”hundred”), starting from its relative begin until its end, building the so-called hectometration of a road. While not all of these hecto points correspond to a physical sign along the road, it is true that they never exist in isolation, but always in a contiguous series of points connected by means of a constant distance. Also, each lane of a road is provided with its own hectometration.

The use of this map reveals to be advantageous for the scope of this project for two main reasons. First of all, this map allows to georeference[1] roads in LiDAR data. Secondly, the hecto-points provide regularly distributed points along roads width and length, which permits to conduct a sensitivity analysis of the model by increasing or reducing their relative distance.

3.3. Calculation of the skyline profile

The skyline profile consists of a projected 360° image of the objects that surround the module site. In order to extract this from the LiDAR data of the analyzed area, the approach described in the work of Keijzer [43] is used.

To apply the model to this research project, it is necessary to introduce a link between the LiDAR image loaded in MATLAB and the geographical coordinate system of the points to be analyzed. Known the coordinates of the LiDAR image vertices (these can be extracted with the MATLAB function geotiffread), it is possible for example to obtain the point x coordinates X_{Points} on the LiDAR image as

$$X_{Points} = \frac{X_{RD} - X_{min,LiDAR}}{dX} \tag{3.6}$$

[1] It means that the internal coordinate system of a map or image can be related to geographic coordinates system.

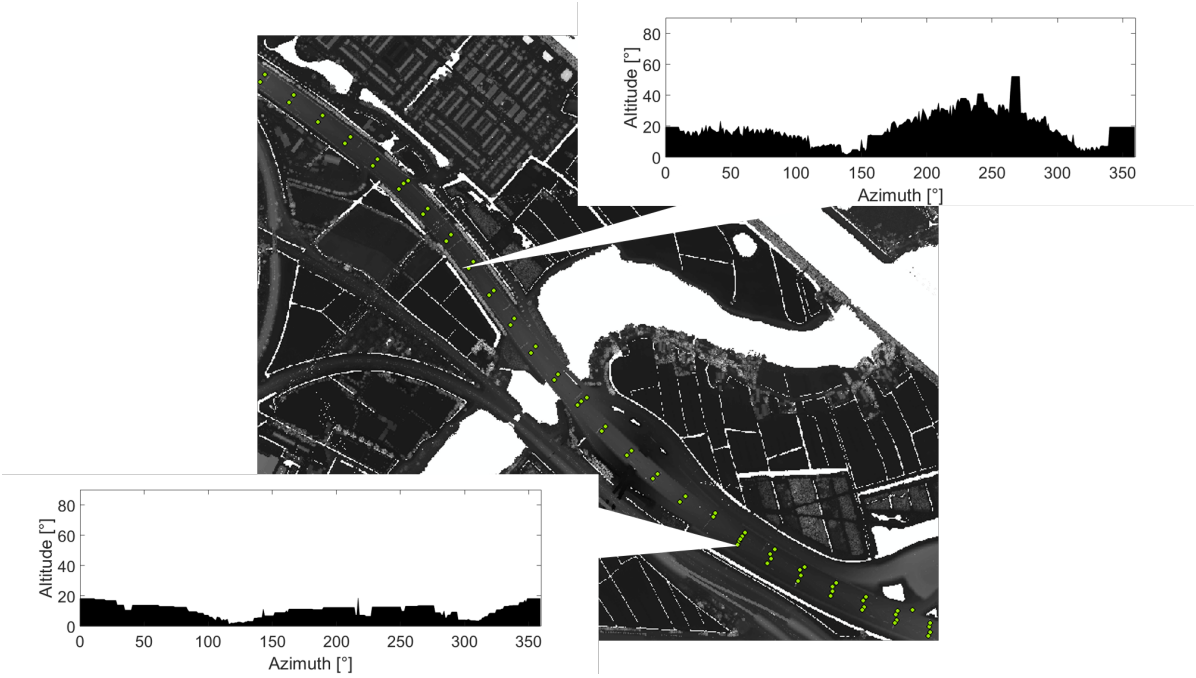

Figure 3.15: Example of the skyline profiles extracted from two points along the A1 (127.384, 483.924 and 128.151, 483.138)

where X_{RD} is the x-coordinate of the points in the RD Amersfoort geographical coordinate system[2], $X_{min,LiDAR}$ is the x-coordinate of the South-West corner of the LiDAR image where the points are found, and dX is the LiDAR data resolution, in this case, 0.5 m. The model can now extract the skyline profile of the surrounding of any point whose coordinates are provided and many points can be given as input in one time. Figure 3.15 gives two examples of how the results look like.

3.4. Calculation of the sky view factor

In a condition of free horizon, the SVF depends solely on the module tilt angle θ_M and can be obtained with Equation 3.7.

$$SVF_{fh}(\theta_M) = \frac{1 + cos(\theta_M)}{2} \tag{3.7}$$

However, in the majority of the cases, a raised horizon is present and in the calculation of the SVF the location-specific skyline profile must be considered. In [64], a method is developed to obtain the SVF from skyline 2D projections from fisheye-lens images. The image is first divided into a raster, which in this work presents a 360 x 90 dimension (one value for each 1° of altitude and azimuth). For each of the generated rectangular sectors, the contribution to the SVF value is obtained from Equation 3.8.

$$\Phi_i = \frac{\pi}{n} \cdot sin(\frac{\pi \cdot (i - 0.5)}{2n}) \cdot cos(\frac{\pi \cdot (i - 0.5)}{2n}) \tag{3.8}$$

As it can be observed, Φ depends on the amount of annular rings that are considered. As already mentioned, in this work n=90 rings is taken. Eventually, the sum of all the sectors' weight corresponds to the visible part of the sky, i.e. the SVF of the location. Since 360 "horizontal slices" are considered in this work, the SVF is obtained as expressed in Equation 3.9.

[2]National Triangle Coordinates (also known as RD coordinates) are the coordinates used at national level in the Netherlands as a basis for geographical indications and files, such as national topographic maps, cadastral maps, DSM etc.

$$SVF = \sum_{i=1}^{n} \frac{\Phi_i}{360} \cdot N \tag{3.9}$$

where N is the amount of free sky rectangular sections on the annular ring i.

For solar roads, it is assumed a module tilt angle of 0°, even if roads sections generally show an inclination, but very small (below 5°). Due to this assumption, the influence of the sky section that is not visible to the module surface due to the tilt angle is not further considered in this work.

3.5. Calculation of the sun coverage factor

The SCF is a function of the altitude of the Sun (a_S) and of the skyline profile (a_{SP}). Considering the annual Sun path and approximating the Sun as a 1D point located in its geometrical centre, the SCF is equal to 1 if the Sun is positioned on the skydome projection above the horizon but behind a projected obstacle profile. In [13], its calculation is summarized in Equations 4.5.

$$SCF = \frac{\sum_{year} \mathrm{X}_{SP}(A_S(t), a_S(t))}{\sum_{year} \mathrm{X}_{FH}(a_S(t))} \tag{3.10}$$

Where

$$\begin{aligned} \mathrm{X}_{SP}(A_S(t), a_S(t)) &= 1 \quad \text{if} \quad 0 < a_S(t) \leq a_{SP}(A_S(t)) \\ &= 0 \quad \text{otherwise} \end{aligned} \tag{3.11}$$

$$\begin{aligned} \mathrm{X}_{FH}(a_S(t)) &= 1 \quad \text{if} \quad a_S(t) > 0 \\ &= 0 \quad \text{otherwise} \end{aligned} \tag{3.12}$$

3.6. Sensitivity analysis of the azimuth step angle

To analyze the impact that the precision of skyline profile extraction has on the irradiation output, a sensitivity analysis based on the increase of the azimuth step angle is conducted. The aim of this analysis is to evaluate the gain in computational time against the loss of accuracy in the irradiation potential estimation of a point and eventually find the optimal trade-off between the two aspects.

Instead of every 1°, the presence of obstacles is detected for every 2°, 5°, 10°, and 20°. The obtained profiles were eventually interpolated into 90°x360° skyline projections. The results were then evaluated in order to find the optimal azimuth step angle.

The analysis is applied to a sample of 496 points taken from a section of the A16, following the here explained procedure:

1. the skyline profiles of the point sample is calculated with a 1° azimuth step angle;
2. for each point the skyline profile is again calculated with an azimuth step angle of 2°, 5°, 10°, and 20°;
3. for each of the calculated skyline profiles the annual irradiation Irr is obtained;
4. the ratio of the Irr_X with X-degrees azimuth step angle on Irr obtained with 1° degree step angle is calculated as

$$Dev = \frac{Irr_X}{Irr_1} \tag{3.13}$$

   With Irr_X the irradiation calculated with an azimuth step angle of X°;
5. the standard deviation is obtained;

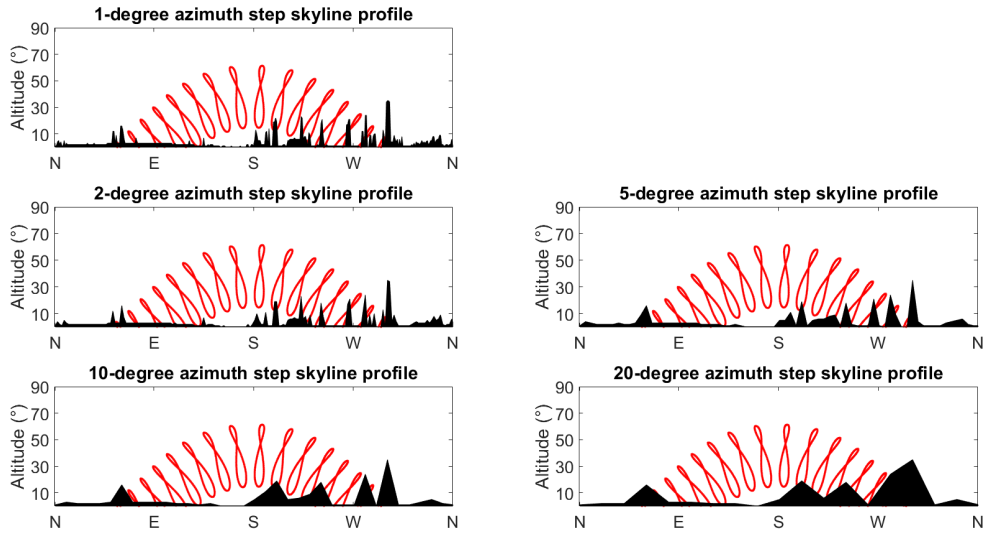

Figure 3.16: Example of how the skyline profile changes by tuning the azimuth step angle

Figure 3.16 provides an example of how a skyline profile is affected by the increase of azimuth step angle, whereas Figure 3.17 shows the results of the sensitivity analysis. It can be observed that by reducing the step angle, the maximum number of calculations necessary when extracting the skyline profile decreases exponentially. However, this increases the percentage of deviation of the results from the reference values obtained with 1° azimuth step angle in an almost linear correlation.

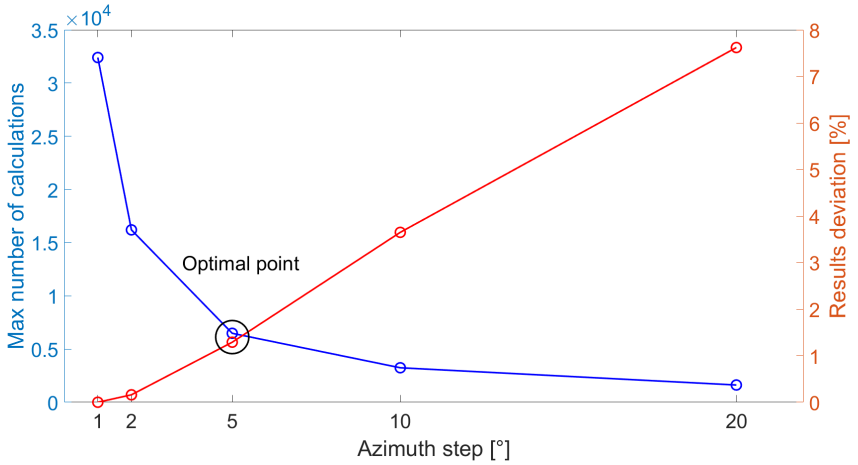

Figure 3.17: Maximum number of calculations and deviation of the irradiation results from the reference model by increasing the azimuth step angle

The optimal point is found at 5° azimuth step angle. This would lead to a reduction of 80% of the number of calculations [3] and a deviation below 2% in the irradiation values obtained. Still, an azimuth step angle of 1° is kept in the model. The detailed results of the sensitivity analysis for increased azimuth step angle can be found in Appendix B.

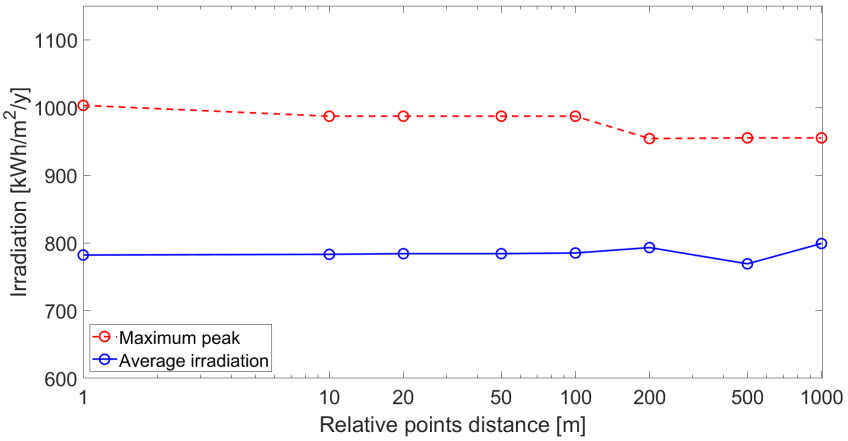

Figure 3.18: Variation of average and maximum irradiation values by increasing relative points distance

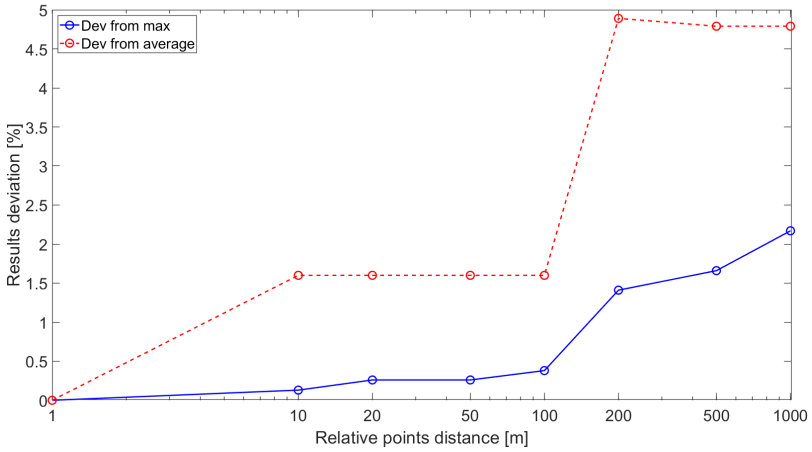

Figure 3.19: Irradiation results deviation by increasing relative points distance

3.7. Sensitivity analysis of the road points density

There are over 1,600 km of highways in the Netherlands. It is straightforward to understand that the points used as input data can only represent a limited amount of the above-mentioned road surface, generating results with an inevitable margin of error.

The objective of the sensitivity analysis of points density is to estimate the accuracy of the model and how the following parameters influence the model output:

- the density of points distribution along the road length
- the density of points distribution along the road width

In order to evaluate the model sensitivity, the following method is applied for 7.4 km and for a cross-section of the A16:

1. the number of points is first adjusted along the road, varying the distance point-to-point (from now on referred as relative points distance) from 1 to 10, 20, 50, 100, 200, 500 and 1000 m on the road length, and from 5 to 15 and 20 m on the road width;
2. the skyline profile is extracted from each of the obtained points;
3. the irradiation model is applied to each of the obtained points;

[3]In general, it can be stated that computational time and number of calculations are directly proportional. However, the actual running time depends on the server used and, in the case of this model, also on the single skyline profile extracted.

Figure 3.20: Location of the pyranometer mounted on the TNO SolaRoad in Krommenie

4. the average, maximum and minimum irradiation is calculated;
5. the deviation from the reference sample (relative points distance of 1 m) is reported as

$$Dev = \frac{mean(Irr_X)}{mean(Irr_1)} \tag{3.14}$$

With Irr_X the irradiation vector for all the points contained in the road section analyzed and with a relative distance of X m.

Figure 3.18 represents the results of mean and maximum irradiation obtained for the different relative points distances, while Figure 3.19 shows their relative deviation from the reference values. The results of the sensitivity analysis are reported in details in Appendix B.

As it can be observed, with the increase of the relative point distance, it is still possible to represent the average and peak irradiation along the road with a deviation lower than 2% from the reference case. However, after 100 m of relative distance, values start to vary more largely and the deviation grows up to 2.2% in the case of average values and up to 4.8% for peaks. This is due to the fact that the skyline profile does not follow any pattern and it is rather random. Therefore, when the points are more densely distributed, more details about specific points will be captured. If the points are rarer, it is more probable to miss peaks of maximum and minimum irradiation.

The relative distance of 100 m at which the data are provided in the Hectopunten map shows a 0.4% deviation from the reference average and a 1.6% deviation from the maximum reference values. This is considered a good balance between computational time and accuracy of the results. The relative distance of 100 m is therefore kept in the model.

The variation of the distance between the points along the road's width needed to be changed manually and is therefore probably less accurate than the previous two analysis performed. The results can be found in Appendix B. It seems not to indicate a logical pattern in the variation of the density of the points along the width. A more accurate research should be therefore conducted in order to deliver any useful information towards the improvement of the model accuracy.

3.8. Validation

In order to validate the model, real data of annual irradiation are needed. Thanks to the collaboration with TNO it is possible to use the real data measured of GHI on the site of the TNO SolaRoad pilot project in Krommenie, Amsterdam. Figure 3.20 shows the pyranometer situated on a 4 m high stand along the SolaRoad and its location in LiDAR data.

The irradiance measured every 5 minutes from the pyranometer is integrated for one year to obtain a reference annual GHI for the location. This resulted to be 1034 kWh/m^2/y.

Comparing the model results for the indicated location with the integrated irradiance measured by the pyranometer, it is possible to evaluate the deviation of the model from real

data. The estimated annual irradiation is of 1011 kWh/m^2, with a deviation from real data of 2.2%. This error can be further reduced if the component of artificial light is ignored from the measured values. Simply reducing to almost zero the nocturnal irradiance value, caused by artificial light, decreases the reference value to 1029 kWh/m^2/y and the error to 1.7%.

4

Solar roads modelling

In this chapter, further aspects that are exclusive for solar road PV systems are explored. The model to account for traffic shading in the final irradiation and DC yield output, together with the real traffic input data, is here described in details. The case studies of A12 and A16 are introduced. In addition, the temperature model used to simulate the solar road module temperature variation is explained. Eventually, a comparison between the temperature output of the TNO SolaRoad and the assumed glueable technology is conducted.

4.1. Characteristics of solar roads modelling

Figure 4.1: When modelling solar road systems, five main aspects should be considered: the shading caused by the elevated skyline, the shading caused by vehicles, the output reduction due to operational temperature, the performance drop due to soiling effect and variation of irradiance due to haze and pollution, and the feasibility of the installation. The latter includes considering noise generation, costs, etc.

Some additional aspects that affect the output potential of the system need to be considered when modelling solar roads. Figure 4.1 aims to indicate the four most important groups of aspects when it comes to modelling solar roads.

Rather different than conventional PV modules, a solar road can be completely shaded not only when the sun light is blocked by the surrounding skyline profile, but also when a vehicle is driving on it. Traffic represents one of the biggest concerns and critics for implementation of solar roads, as it is claimed that the power could be substantially reduced by cars standing in a traffic jam.

By thinking about the dirtiness that can be found on busy urban roads, it can be understood how the soiling effect is relevant when it comes to solar roads. Trash and other objects, together with sand and soil can reduce the irradiance that reaches the module beneath the road surface. In addition, vehicles also cause air pollution. A high concentration of particular matter (PM) can not only scatter sunlight but also changes the light spectrum that reaches the road surface. This can cause a reduction in PV cell conversion efficiency.

Due to their position close to the ground and surrounded by obstacles, roads do not easily receive natural ventilation. However, they are still exposed to solar irradiation for the entire day and they are mainly built with dark coloured materials, such as asphalt, which absorb light in all its wavelengths. For these reasons, road surfaces can reach a very high temperature and this can impact solar road power conversion efficiency, as well.

Last but not least, when designing solar road projects, not only irradiation and power output potential are to be taken into consideration but also costs, which are the main driver in terms of feasibility of a project. Solar roads can still show an important initial capital investment and a long payback time. These aspects will likely improve with more research and mass production in the future. However, solar roads need also to comply with strict road regulations, in particular, noise limits in urban and residential areas. Conventional roads are studied and built to reduce the vehicles passing noise and solar roads will need to do the same. Otherwise, additional costs for noise abatement measures needs to be accounted, such as the erection of noise barriers, the introduction of speed limits, etc.

In the model developed in this research project, traffic shading and temperature-dependent conversion efficiency are included. Further suggestions regarding soiling and haze impact on solar roads output power can be found in Chapter 7.

4.2. Traffic

In 2018, almost 11.3 million vehicles [1] have been counted on the Dutch roads [3]. If we consider an average speed of 60 km/h [49], assuming an average car density on the main roads of 2000 vehicle/h, and approximating the length of a car to almost 5 m, it can be estimated that roads are fully covered by car for around

$$5m \cdot \frac{1}{25}\frac{s}{m} = 0.2\frac{s}{veh} \tag{4.1}$$

$$0.2\frac{s}{veh} \cdot 2000\frac{veh}{h} \cdot \frac{1}{3600}\frac{h}{s} = 17\% \tag{4.2}$$

of the time. If only highways are considered and the average speed is set at 90 km/h [49], the estimated coverage time drops to 11% applying the same simple calculation. Both these estimations are considered in the literature as well. Wattway by Colas claims that roads are generally occupied by vehicles only 10% of the time [70] and in [57] it is stated that roads are used by cars only 20% of the time.

This small numbers should encourage who is sceptical for solar roads applications. However, it needs to be taken into consideration that on specific locations the dynamic shading caused by traffic could instead significantly affect the output of the area and therefore be a relevant aspect when deciding whether to build a solar road or not.

4.2.1. Traffic shading model

In order to insert this location-specific aspect in the model, traffic data of Dutch highways are needed. In July 2016, the department of Traffic & Planning of the Faculty of Civil Engineering and Geosciences at TU Delft created a research lab called DiTTlab (Delft Integrated Traffic & Travel Laboratory), where students, researchers and practitioners can work with traffic data and simulation models. One of the successful projects involved the development of an open-source online app called 'Urban Mobility Lab Demonstrator' that provides accurate traffic data for the whole Dutch road network. The access to this source can be found in [5].

[1] These counts generally do not distinguish between single vehicles. The same vehicle can, therefore, be counted more than once.

In the collected data set, vehicles flow q [veh/h] and speed u [km/h] are provided. The values are measured by so-called vehicle loop detectors. The most common detectors are based on inductive loop, as represented in Figure 4.2: a wire coiled in a circle below the road surface detects the variation of the electric field when an object (in this case a vehicle) passes over the loop. Installed in combination with axle sensors, vehicle detectors can, therefore, register speed and flow of passing vehicles in a defined time interval.

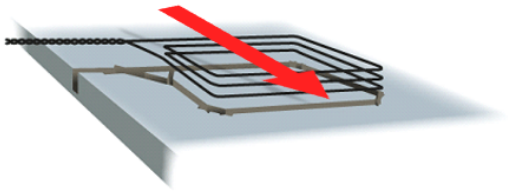

Figure 4.2: Electrical wires of an inductive loop detector embedded in the road asphalt layer (Modified from [6])

The detectors are positioned along the road with an average distance of 500 m from each other. From these sensors, raw data are collected. The research group of DiTTlab applied an adaptive smoothing method (ASM) in order to further process raw data. Developed at the Institute of Economics and Traffic of the Dresden University of Technology, the ASM is a method used to obtain spatio-temporal information from incomplete traffic data. In fact, stationary traffic detectors are often not homogeneously distributed along the road path. Additionally, it is difficult to reconstruct traffic behaviour between two distant detectors. The ASM takes into consideration that, with increasing traffic congestion, information propagates upstream, while in free traffic it moves downstream. This is a useful application to reconstruct traffic situations from incomplete data [67].

The values are eventually represented in matrices where the time of the day (from 2 am to 11:30 pm) progresses along each row, and the hectometers along the road advance along each column, as represented in the examples of a section of A16 in Figure 4.3a and Figure 4.3b. This means that drawing a horizontal line perpendicular to the y-axis, the variation of vehicles' speed throughout the day in a specific point of the road can be obtained. Similarly, following a vertical line perpendicular to the x-axes discloses the different vehicle velocities that are encountered in a specific moment of the day along different sections of the road.

In the figures, it can be observed that the vehicle speed is maintained constant around 100 km/h during the day along the road section. However, at 30 m distance from the beginning of the line, the vehicles speed seems to increase. This can be due to different reasons, such as an expansion of the road width or after a motorway exit, where the car density is reduced.

Regarding vehicles flow, it seems that the most influencing factor is the time of the day. In fact, along the whole road section, it can be recognized a very low vehicles flow before 5:00, a higher flow between 6:00 and 9:00, a constant flow of medium intensity until 15:30, where it rises again until 18:00. This pattern can be attributed to the entrance and exit office hours during the weekdays.

It can occur that for different reasons (technical, of data collection, of data processing) data are missing. An example is given in Figure 4.3, between 10:30 and 11:30 pm in the last meters of the road section, where both speed and flow of vehicles are reduced to zero due to missing data.

In order to couple the traffic with the irradiation data, it is necessary to further elaborate the row data collected by the detectors and filtered with the ASM. First of all, the flow and speed data need to be expanded from 2,580 30sec/day (from 2:00 am to 11:30 pm) to 2,880 30sec/day (24 hours of data). This is done by inserting values equal to zero before and after the actual data. This correction does not influence the quality of the results, since between 11:30 pm and 2:00 am of the following day no sunlight hits the road surface. This makes the traffic data in these time intervals irrelevant for the purpose of this study.

Secondly, the resolution of the collected data needs to be reduced from 30 seconds to one hour basis. This is achieved by averaging both speed and flow data within each hour of the

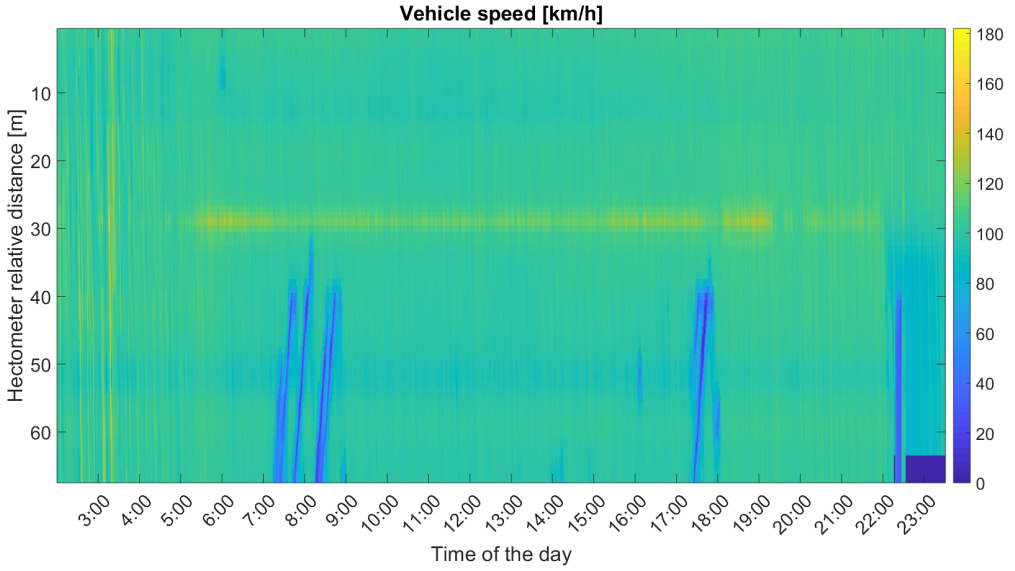

(a) Vehicle speed [km/h]

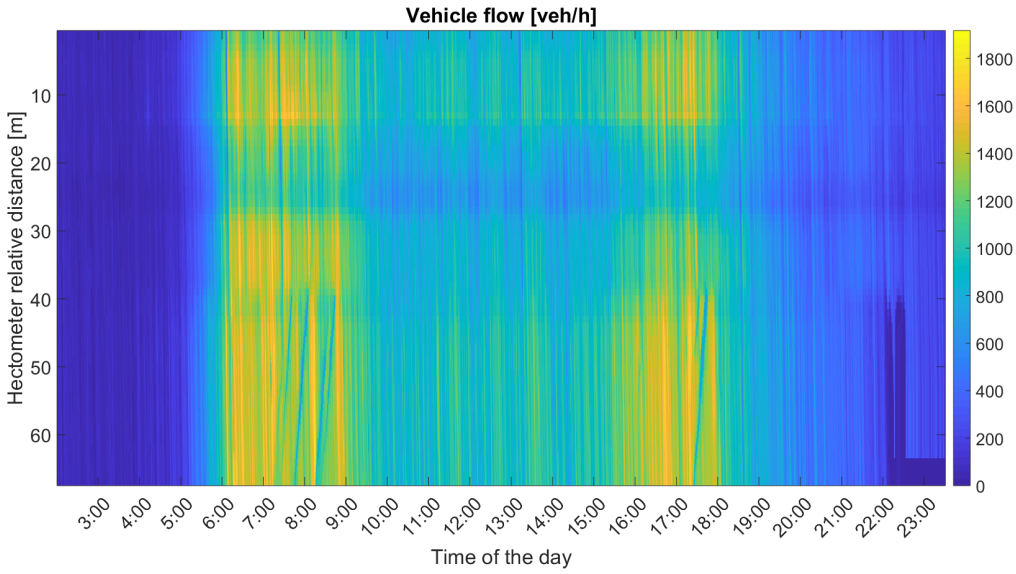

(b) Vehicle flow [veh/h]

Figure 4.3: Traffic data from the TU Delft DITTlab app: A16 15 - 30 km left lane - 4th of June 2018

day.

Eventually, for each speed and flow value, coordinates are needed to generate a geographical distribution of the data. To do so, the route is first described using the coordinates of the hectometers along the road. The coordinates of the detectors are known and are put along the described route and the raw data of vehicles speed and flow are extracted. However, they do not represent a heterogeneous distribution of data along the route. Therefore, the ASM filter is applied to complete the missing data. The flow chart in Figure 4.4 gives a visualization of what explained above.

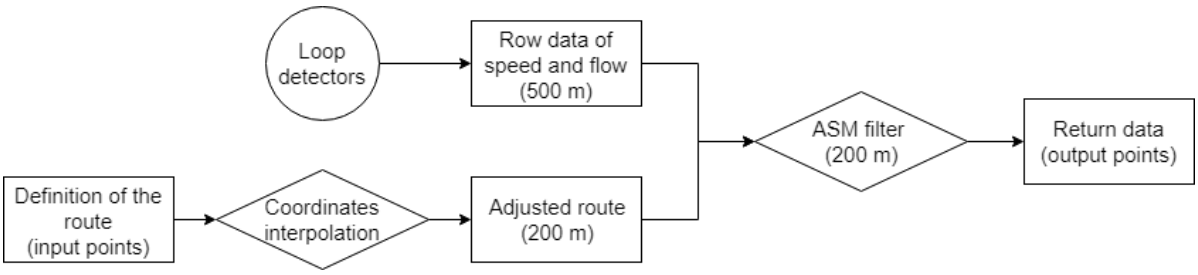

Figure 4.4: Obtaining geographical distribution and missing traffic data

Figure 4.5 explains in a graphical manner the concept of the model behind traffic shading. A vehicle travels above a point, which can represent an infinitesimally small section of a solar road module (Δx→0). The time that the car needs to completely surpass the point can be defined as in Equation 4.3.

$$\Delta t = \frac{d_{veh} + \Delta x}{u(t)} \tag{4.3}$$

Where d_{veh} is the length of the vehicle, here assumed to be 5 m, and $u(t)$ is the travelling speed of the vehicle at the moment t.

Figure 4.5: Visualization of Δt, defined as the time that a vehicle needs to completely surpass a point (here represented in the blue rectangle for simplicity)

The cumulative time in which the point is shaded by passing vehicles ($T_{coverage}$) can be estimated as in Equation 4.9.

$$T_{coverage} = \Delta t \cdot q(t) \tag{4.4}$$

Where $q(t)$ is the vehicles flow [veh/h] at the moment t. $T_{coverage}$ is a vector that represents the amount of time for each hour of the day in which the point is shaded by passing vehicles. Figures 4.6 to 4.8 depict in bar diagrams the vectors $T_{coverage}$, $u(t)$ and $q(t)$ of one point on the A16, left line, on the 1st of June 2018. The same considerations taken above for 4.3b and 4.3a can be recognized in these bar charts. It can be seen that, at constant driving speed, the shading factor is only affected by the traffic flow and follow its variation throughout the 24 hours. These conditions are expected to be often encountered in highways, where the driving speed is more constant than on secondary roads. It can be therefore concluded that the impact of traffic for solar highways will be more influenced by car flow, while solar roads in secondary routes will be also strongly influenced by the reduced driving speed.

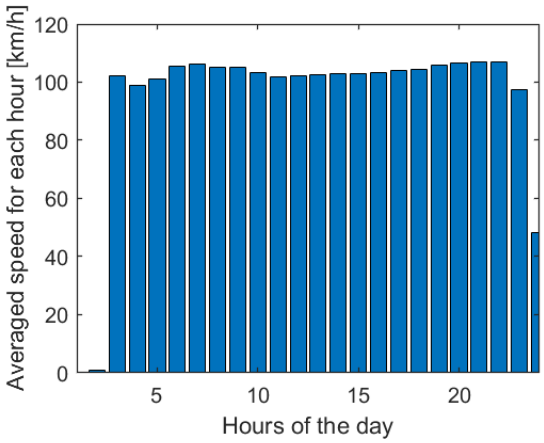

Figure 4.6: Vehicles speed [km/h] - 1st of June 2018 (point taken from A16, left line)

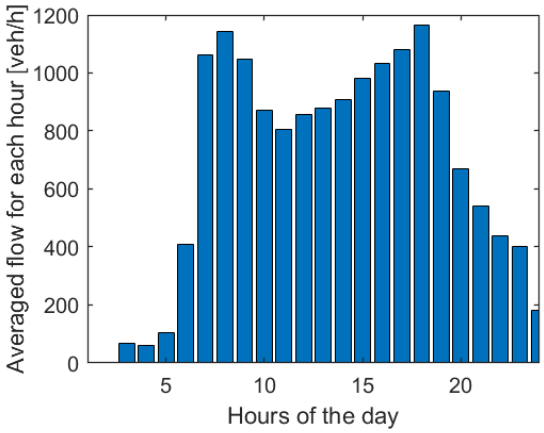

Figure 4.7: Vehicles flow [veh/h] - 1st of June 2018 (point taken from A16, left line)

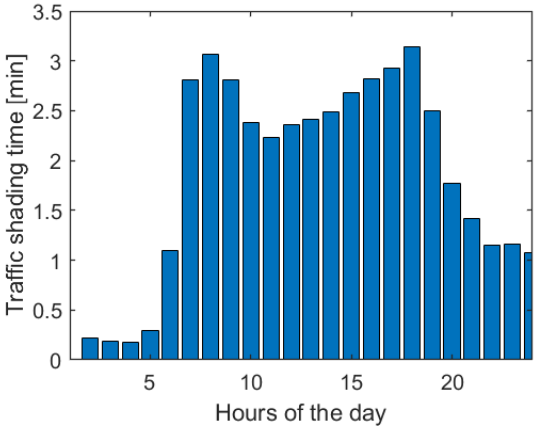

Figure 4.8: Coverage time [min] for each hour of the day - 1st of June 2018 (point taken from A16, left line)

The coverage time $T_{coverage}$ can be seen as a reduction of the time in which the sun is shining on the point. However, the impact of the shading effect caused by a car passing above the road surface varies with time. In fact, a car shading a point of the road surface at noon will have a stronger impact on the reduction of the total daily irradiation if compared with a car shading for the same time the same point in the evening. This is because the

amount of irradiance blocked by the shading object is higher in the first case than in the second. For this reason, the coverage time needs to be weighted depending on the moment of the day and then deducted from the hours in which the sun shines in order to estimate the effective irradiation that reaches the road surface.

Similarly, the coverage time of each hour of the year can be related to a specific position of the sun in the skydome. Transforming the coverage time into a simil-analemma (from now on called traffic shading matrix or $trMat$) allows adding weight to the factor. Figure 4.9 depicts the traffic shading matrix for a point on the A16.

It is now possible to correct the sun analemma by subtracting the traffic shading matrix. The corrected analemma does not refer anymore to the amount of time in which the sun is shining. It represents instead the amount of time in which a *specific point* of the solar road, *actually sees* the sun shining in each hour of the year. It basically indicates the effective hours in which the point on the road surface receives sunlight, considering traffic shading.

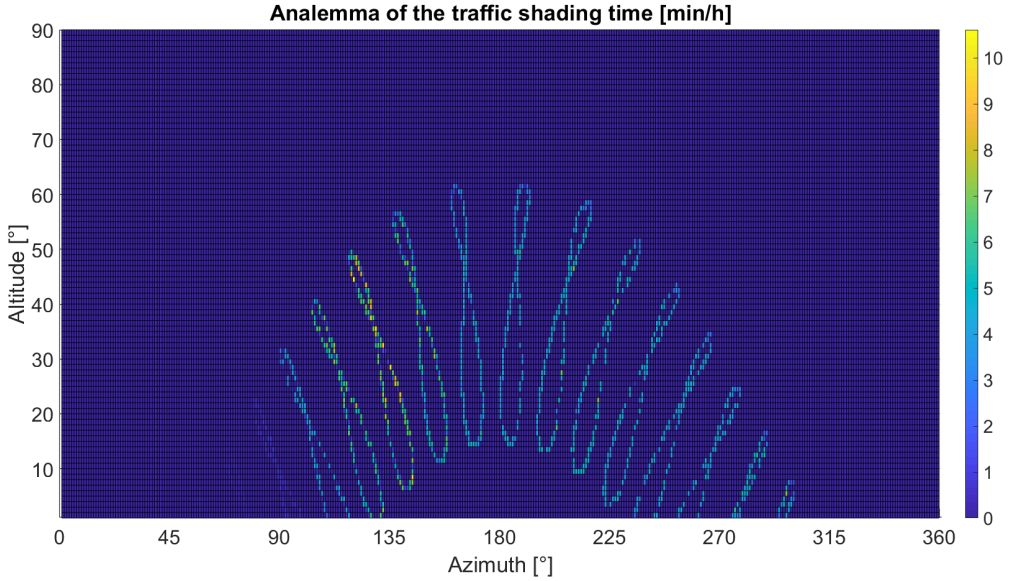

Figure 4.9: Cumulative time in minutes in which a selected point of the A16 is shaded due to traffic at each hour of the year

In order to correct the total irradiation of one point due to traffic shading, SCF and SVF need to be adjusted. The SCF of Equation 3.11 can therefore be redefined as traffic coverage factor (TCF) in Equation 4.6. The traffic coverage factor corresponds to the faction between

- the sum of the hours in which the sun is behind the elevated skyline (SCF),
- plus the time in which the sun is above the skyline profile but the point is shaded by passing vehicles,

and the total amount of hours in which the sun is above the horizon.

$$TCF = \frac{\sum_{year} \mathrm{X}_{SP+tr}(A_S(t), a_S(t))}{\sum_{year} \mathrm{X}_{FH}(a_S(t))} \tag{4.5}$$

where

$$\begin{aligned} \mathrm{X}_{SP+tr}(A_S(t), a_S(t)) &= 1 \quad \text{if} \quad 0 < a_S(t) \leq a_{SP}(A_S(t)) \\ &= T_{coverage}(A_S(t), a_S(t)) \quad \text{otherwise} \end{aligned} \tag{4.6}$$

$$\begin{aligned} \mathrm{X}_{FH}(a_S(t)) &= 1 \quad \text{if} \quad a_S(t) > 0 \\ &= 0 \quad \text{otherwise} \end{aligned} \tag{4.7}$$

The SVF can be corrected to a traffic view factor (TVF) applying a shading factor due to traffic f_{ts}. This can be generated as the ratio between the corrected analemma that considers

Figure 4.10: A16 highlighted in red [71]

Figure 4.11: A12 highlighted in red [71]

the traffic shading, and the one that does not. The traffic shading coefficient will span from 0 in case the traffic completely blocks the sunlight on the road surface for the entire year, to 1 in case the point never occurs to be shaded by vehicles throughout the year.

$$f_{ts} = \frac{sunMat - trMat}{sunMat} \tag{4.8}$$

$$TVF = SVF \cdot f_{tr} \tag{4.9}$$

where $sunMat$ refers to the sun matrix, including the AM and AoI correction factors and the skyline profile, while $trMat$ describes the simil-analemma for the traffic shading.

Using the TVF and the TCF in Equation 2.8 and 2.9 respectively, allows to estimate the irradiation and DC yield potential of a solar road, considering real traffic data.

4.2.2. Application to the case studies of A16 and A12

Despite the great potential availability of traffic data, it was not possible to apply real data to all the national highways. This was mainly due to the large size of shared data and the restriction in time to process them.

Nevertheless, the traffic shading model has been applied for the two case studies of the motorway A16 and A12 in order to correct their effective irradiation potential and to observe the effect of traffic on their energy output. According to a study of Statistics Netherlands (Centraal Bureau voor de Statistiek, CBS), these motorways are within the top 5 busiest roads in the entire country [2].

The position of the two highways in the national map can be seen in Figures 4.10 and 4.11. The highway A16 connects the city of Rotterdam with the Belgian border. From the available traffic data, an average flow of 677 vehicles per hour has been recorded in 2018, as depicted in Figure 4.12. The A12 goes from The Hague to the eastern German border. The model counted an average of 713 with peaks of almost 2,300 vehicles per hour in 2018, as it can be observed in Figure 4.13.

4.3. Temperature

Temperature influences the PV module performance in such a way that an increase in the temperature of a solar cell leads to a slight increase of short circuit current, but a relevant drop in open-circuit voltage, reducing significantly the conversion efficiency [20]. As already mentioned, the temperature of a rooftop installed PV module is influenced by the irradiance intensity on the array received from the Sun, the convective heat exchange with the environment in both the front and rear sides (dependent on the ambient temperature, wind speed and more other aspects), the radiative emission from the top surface, and the conductive heat transfer between the module and the mounting structure.

In the case of a solar road, the thermal behaviour of the module needs to be considered differently. Since the cells are placed between an anti-skid layer and the asphalt, the cooling

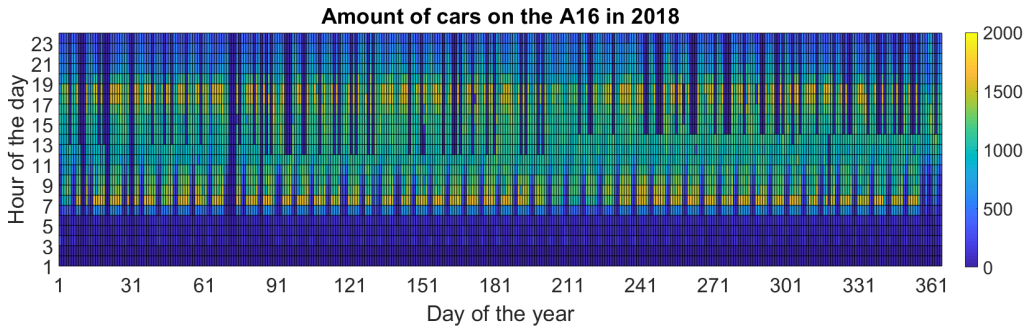

Figure 4.12: Vehicles per hour passing on the A16 throughout the year (data of 2018)

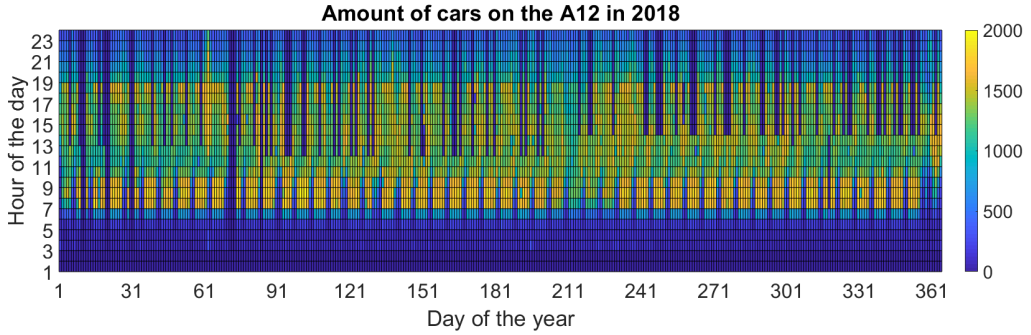

Figure 4.13: Vehicles per hour passing on the A12 throughout the year (data of 2018)

effect of wind and surrounding air on the rear side does not take place in a solar road module. On the other hand, the underneath soil absorbs the heat with high thermal inertia, playing the role of heat sink [19]. Therefore, thermal models mentioned in Chapter 2.2.1 cannot be directly applied to a solar road.

In [68], V. Kumaravel developed a thermal model to estimate the temperature of the solar cells in the TNO SolaRoad concept. The model was built upon the fluid dynamic model of M. Fuentes [42] with the integration of conductive heat exchange and the formation of the temperature gradient between the layers. This model has been adjusted for this research project and applied to generate the DC yield coefficients for solar roads in the Netherlands.

4.3.1. Temperature model

In addition to the material intrinsic thermal properties (conductivity and capacity), the temperature of the solar road modules depends on the following factors:

Solar irradiance: The module receives heat from the Sun and this is absorbed depending on the absorptivity of the module. The absorptivity β of the module depends on the reflectivity r of its surface, the absorptivity of the above ASL α and the conversion efficiency η, based on Equation 4.10 [68].

$$\beta = (1 - r - \alpha) \cdot (1 - \eta) \tag{4.10}$$

In fact, the more light is reflected, the less reaches the module surface and the more light is converted into electricity the less energy is available to heat up the module.

The result of $1 - r - \alpha$ is the actual transmittance of the anti-skid layer. In [68], Kumaravel conducted an optical study of the effective ASL transmittance for the case of the TNO SolaRoad. This is found to be isotropic[2] and to vary only depending on the angle of incident. Since no similar experiment has been conducted for a different solar road technology so far, it is assumed that the same values apply here.

The results of Kumaravel optical analysis are depicted in Table 4.1. In the case of this research project, it is chosen to approximate these values to a third-order function. In Figure

[2]It is uniform for all the orientations.

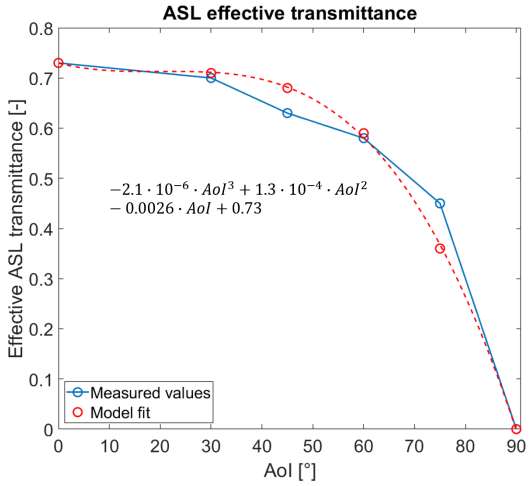

Figure 4.14: Variation of the ASL transmittance depending on AoI. The full line represents the measured data and in dotted line the adapted function.

4.14, the modelled values of the ASL effective transmittance are plotted for different AoI. The approximation causes a maximum deviation of 9% from the interpolation of the measured values.

Table 4.1: Effective transmittance of TNO SolaRoad ASL (Values from [68])

AoI	τ_{eff}
0	0.73
30	0.70
45	0.63
60	0.58
75	0.45
90	0

Wind speed and ambient temperature: The wind and ambient temperature drive the convective heat exchange between the solar road surface and the environment. Wind speed results to be less relevant than for conventional rooftop modules since the wind shear logarithmically increases with the altitude [47].

Since the wind speed is generally measured on a higher altitude than the ground level, it needs to be corrected. The power-law used in many PV system modelling to correct wind speed is inaccurate for heights above 60 m [3] [47] but may still be applied for conventional rooftop applications. However, the error increases for solar roads, which are mainly placed at ground level. Therefore, the logarithmic wind profile of Equation 4.11 is preferred to correct wind speed data.

$$U(h) = U(h_{ref}) \cdot \frac{ln(\frac{h}{z_0})}{ln(\frac{h_{ref}}{z_0})} \tag{4.11}$$

where $U(h)$ is the wind speed at height h, h_{ref} is the height at which the wind speed $U(h_{ref})$ has been measured, and z_0 is the so-called terrain or surface roughness length that indicates the friction of the wind with the ground for different types of landscapes.

Figure 4.15 summarizes the heat exchange processes that take place within the solar road layers. A one-dimensional heat transfer is considered since all the materials have low thermal conductivity and because the dimensions of width and length are much bigger than

[3] The so-called blending height is the height above which the local terrain roughness does not affect wind speed anymore.

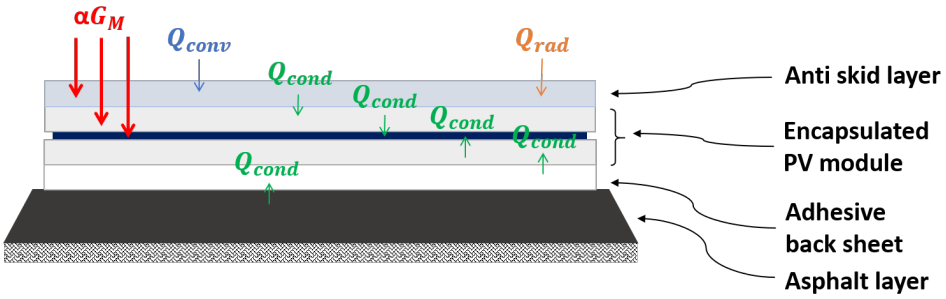

Figure 4.15: Heat transfer within a section of the solar road

thickness. As it can be observed, the module itself receives energy from the solar irradiance G_M which is partly reflected, partly converted into electricity and partly absorbed and converted into heat. In the case of solar roads, the irradiance that reaches the module is the one that has been already transmitted through the ASL and the front foil of encapsulation. Additionally, the module heats up via conductive transferred heat from layers above and below.

The ASL is the only layer subjected to convective, radiative and conductive heat transfer. This results in

$$0 = Q_{irr} + Q_{cond} - Q_{conv} - Q_{rad} \tag{4.12}$$

where

$$Q_{irr} = \alpha \cdot G_M \tag{4.13}$$

$$Q_{cond} = \frac{\lambda}{d_{ASL}} \cdot (T_{foil1} - T_{ASL}) \tag{4.14}$$

$$Q_{conv} = H_c \cdot (T_{ASL} - T_{amb}) \tag{4.15}$$

$$Q_{rad} = H_{sky} \cdot (T_{ASL} - T_{sky}) \tag{4.16}$$

With

Q_{irr} the energy from the Sun irradiance on the POA

Q_{cond} the conductive heat exchange between the ASL and the front foil

Q_{conv} the convective heat exchange between the ASL and the environment

Q_{rad} the radiative heat exchange between the ASL and the sky

λ the thermal conductivity of the layers' material

d_{ASL} the thickness of the ASL

T_{foil1} the temperature of the front encapsulant

T_{ASL} the temperature of the ASL

T_{amb} the ambient temperature

T_{sky} the sky temperature

H_C the convective heat transfer coefficient

H_{sky} the heat transfer coefficient due to radiation from the sky

The signs used in the equations depend on the definition of the heat transfer direction. In this case, a positive sign indicates an energy input in the layer, while a negative sign indicates an energy output.

The heat transfer coefficients can be obtained from the profile of the ambient temperature, the sky temperature and the emissivity of the module surface, as explained in detail in [42]. The sky temperature is dependent on the ambient temperature, following the concept that in a cloudy day, the sky temperature will be closer to the ambient one, while in a perfectly clear sky, it will be higher. Equation 4.17 from [42] has been adapted for the weather conditions of the Netherlands. The average clearness index in the country is approximately 0.4 [8]. Therefore, it can be concluded that cloudiness or haziness decreases the difference between ambient temperature and sky temperature in an average day of 50%, assuming that a clear sky has an index of 0.9. This lead to define T_{sky} as

$$T_{sky} = 0.4 \cdot (0.552 \cdot T_{amb}^{1.5}) + 0.5 \cdot T_{amb} \tag{4.17}$$

In the layers below the ASL, the thermal model is based on a steady-state energy balance method explained in Figure 4.16. The solar road is subdivided into the different composing elements and an energy balance is applied to each of them. The system is considered in steady-state when energy inputs balance energy outputs, or when the rate of energy content change is equal to zero.

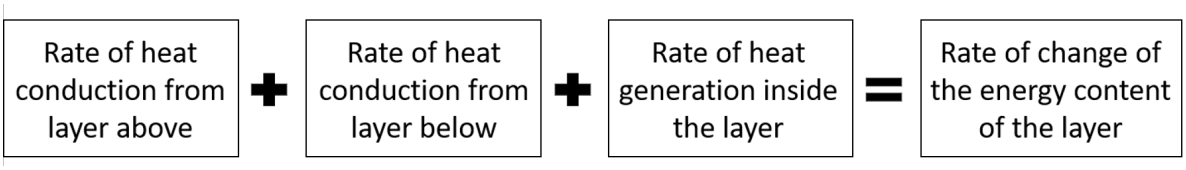

Figure 4.16: Steady state energy balance equation of the solar road layers

The assumptions made for coefficients and thermal properties are listed in Table E.2, Appendix E.

4.3.2. Generation of DC yield coefficients for solar roads

The temperature model described in Chapter 4.3 is applied in the DC yield model introduced in Chapter 2.2.3 for three different PV technologies: mono c-Si, poly c-Si and CIGS, assuming the technical specifications indicated in Table 4.2.

Table 4.2: Technical specifications of the three different PV technologies assumed as input in the temperature model

	Mono c-Si	Poly c-Si	CIGS
η_{eff}	20%	16%	10.5%
V_{OC} [V/m^2]	45.3	44.7	45.3

In order for the results to be compared with the scarce literature, the modules parameters correspond to the ones assumed in the work of A. Shekhar et al. [19], where the author studied the implementation of three different PV technologies for SolaRoad. In the case of this research project, the dimension of solar road modules is unknown and the estimation of DC yield needs to be obtained in kWh/m^2/y. Therefore, the following modifications in the assumptions of Shekhar are made:

- to obtain the number of cells n_{cell} in a square meter, 1 m^2 is divided by the area of the cell A_{cell}, so that

$$n_{cell} = \frac{1}{A_{cell}} \tag{4.18}$$

- assuming that all the cells are connected in series, the V_{OC} of the module is replaced by the $V_{OC,cell}$ of the single PV cell multiplied by the number of cells per square meter, so that

$$V_{OC} = V_{OC,cell} \cdot n_{cell} \tag{4.19}$$

  assuming no voltage drop over the interconnections.

Table E.1 in Appendix C reports all the assumptions made for the different PV technologies.

Tables 4.3 and 4.4 report the obtained coefficients. In this case, as well, the Netherlands is divided into the same two sections considered for irradiation coefficients, as already shown in Figure 3.9. It can be noticed again that, with an assumed 0° tilt angle, no ground reflectance is considered. Therefore, the coefficient d_5 results to be zero.

Table 4.3: DC yield coefficients for South-West Netherlands

PV Technology	d_1	d_2	d_3	d_4	d_5	Sum
[0° Tilt]	[kW/m^2/y]	[kW/m^2/y]	[kW/m^2/y]	[kW/m^2/y]	[kW/m^2/y]	[kW/m^2/y]
mono c-Si	108	33	-19	79	0	201
poly c-Si	86	27	-15	63	0	160
CIGS	56	18	-10	41	0	105

Table 4.4: DC yield coefficients for North-East Netherlands

PV Technology	d_1	d_2	d_3	d_4	d_5	Sum
[°]	[kW/m^2/y]	[kW/m^2/y]	[kW/m^2/y]	[kW/m^2/y]	[kW/m^2/y]	[kW/m^2/y]
mono c-Si	94	56	-35	79	0	194
poly c-Si	74	46	-29	62	0	153
CIGS	48	30	-19	41	0	100

The column that indicates the sum of the coefficients reveals the maximum DC yield output that can be expected by the PV module (0° tilt angle) and technology considered. It can be observed that for the South-West part of the Netherlands, poly c-Si solar roads can generate up to 160 kWh/m^2 in a year. The output can rise to 201 kWh/m^2 with a mono c-Si or be limited to 105 kWh/m^2 if CIGS is implemented. The same analysis can be applied to the North-East part of the Netherlands.

Table C.3 in Appendix C shows the coefficients generated by applying the DC yield model to the technology of TNO SolaRoad. Figures 4.17a and 4.17b depict the variation of temperature in Delft throughout the year for a glueable solar road and for a TNO SolaRoad poly c-Si module, respectively.

In fact, the temperature deviation from STC reduces of around 2% the maximum DC yield potential of the solar road technology, whereas for conventional modules the deviation is generally assumed to be around 6% [20]. Further research into the properties of the materials used need to be conducted to explain this difference in a satisfactory manner. However, it is already known that the ground plays an important role as heat-sink.

It can be noticed that in the case of the TNO SolaRoad the module temperature fluctuates more, reaching higher temperature (up to 60 °C) in comparison with the glueable solar road technology. For this reason, the estimated annual DC yield output of the TNO SolaRoad decreases about 8 kWh/m^2, 6 kWh/m^2 and 3 kWh/m^2 for mono c-Si, poly c-Si and CIGS, respectively, in respect to the assumed glueable solar road technology. The difference is not considered relevant, but it seems from the results that the glueable solar road technology is less responsive to ambient and soil temperature. Further research into how the temperature model performs when applied to the assumed technology need to be conducted. Since the assumed glueable solar road technology is solely based on assumptions and literature research, it is reasonable to think that in a real application its performance would result rather different than the simulated one. However, one reason can also be that the assumed glueable technology is around 6 times thinner than the TNO SolaRoad. This could significantly reduce the heat accumulation potential.

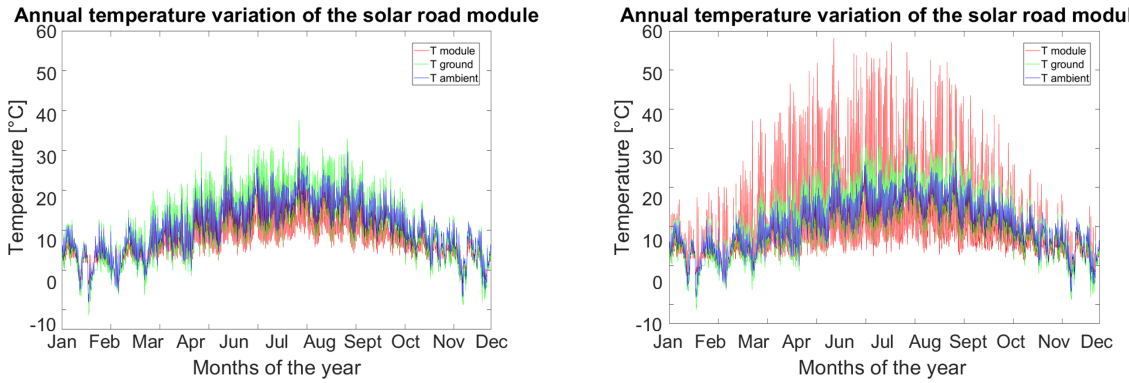

(a) Glueable solar road module (b) TNO SolaRoad module

Figure 4.17: Temperature variation of solar road modules simulated in Delft for one year

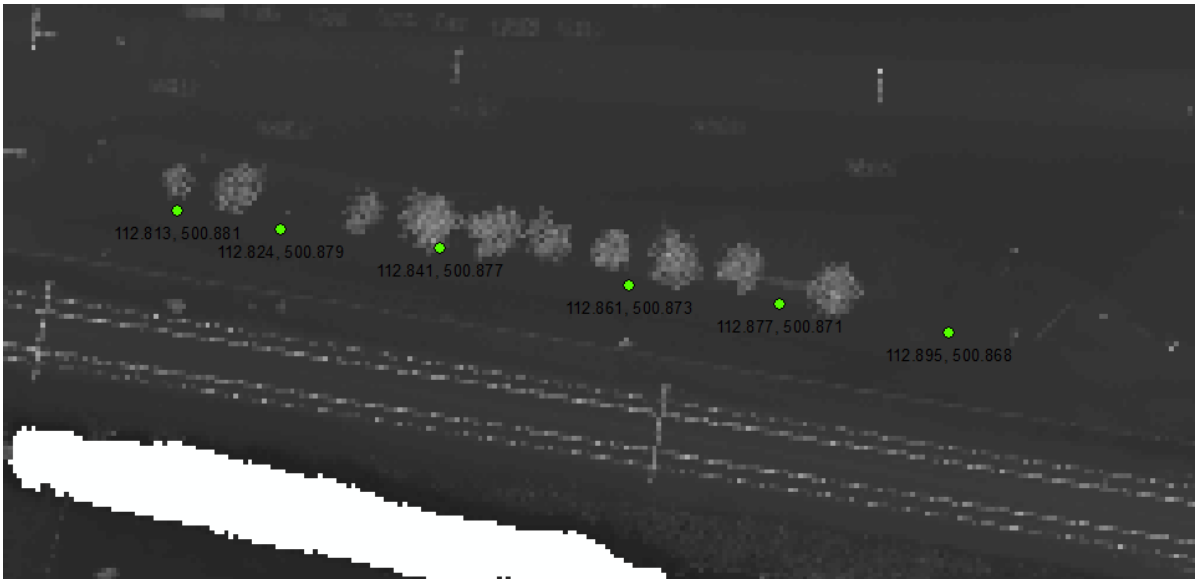

Figure 4.18: Location of the TNO SolaRoad in Krommenie, Amsterdam, represented in LiDAR. The green points indicate the six analyzed sites.

4.4. Comparison with TNO SolaRoad model

As already mentioned, data availability about solar road performance is scarce, due to the fact that not so many installations are actually available for monitoring, but also because data are mainly held by private. For these reasons, it was very hard to find a suitable validation case for the modified DC yield model.

Nevertheless, a comparison with the TNO SolaRoad simulation conducted by A. Shekhar in [19], and already mentioned in Section 2.1.4, is made in order to evaluate the model results. The six points along the TNO SolaRoad installation and indicated in Figure 4.18, are analyzed. Their DC yield for the three different PV technologies (mono c-Si, poly c-Si and CIGS) is calculated applying the TNO SolaRoad coefficients and compared with the values obtained by the simulation conducted in the paper. Table 4.5 gives an overview of the comparison results.

The deviation of the obtained DC yield values from the one indicated in the paper of A. Shekhar varies from a minimum of 6% to a maximum of 17% for mono c-Si, from 7% to 23% in the case of poly c-Si and from 5% to 28% if CIGS is considered.

It can be stated that the Shekhar's model results always lie in the range of the DC yield values calculated for the six points. In particular, results in Point 3 show to good correspond with the literature. However, the exact location where the model was applied is not known.

Table 4.5: Comparison between the DC yield results of the TNO SolaRoad model in [19] and the results obtained with TNO SolaRoad DC yield coefficients. The points are numerated from left to roght. The * indicates the results of Point 6, which is at the edge of the new section of the SolaRoad and it is therefore not representative for the comparison.

DC yield [kWh/m^2/y]	Shekhar's model	Point 1	Point 2	Point 3	Point 4	Point 5	Point 6	Deviation [%]
mono c-Si	142	154	163	114	149	154	179*	6-17 (24*)
poly c-Si	99	123	130	91	119	123	143*	7-23 (35*)
CIGS	64	82	86	60	79	81	95*	5-28 (38*)

The paper only indicates the location of "Krommenie" as reference for the location where the model is applied. Therefore, it is difficult to compare the results, as they might be affected by different skyline profiles.

5

Results and discussion

In this chapter, the improved model is applied in different locations to observe its sensitivity to latitude and tilt angles. It follows the presentation of the results of the irradiation and DC yield potential estimation for the Dutch highways network. Mean, maximum and minimum values, together with standard deviation, are provided for the analyzed roads. The three most irradiated highways are indicated and their DC yield output potential is provided. A closer look is given at the A10, ring road of Amsterdam, where optimal and unsuitable locations are both discussed in order to show the function of the irradiation map. A comparison with the output of a conventional PV installation is provided as well. Eventually, the results of the traffic shading model are presented. The average time in which solar road modules could be covered by passing vehicles is estimated, together with the impact of irradiation and DC yield potential of the road A12 and A16. Two examples of situations in which traffic can be considered as a relevant shading source are also given.

5.1. The effects of the optical air mass correction factor

In absence of atmosphere, the distribution of solar radiation at the poles would almost be the same as at other lower latitudes, only less continuous on an annual basis. The weather and the amount of air that the sunlight needs to cross variegate the solar radiation received on Earth mainly based on the location's latitude [48]. In this report, the influence of optical air mass on the coefficient-based irradiation model introduced in Chapter 2.2.2 are studied on the Equations and theoretical knowledge explained in 3.1.1.

In addition to the two locations selected in the work of A. Calcabrini [13], Delft (The Netherlands) and Antofagasta (Chile), two other cities are considered, Reykjavik (Iceland) and Bata (Equatorial Guinea). This is done in order to explore the sensitivity of the corrected model for higher and lower latitudes, respectively. The coordinates, together with the average elevation of the chosen locations are listed in Table 5.1 and are indicated on a world irradiation map in Figure 5.1.

Table 5.1: Coordinates and average elevation of the analyzed locations

	Delft	Antofagasta	Reykjavik	Bata
Coordinates (WGS84)	52.01,4.357	-23.433,-70.433	64.14,-21.948	1.852,9.774
Elevation [m]	0	154	15	4

For each of these cities, a comparison is conducted between the coefficients obtained with the original model (where no AM correction factor is applied) and with the improved version. The results of the analysis are shown in Figure 5.2 and the table with the values can be found in the Appendix B, Table B.4.

From the results, it can be observed that applying a correction factor based on the optical air mass improves the coefficients for low tilt angles. In particular, for higher latitudes (Delft

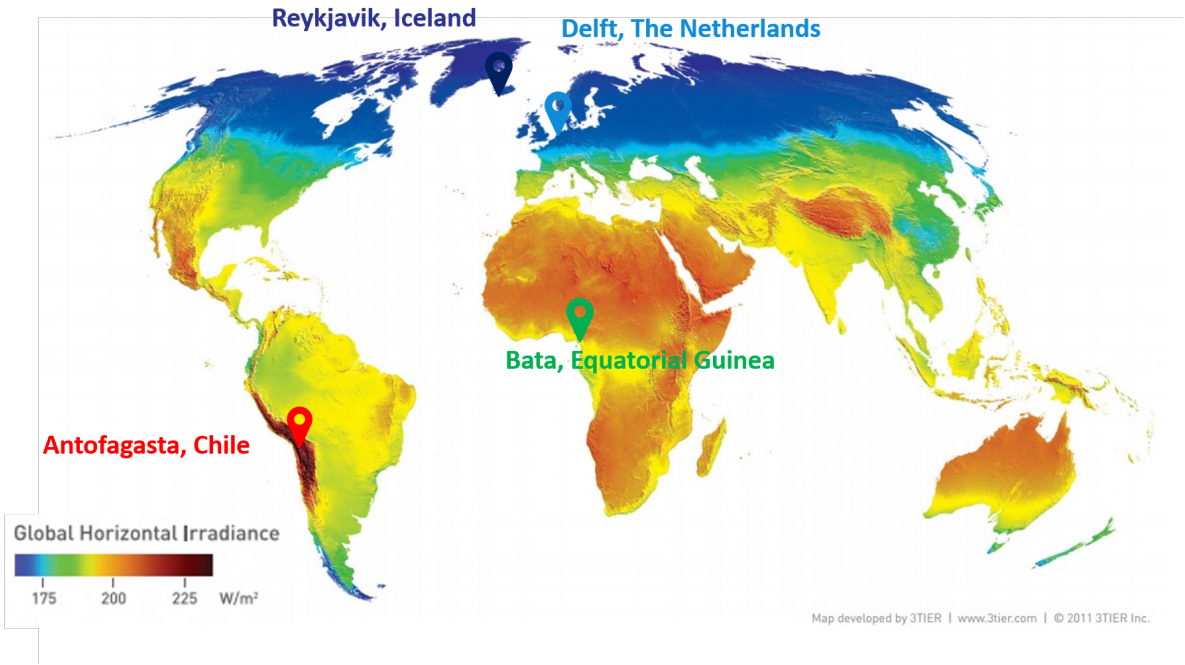

Figure 5.1: Irradiation world map with the analyzed locations

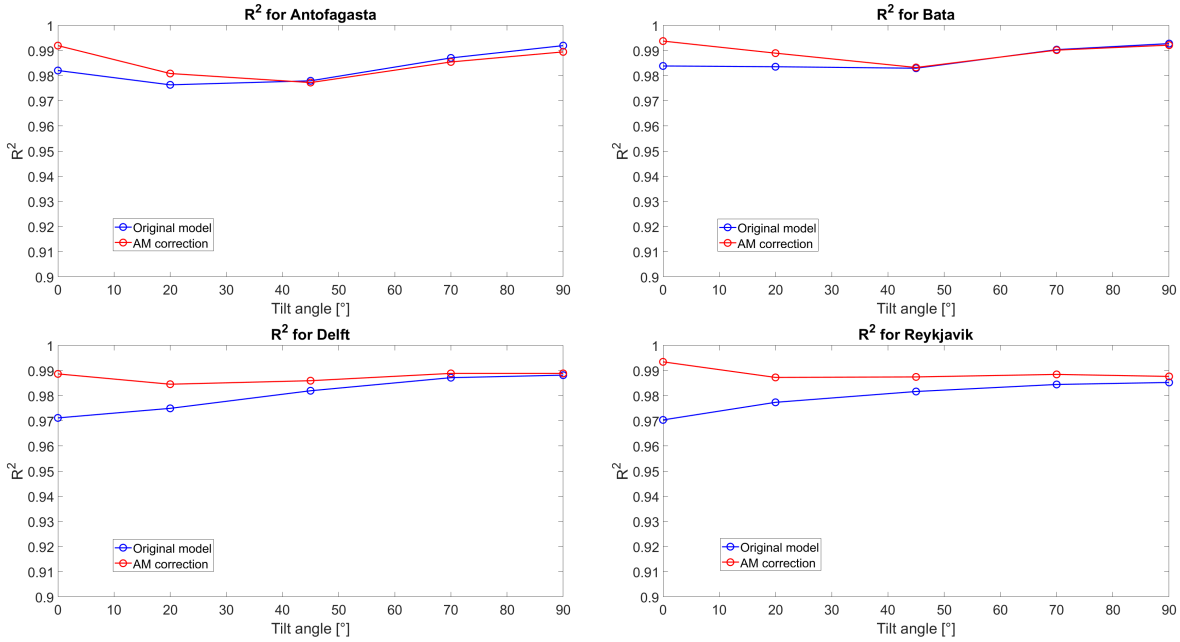

Figure 5.2: Improvement of accuracy in the model with implementation of the AM correction factor

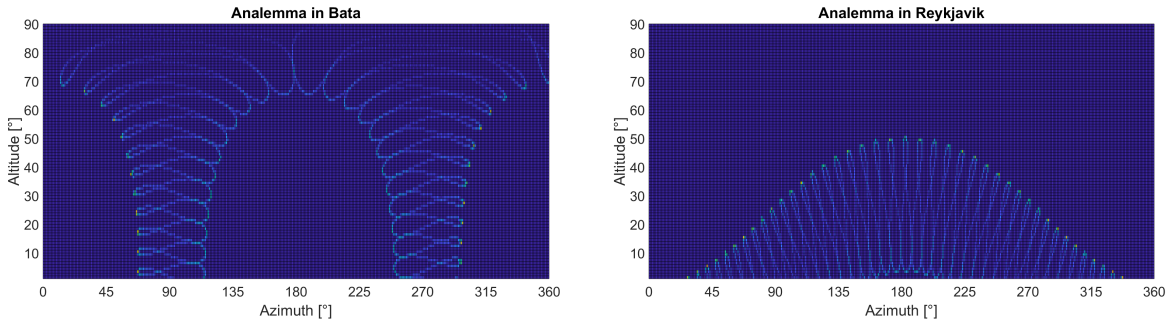

Figure 5.3: Analemma in the city of Bata (left) and Reykjavik (right)

and Reykjavik), the accuracy of the model stabilizes on a constant value around 0.99, whereas in the original model it was linearly decreasing with the tilt angle. In the case of lower latitudes (Antofagasta and Bata) the improvement of the model is less significant.

In general, the AM correction factor principally impacts on high latitude locations, improving the accuracy of the model for low tilt angles. This is because not considering the AM correction factor overestimates the radiation at high zenith angles (when the sun is low on the horizon) in the original model. The conditions of high zenith angles for Sun altitudes are more often in the case of Delft and Reykjavik since they are located at higher latitudes, as it can be observed in Figure 5.3. In fact, due to the inclination of Earth axes, the Sun path covers significantly more often lower altitudes in winter in comparison with summer. On the other hand, Antofagasta and Bata do not show similar variations in sun altitude throughout the year, since they are located close to the equator. Therefore, the overestimation of direct sunlight at high zenith angles has a lower impact on the irradiation estimation at these latitudes.

The same can be said for low module tilt angles. For a module placed horizontally on the ground (0° tilt), the share on total POA irradiation is higher for the diffuse than for the direct component. This is due to reflections and higher AoI. An overestimation of the DNI reduces the accuracy of the total irradiation estimation for these modules. Introducing the AM correction factor improves the correlation with real data.

It follows that, for lower latitude, the POA irradiation received by a 0° tilted module will be more influenced by DNI than on higher latitudes. Therefore, the improvement of the model is less relevant at lower latitudes for low tilt angles than at higher latitudes.

5.2. The effects of the optical AoI correction factor

The major improvement to the model accuracy is given by the AoI correction factor. After the application of the AoI correction factor for 0° tilted modules, 98% of the results fell within 5% of relative deviation from the simulated values. In comparison, the previous version of the model was giving a 5% range of relative deviation for only 65% values. Figure 5.4 compares the accuracy of the two model versions.

5.3. Solar road irradiation map of the Netherlands

First of all, an analysis of the SVF along the Dutch highways has been conducted to observe the impact of the skyline profile on irradiation potential. Table C.1 in Appendix C reports the statistics for all the analyzed roads. Overall, it can be stated that highways are generally in almost free horizon conditions. On average, they show an SVF of 0.9 and maximum values of 0.99 that can be found in all the analyzed roads. Minimum values close to 0 can be found but are mainly correlated with distorted data (see Section 3.2.2). They account anyway for a very small share of the measured points. As an example, in the case of A16, only 0.7% of the points show an SVF lower than 0.1, while almost 65% of the points is found to have an SVF larger than 0.9. Although A 65 does not cross significantly built-up areas, it shows the lowest average SVF of 0.78. Figure 5.5a represents how this reduction of the sky view is

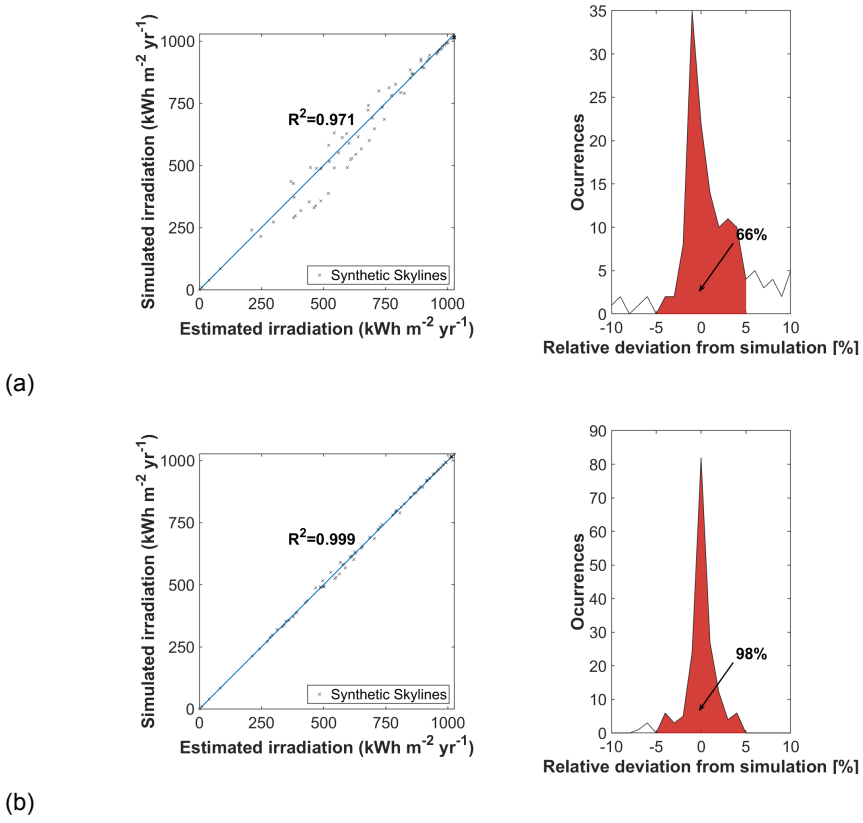

Figure 5.4: Comparison of the relative standard deviation and coefficient of deviation for the original (a) and improved (b) version of the irradiation model for 0° tilted modules (Images generated from the original model, kindly concessed by A. Calcabrini [13])

instead due to the trees aligned along the entire road. Figure 5.5b gives a comparison of a 0.9 SVF skyline profile.

The irradiation model explained in Chapter 2.2.2 has been applied to the Dutch highways, using different irradiation coefficients for roads situated in the South-West and in the North-East part of the country. Figure 5.6 shows the graphic results of the model, where the simulations conducted every 100 meters length and 15 meters width are here interpolated. As explained in the legend, the following rule is applied: the more irradiation a solar road section receives, the closer to yellow it is represented. Irradiation maps classify the points in five classes of annual irradiation applying the Jenks Natural Breaks classification method, as represented in Figure C.1, in Appendix C. The method classifies the values in class breaks that minimize the within-class variance and maximize the between-class difference. This was chosen to allow a meaningful evaluation of optimal sites in terms of energy output and discard values under a minimum range of interest.

The irradiation potential map of solar highways in the Netherlands can be provided in digital version upon reasonable request with precise values for each analyzed locations.

Table C.2 in Appendix C gives the statistics of irradiation for each analyzed road. Overall, the Dutch highways show an average irradiation potential of 882 kWh/m^2/y and a maximum peak on A73 of 1026 kWh/m^2/y. The top three most irradiated highways are reported in Table 5.2.

However, there are several locations in which the irradiation potential has been observed to drop. From further analysis, it has been recognized that reduction of irradiation potential is mainly caused by the following four factors:

- Underpassage at interchanges and bridges
- Tree-lined avenues

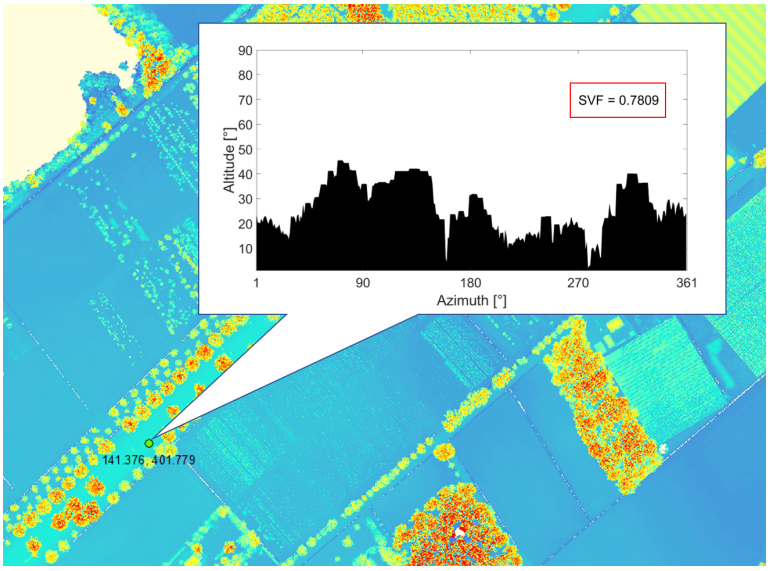

(a) Skyline profile along the A65

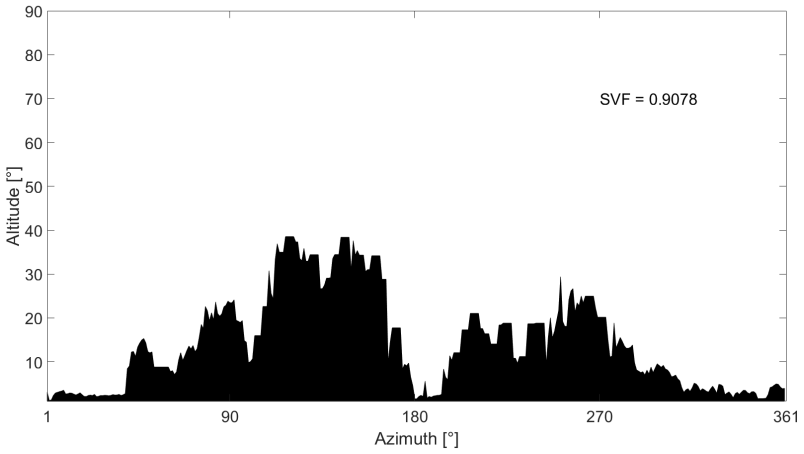

(b) Skyline profile with SVF 0.9

Figure 5.5: Examples of skyline profiles along highways

- Urban environment (mainly buildings)
- Distorted data (traffic shields, cable lines, etc.)

The highway A10 around Amsterdam represents a good example to be further analyzed. Assumed that the municipality already decided to launch a solar road trial along the ring road, the map representing the irradiation potential of highway A10 is very useful at this stage. Figure 5.7 depicts the irradiation of A10 and main injecting highways. The road shows average irradiation of 881 kWh/m^2/y, with a peak around 1022 kWh/m^2/y in the areas of Watergraafsmeer, Ringweg Oost.

The two areas circled in black on the map represent two underpasses, where the road passes below the canal. Obviously, these two locations do not represent a considerable option. Another area where the construction of a solar road is not advised would be the section indicated with the number 1. Figure 5.8a shows more in details that trees are planted along the road in the interchange and that another road is intersecting the A10 in this stretch on a bridge. These elements are the cause of shading of the road surface and decrease therefore the irradiation potential in the area to an average of 670 kWh/m^2/y and a minimum of 440 kWh/m^2/y.

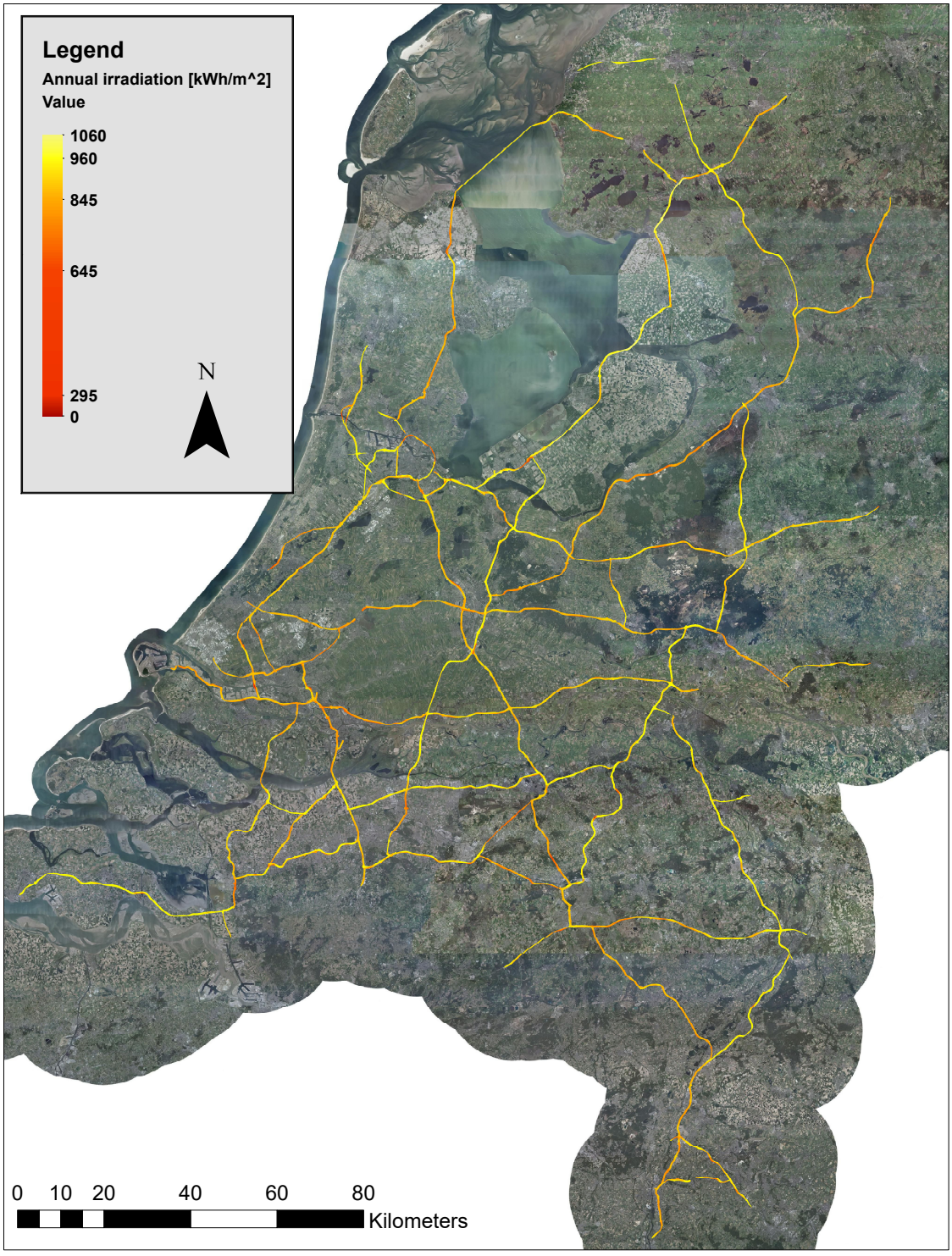

Figure 5.6: Map of the irradiation potential for solar highways in the Netherlands

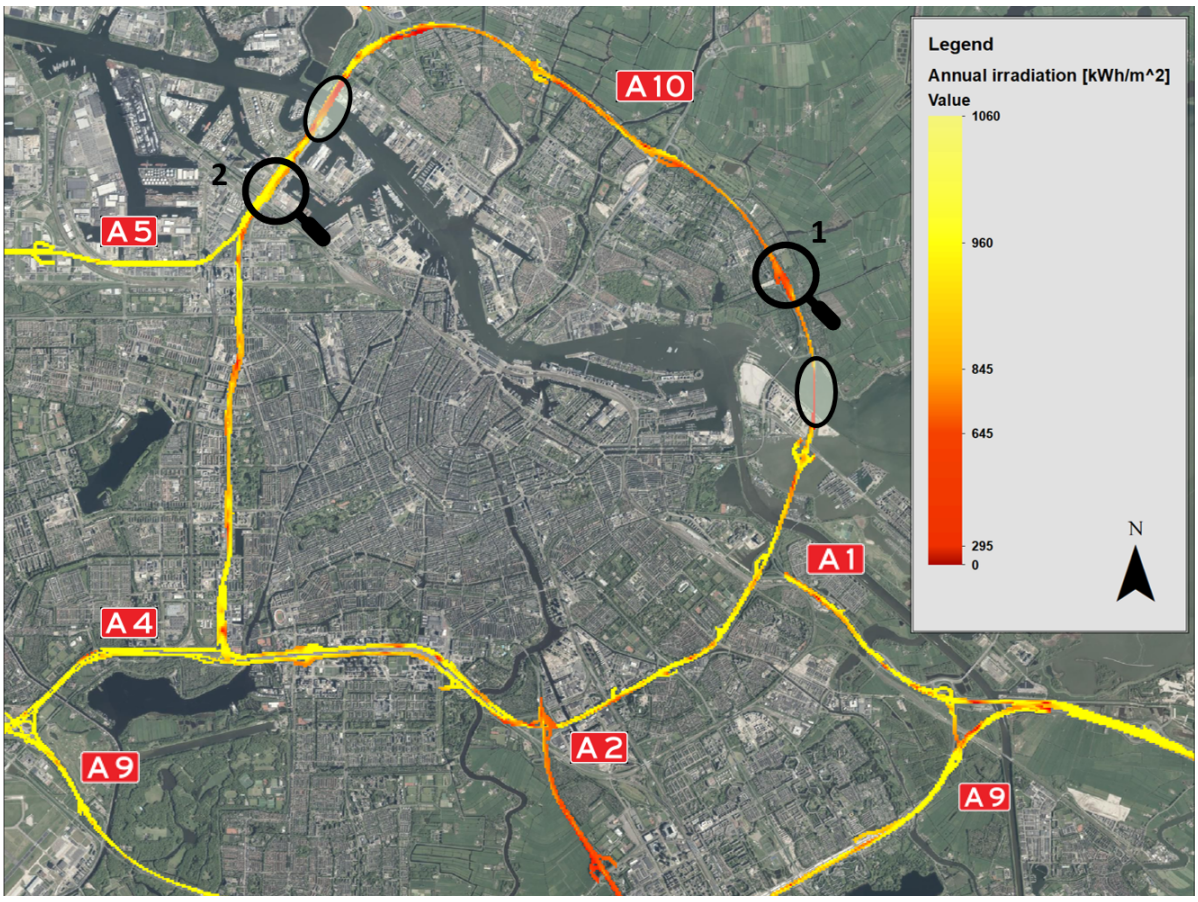

Figure 5.7: Irradiation potential map of the A10 and main injecting highways

Table 5.2: Top three highways in the Netherlands for annual average irradiation per m^2

Road	Average irradiation [kWh/m^2/y]	Description
A31	1002	The road connects the A7 near Zurich to the A7 near Drachten and mainly crosses cultivated lands
A5	999	The road was born as a by-pass for the city of Amsterdam to relieve the surrounding motorways from traffic towards the capital. Since the highway does not have any other aim than the city, it crosses a free horizon countryside in the West of Amsterdam
A200	983	Crossing no built-up areas

On the other hand, the section indicated with number 2 represents an appealing location for solar road testing. Figure 5.8b shows that the area is situated away from buildings or other possible shading objects and also that the carriageway widens in the section, offering more irradiated surface. Section number 2 has an average irradiation potential of 940 kWh/m^2/y (almost 30% higher than in section number 1) and reaches points of over 1020 kWh/m^2/y, close to the maximal annual irradiation achievable in the South-West region of the Netherlands (1026 kWh/m^2/y).

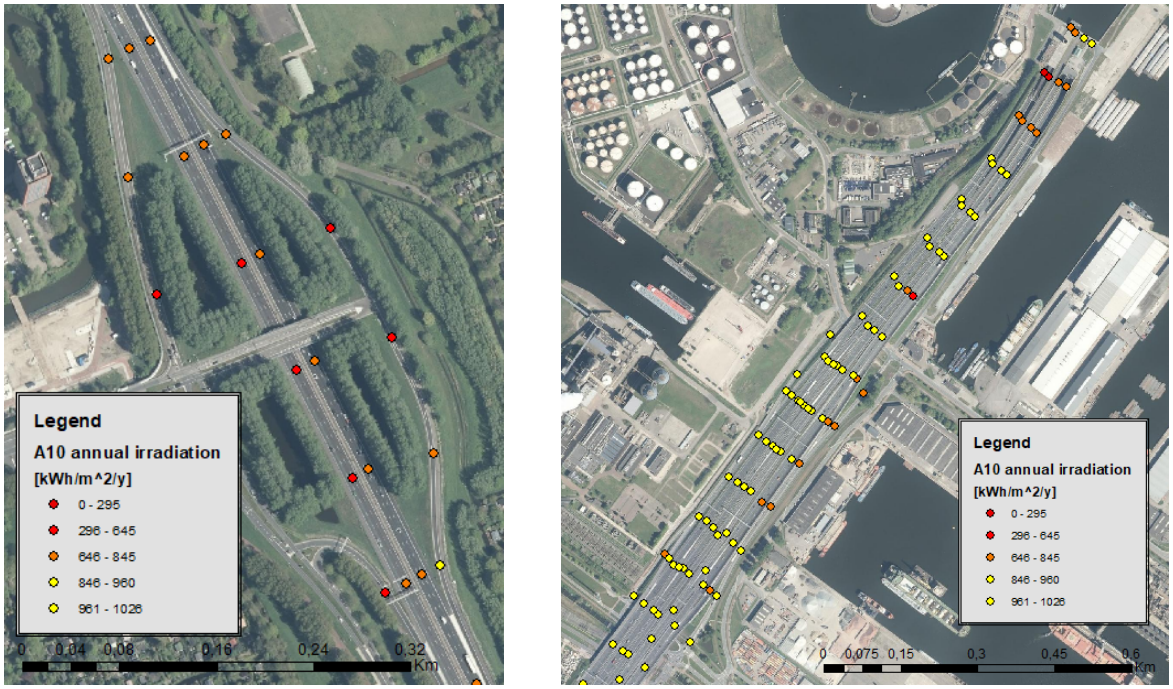

(a) Section number 1 of A10

(b) Section number 2 of A10

Figure 5.8: Details of the irradiation potential for the two analyzed sections of A10

5.4. Solar road DC yield map for the Netherlands

The DC yield model explained in Chapter 2.2.3 has been applied to the Dutch highways, using the DC yield coefficients for roads situated in the South-West and in the North-East part of the country. Similarly to the irradiation map previously represented, Figure 5.9 shows the interpolated results of the DC yield model for poly c-Si solar road modules. As explained in the legend, the following rule is applied: the higher the energy output of solar road section, the closer to green it is represented. Similarly to the irradiation potential map, the Dc yield map classifies the analyzed points using the Jenks Natural Breaks classification method, as shown in Figure C.1. The map of DC yield potential of solar highways in the Netherlands can

Table 5.3: Statistics of the DC yield potential of solar highways in the Netherlands

DC yield	mono c-Si [kWh/m^2/y]	poly c-Si [kWh/m^2/y]	CIGS [kWh/m^2/y]
Average	173.93	138.53	90.11
Maximum	200.98	160.00	104.99
Minimum	0.07	0.05	0.03
StD	13.21	10.41	6.75

be provided in digital version upon reasonable request with precise values for each analyzed locations.

Table 5.3 reports the statistics of DC yield output for the three different PV technologies. For mono c-Si, Dutch highways show an average output of 173 kWh/m^2/y and a maximum peak of almost 201 kWh/m^2/y in several sites. If poly c-Si is assumed, then the average output decreases to almost 139 kWh/m^2, with peaks of 160 kWh/m^2/y in the best locations. With CIGS, the annual DC yield is further reduced to an average of 90 kWh/m^2/y and a maximum value of 105 kWh/m^2/y. Overall, mono c-Si shows a generation potential around 25% higher than poly c-Si, whereas CIGS DC yield is on average 35% lower than of poly c-Si. This output was expected since the conversion efficiency of mono c-Si is approximately 25% higher than the one assumed for poly c-Si, whereas CIGS has a conversion efficiency of about 34% lower.

Tables C.4, C.5 and C.6 in Appendix C report the statistics of the annual DC yield output for each analyzed highway, assuming mono c-Si, poly c-Si and CIGS are provided. In the last column, the total generated output is calculated assuming that the road is completely covered by PV modules. The average DC yield is multiplied by the specific length of each road with the assumption of 15 m road width.

According to this calculation, covering the three longest highways of the Netherlands A7, A2 and A15 with solar road modules will generate almost 477, 404 and 401 GWh in a year. However, this will require to cover 240, 212 and 204 km of road surface respectively. At this stage of technology development, it is more reasonable to identify the three roads with the highest average potential (irradiation): A31, A5 and A200. Table 5.4 shows their respective average and total DC yield for the three different PV technologies. The total DC yield is again used to indicate the case in which the road is completely covered by solar roads module. In the case of A31, A5 and A200 this means a solar road of 65, 14 and 1 km respectively.

If the total surface of the Dutch highway network was covered by solar road modules, 5.2 TWh/y, 6.6 TWh/y, and 3.4 TWh/y of electricity could be generated in the case of poly c-Si, mono c-Si and CIGS module technologies, respectively. The CBS reports a national electricity consumption of 120 TWh in the year 2018 [4]. 3 to 5 % of the national consumption could be therefore obtained by solar road installations in the Netherlands. If it is assumed that 15% of electricity is consumed due to street lighting, mono c-Si solar highways would then be able to power up to 36% of the national consumption (28% and 18% in case poly c-Si and CIGS modules are installed).

Table 5.4: Top three highways in the Netherlands for annual average DC yield output per m^2

PV technology	DC yield	A31	A5	A200
poly c-Si	Average [kWh/m^2/y]	157.3	156.8	154.3
	Total [MWh/y]	153,367.5	32,928.0	2,313.9
mono c-Si	Average [kWh/m^2/y]	196.4	195.7	192.6
	Total [MWh/y]	191,451.0	41,105.4	2,888.3
CIGS	Average [kWh/m^2/y]	105.0	104.8	100.6
	Total [MWh/y]	100,025.3	21,474.6	1,509.2

It is interesting to compare the model results with a conventional PV system installation. South to the Technical University of Delft, along the A13, a virtual free-standing solar park of 6.9 MW$_p$ has been simulated since 2014. Its performance can be checked on the Dutch PV

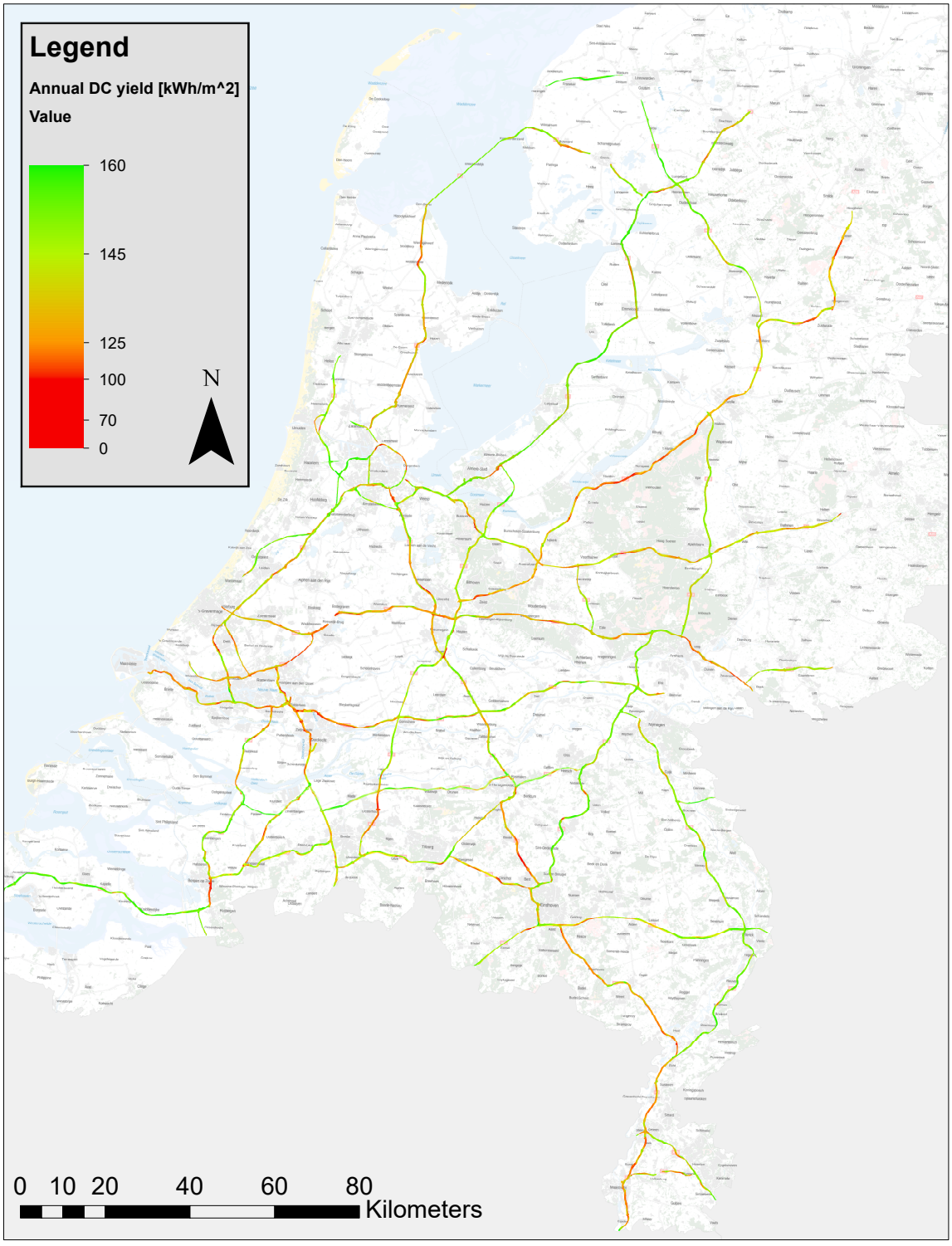

Figure 5.9: DC yield potential map for solar highways in the Netherlands. Poly c-Si modules are assumed.

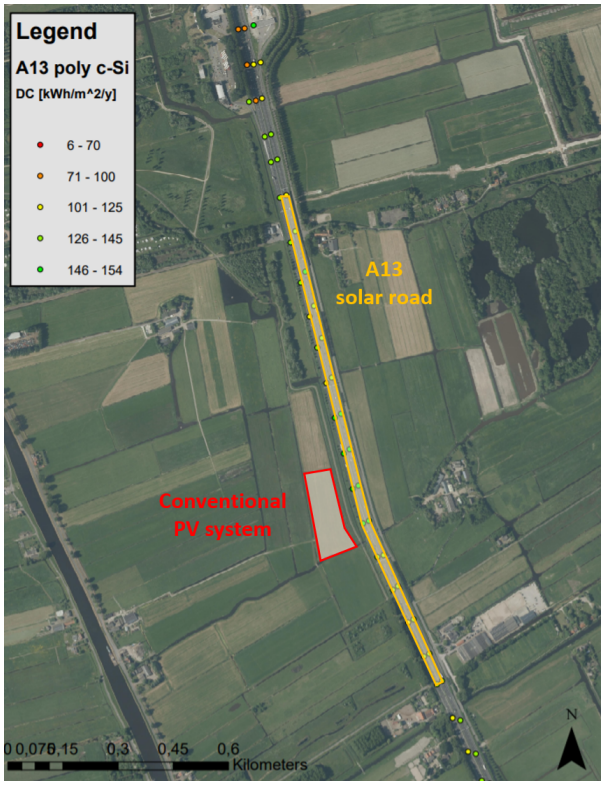

Figure 5.10: Location of the PV system case study in the south of Delft and the A13 highways section passing nearby

portal established by the university (https://pvportal-2.ewi.tudelft.nl/). The system consists of around 21 mono c-Si modules (high efficiency of 20.07%), distributed in 27,811 m^2. In 2018, the system generated around 1,184 kWh/kW_p, which can be converted into 8,168 MWh, with an average of 294 kWh/m^2.

It is now assumed to cover the same ground area with poly c-Si solar roads modules along the nearest section of the A13, as depicted in Figure 5.10. The annual DC yield output would result in 3,803 MWh/y, with an average of 137 kWh/m^2. This accounts for almost 47% of the DC generated by the conventional system. If mono c-Si would be used, the average annual DC yield would rise to 151 kWh/m^2, reaching a generation of 4,199 MWh/y. This will account for 51% of the output of the conventional PV installation. This means that to obtain the same output as the one generated by the tilted conventional modules, a double large ground area should be covered with solar road modules.

However, together with the spacial conversion efficiency, also the value of the occupied land needs to be considered. In fact, the land occupied by the PV system is not available anymore for example for agricultural purposes, such as growing potatoes.

According to the United Nations Food and Agricultural Organization (FAO), 4.57 kg/m^2 of potatoes can be grown on average in the Netherlands. Assuming a reasonable retail price of 1 € /kg, it is possible to earn 4.57 € each square meter of cultivated land. The area that the PV system subtracts from cultivation also comprehends the row spacing between the tilted modules in order to avoid mutual shading (an area that is saved in case of solar roads), which accounts for 160,490 m^2. Therefore, the total area occupied by the conventional PV system would have generated annual revenue of 732,797 € /y. Selling electricity to neighbour households at 0.17 € /kWh, would generate a revenue of 1,388,589 € /y. The net value of earnings from the land used can be therefore considered to be the subtraction of the potential food cultivation revenues from the electricity revenues. This accounts for 655,792 € /y.

The same calculation can be performed for the solar road. If mono c-Si modules were installed, its annual electricity revenues would be 713,908 € /y. On the contrary than for the field occupied by the conventional PV system, the area of the solar road would anyway

not be available for other lucrative purposes. Therefore, the net earnings from the land used simply accounts for 713,908 € /y.

Comparing the results, it can be observed how the solar road can actually generate revenues of 58,116 € /y more in comparison with the conventional ground-mounted PV system. If the comparison was conducted with a rooftop installation, the outcome of the conventional system would have probably been better. However, in this case, surface constraints would have also played a role.

5.5. The effect of traffic shading

The shading effect caused by traffic has been observed for both A16 and A12. Figure 5.11 indicates the interpolation of the cumulative traffic coverage hours obtained for every 200 meters along the A16. For the results of A12 and the irradiation map after the introduction of traffic shading, it can be referred to the maps in Appendix D. The areas indicated in red are the road sections most affected by traffic shading and are therefore the ones that show the highest reduction of the annual irradiation potential. In general, the threshold of 350 h/y has been set as the value for high traffic shading.

The maps of traffic shading time, irradiation and DC yield after applying the effect of traffic shading can be provided upon reasonable request with precise values for each analyzed locations. The map of traffic shading time classifies the points in five classes of traffic coverage time of equal range. This was chosen because secondary aspects correlated to traffic, such as haze, pollution and noise, are directly correlated to traffic intensity. In this way, a direct correlation is easier to be applied to the different classes.

It needs to be taken into consideration that the right and the left lanes behave differently since they show different traffic flows at a different time of the day. It is true that the car that drives to the office along one lane, comes back after work on the other one. However, it is also true that the two travels happen in a different moment of the day and therefore affects differently the irradiation potential of the road surface. Additionally, more complex behaviours and location-specific characteristics of the road also play a role in defining the causes of traffic on each lane.

Tables 5.5 to 5.8 report the statistics of traffic coverage time, irradiation and DC yield potential reduction along both A16 and A12. Overall, the annual average coverage time on the A12 counts for around 240 hours, varying from a minimum of 120 to a maximum of 450 h/y. This means that for a cumulative amount of 240 hours within one year on average, a point on the road is completely shaded due to traffic. This accounts for 2.7% of the hours in a year. For A16 the numbers are slightly slower, with an average coverage time of 230 hours per year (2.6% of the hours in a year), varying from a minimum of 58 to a maximum of 416 h/y.

However, what is relevant in a study dedicated to solar roads is to understand how many of these shaded hours happen at the same time as hours of sunlight. In fact, in case of a traffic jam during sunset, the coverage time of the location will equally increase as if the traffic jam occurs at noon but in the first case, the energy output of the location will be less affected by traffic shading than in the second case.

On average, the annual irradiation and DC yield reduction caused by traffic has been found to be around 3%. This is a considerable percentage, comparable with cables losses in large PV installations and needs, therefore, to be taken into consideration.

Nevertheless, there are specific locations where the reduction rises over 5% for the irradiation and to almost 9% for the DC yield and the threshold of 350 h/y of traffic shading time is overcome. On the A12, these points are located in proximity to two very large interchanges called in Dutch Knooppunt Lunetten and Knoppunt Velperbroek, located in the province of Utrecht and in the region of Arnhem, respectively. It can be stated that interchanges always attract high vehicles flows. Additionally, in the proximity of ramps[1], vehicles speed tends to reduce and the number of lanes decreases as well, generating downstream congestion. A similar effect can be observed at the exit of the highway, in the North of The Hague, where the vehicles need to slow down. These phenomena have been observed to cause a reduction

[1] A road that allows access to an interchange, also called slip road.

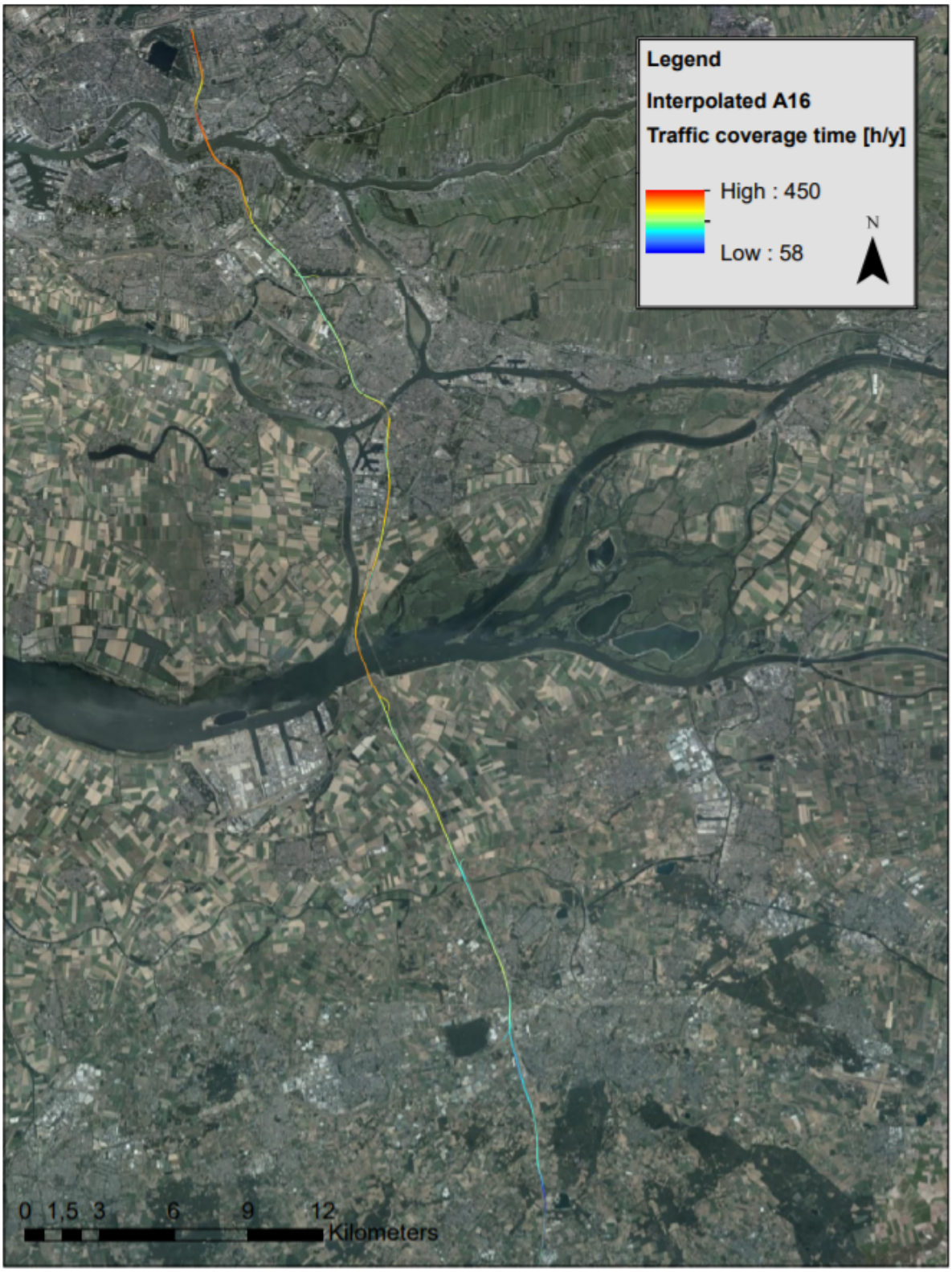

Figure 5.11: Interpolated annual traffic shading hours for A16

Table 5.5: Statistics of the effect of traffic shading on annual irradiation for left and right lane of A16

A16 Irradiation	$T_{coverage}$ [h/y]	I^Y [kWh/m^2/y]	ΔI^Y [kWh/m^2/y]	Reduction [%]
Average	233.24	895.70	26.17	2.9
Maximum	416.69	1013.39	57.34	6.1
Minimum	58.26	13.16	0.00	0.0
StD	56.56	133.97	8.47	1.0

Table 5.6: Statistics of the effect of traffic shading on annual DC yield for left and right lane of A16

A16 DC yield	$T_{coverage}$ [h/y]	E^Y [kWh/m^2/y]	ΔE^Y [kWh/m^2/y]	Reduction [%]
Average	233.24	140.64	4.08	3.0
Maximum	416.69	159.05	8.92	8.92
Minimum	58.26	2.02	0.00	0.00
StD	56.56	21.06	2.32	1.32

of received irradiation up to 50 kWh in a year.

In the case of A16, there are fewer points where the traffic coverage time surpasses the 350 h/y. In general, it can be observed that in the proximity of bridges the traffic shading effect is more significant. This is due to the fact that bridges are points of convergence for many roads that need to cross a water body.

Next subsections contain a more detailed analysis of two locations that count for particularly interesting and explanatory examples.

5.5.1. Example 1 - Knooppunt Lunetten (A12)

The interchange Knooppunt Lunetten is located in the South-East of Utrecht, close to the residential area of Lunetten Zuid. It connects A12 with A27, generating a high flow of vehicles every day. Figure 5.12 represents the interchange in an image generated from LiDAR data. The left and right lane are indicated in red with the respective flow directions. The points along the road indicate the traffic coverage time calculated every 200 m. As explained in the legend, the following rule applies: the higher the traffic shading time, the closer to red their filling colour, the higher is the cumulative time in a year in which the indicated point is completely shaded by traffic.

As it can be observed in the figure, the area on the left lane that is leaving the interchange, indicated with red and orange points, results to be the most affected by traffic shading. This means that the shading is caused by car *entering* the road section through the ramp indicated with a red line in the figure. As already mentioned, ramps (together with bridges, points in which the number of lanes is reduced and many others) represent a point in which vehicles tend to have a lower speed while accessing the highway. This tends to generate congestion at the injection point. The phenomenon causes this section of the road to present a coverage time from 340 up to 400 h/y and an annual irradiation reduction from 46 kWh/m^2/y up to 50 kWh/m^2/y (around 5%). The DC yield losses due to traffic account for up to 8 kWh/m^2/y, slightly more than 5% reduction of the total generation.

Table 5.7: Statistics of the effect of traffic shading on annual irradiation for left and right lane of A12

A12 Irradiation	$T_{coverage}$ [h/y]	I^Y [kWh/m^2/y]	ΔI^Y [kWh/m^2/y]	Reduction [%]
Average	240.76	878.70	26.80	2.9
Maximum	448.91	997.57	52.24	5.4
Minimum	123.09	10.67	0.00	0.0
StD	47.69	139.54	8.16	1.0

Table 5.8: Statistics of the effect of traffic shading on annual DC yield for left and right lane of A12

A12 DC yield	$T_{coverage}$ [h/y]	E^Y [kWh/m^2/y]	ΔE^Y [kWh/m^2/y]	Reduction [%]
Average	240.76	137.98	4.18	2.9
Maximum	448.91	156.59	8.13	6.8
Minimum	123.09	1.64	0.00	0.0
StD	47.69	21.96	1.27	1.0

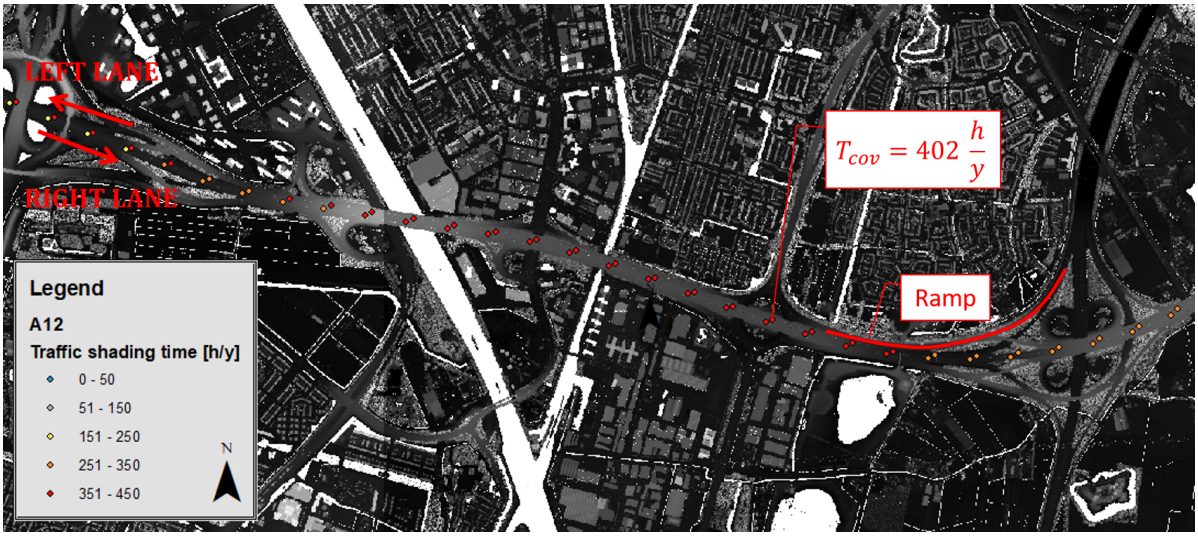

Figure 5.12: Knooppunt Lunetten in the South-East of Utrecht (1:25.000). The points along the road indicates the traffic coverage factor in the specific location

5.5.2. Example 2 - Van Brienenoordbrug (A16)

The road section of A16 in which the traffic shading time has been observed to be higher than 350 h/y is 500 m after the bridge Van Brienenoordbrug, at the exit 25 (Capelle a/d Ijssell) before an interchange. In general, traffic shading factor above 350 h/y and irradiation reduction up to 57.34 kWh/m^2/y (around 6%) has been recorded in this area. The DC yield reduction observed is up to 9 kWh/m^2/y, meaning a percentage reduction of 6% of the total generation.

Figure 5.13 represents the location in an image extracted from LiDAR data and the traffic shading time for each analyzed point is shown using the same colour map as explained in the legend. The vehicles flow directions are shown with red arrows and the point with the highest traffic coverage time (416 h/y) is indicated.

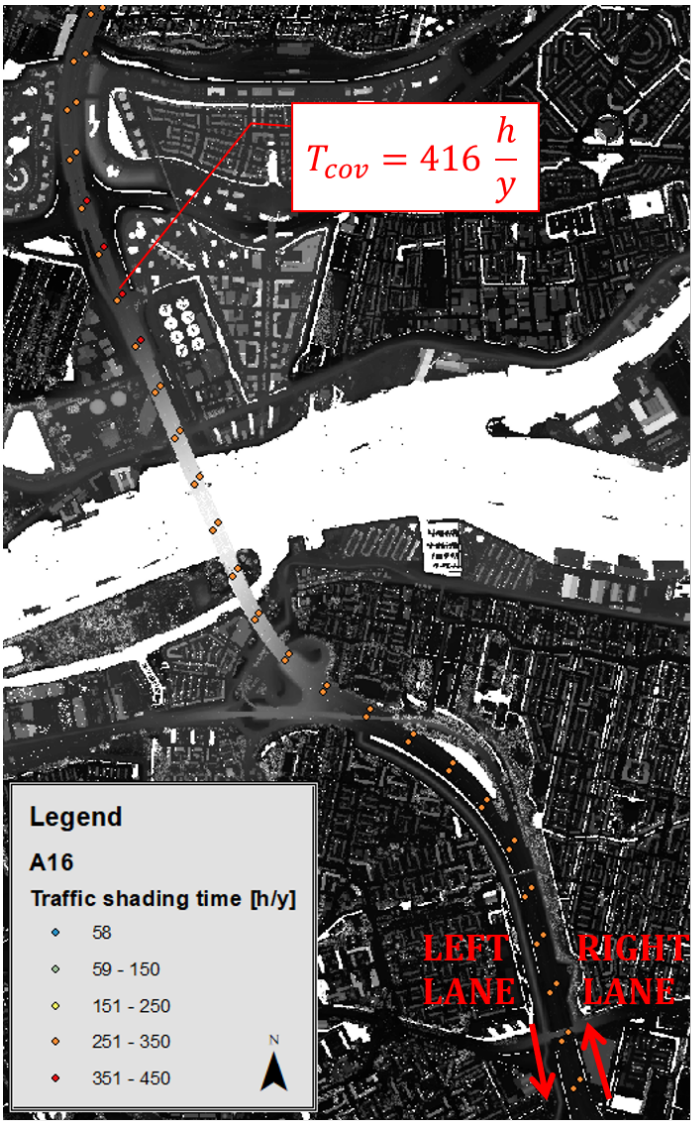

Figure 5.13: Brienenoordbrug in the East of Rotterdam (1:20.000). The points along the road indicates the traffic coverage factor in the specific location

6

Conclusions

The goal of this research project was to develop a method to estimate the irradiation and DC yield potential of solar roads in the Netherlands. The three main research objectives addressed in 1.2 are here synthesized.

6.1. Development of a method to estimate the irradiation and DC yield potential of solar highways in the Netherlands

The open-source map of the Hectopunten along the main Dutch roads was used to identify the locations of the points along the road where the model is applied. The points have a relative distance of 100 m in the length of the road and of 15 m in the width. A tool developed by M. Kaijser, described in 3.3, was applied to extract the skyline profile of these points from LiDAR data. To these points, the irradiation and DC yield model was applied.

In order to obtain the irradiation and DC yield potential of solar highways in the Netherlands, conventional approaches to obtain irradiation and DC yield values for a specific location resulted to be not effective. Therefore, another approach was chosen, the irradiation and DC yield coefficients method developed by A. Calcabrini, presented in 2.2.2 and 2.2.3. The irradiation model was improved to better simulate solar road operational conditions. This was achieved correcting the irradiance input, considering a reduction due to the optical air mass of Earth's atmosphere and due to the misalignment between the normal to the module and the sun altitude (angle of incidence). These modifications resulted in a significant reduction of sunlight reaching the solar road surface in the first 10° of altitude. With the introduction of the optical air mass and angle of incidence correction factors, 98% of the model results deviate only 5% from the values obtained with the reference model (Perez). Before, the model could give this range of deviation for only 66% of the values.

A traffic shading model was also successfully developed. The model aims to estimate the irradiation that is shaded by passing vehicles on a solar road. It is based on real traffic data provided by the Faculty of Civil Engineering and Geoscience with the research project of DiTTLAB. The data were provided for one point each 200 m, for both left and right lanes. The data of vehicles flow and speed were converted into the amount of time in which a solar road point is completely shaded by a vehicle at each hour of the day, called traffic coverage time. The traffic coverage time was used to correct the SCF and SVF into traffic coverage factor (TCF) and traffic view factor (TVF) in order to account for traffic shading in addition to the skyline profile. The model was applied to the highways A12 and A16, chosen among the four busiest roads in the Netherlands. Therefore, their traffic data deliver results of worst-case traffic scenarios for the average highways of the country.

Eventually, to account for conductive thermal exchange between the building layers of the solar road, the fluid dynamic model used to estimate conventional module temperature is also modified. The temperature model developed by V. Kumaravel to estimate the temperature variation with time of the TNO SolaRoad prototype, and described in Section 4.3, has been implemented. The input data were changed to simulate the glueable solar road technology

assumed in this research project, according to the technology assumptions mentioned in Appendix E. The modification resulted in a decrease of around 2% of the maximum DC yield potential due to module temperature deviation from STC. This deviation is lower than the one observed for conventional modules, usually assumed to be around 6% [20]. Further research into the material properties needs to be conducted to explain this difference in a satisfying way. However, it can be said that the ground plays an important role as massive heat-sink. In comparison with the TNO SolaRoad technology, deviations of 8, 6 and 3 kWh/m^2/y for mono c-Si, poly c-Si and CIGS were observed. This is probably due to the fact that the assumed glueable technology is around 6 time thinner than the TNO SolaRoad and therefore experiences less heat accumulation. However, further research and testing of the assumed technology should be conducted in order to validate the simulation results.

6.2. Evaluation of the model sensitivity

The sensitivity of the model has been evaluated for the following two aspects:

1. the increase of the azimuth step angle when generating the skyline profile, which means a reduction of the resolution of the obtained skyline profile;
2. the reduction of the analyzed point density, which means a decrease of the relative distance between the analyzed points.

The model results to be more sensitive to the variation of the skyline resolution. Increasing the step angle from 1° to 5°, 10° and 20°, increased the deviation from the reference values of irradiation to 0.2%, 1.3%, 3.7% and 7.6%, respectively. However, the increase of the azimuth step angle can significantly reduce the computational time to extract the skyline profile. The optimal balance between accuracy and number of calculations has been found at 5° azimuth step angle, where 80% reduction of the calculation time can be achieved with less than 2% deviation from the reference values.

The relative distance between points has been increased from 1 (reference case) to 10, 20, 50, 100, 200 and 500 m. The deviation from the average irradiation obtained in the reference case goes from 0.1% up to 2.2%. The deviation from the maximum irradiation obtained in the reference case is instead higher and goes from 1.6% up to 4.8%. The optimal balance between reduction of the number of points to be analyzed and results deviation was found at 100 m relative distance between the points with 0.4% deviation from reference average and 1.6% deviation from maximum reference.

6.3. Estimation of the irradiation and DC yield potential of solar highways in the Netherlands

The results of the skyline profile extraction showed that solar roads have an average SVF of 0.9. Therefore, it can be stated that highways mainly show almost free horizon conditions. It was observed that built-up areas reduce SVF, but that they are not the only relevant factor. Bridges and especially trees aligned along the roadside are a common cause of significant shade. However, it is difficult to express a general statement, since highways in urban areas tend instead to be built far away from buildings - in order to reduce the noise - whereas tree-lined avenues are more common in the countryside.

A map of the irradiation potential of solar highways for the whole Netherlands was generated and it was shown in Section 5.3. The road sections that receive higher annual irradiation are normally elevated road sections or roads that pass through the countryside. On the other hand, low irradiation potentials are mainly caused by surrounding buildings in densely built-up areas (urban areas), trees along the roadside, underpasses or distortion of the LiDAR data, as explained in Section 3.2.2. Solar highways in the Netherlands receives an average irradiation of 882 kWh/m^2/y, 14% less than the maximum irradiation achievable by a 0° tilt mounted module (1026 kWh/m^2/y), and 35% less than the maximum irradiation received by an optimally tilted module (1367 kWh/m^2/y) in South Holland. The three most irradiated highways are A31, A5 and A200 with average annual irradiation of 1002, 999 and 983 KWh/m^2/y, respectively. All three mainly cross the countryside.

To give a more detailed example, the ring road around Amsterdam was considered. The A10 annual average irradiation was found to be 881 kWh/m^2/y, with a maximum peak of 1022 kWh/^{2}/y in the area of Watergraafsmeer, Ringweg Oost. With the use of the potential map, it was possible to identify several optimal locations for a solar road installation on the A10. As an example, the road section South-West to the Tweede Coentunnel receives average irradiation of 940 KWh/m^2/y and presents a larger surface to be covered with solar road modules due to increase of the number of lanes. In addition, an example of a site that does not seem suitable for solar road application was indicated as well. It is located in the East part of the Ringweg Noord, where the A10 crosses the S115. The irradiation reduction is caused both by the presence of a bridge passing over the highway and by trees aligned along the roadside.

A map of the poly c-Si DC yield potential of solar highways for the whole Netherlands was generated as well and can be found in Section 5.4. For poly c-Si modules, solar highways in the Netherlands show an average output of 138 KWh/m^2/y, with peaks of 160 KWh/m^2/y. If mono c-Si is installed, the average increases to 174 KWh/m^2/y, while the use of CIGS would reduce it to 90 KWh/m^2/y (considering the assumed technologies, as described in Appendix E. The top three roads A31, A5 and A200 were found to generate an average between 154 and 157 KWh/m^2/y with poly c-Si, between 192 and 196 KWh/m^2/y with mono c-Si, and between 100 and 105 KWh/m^2/y with CIGS.

In total, covering the entire Dutch highways network with solar road modules would generate 5.2 TWh/y, 6.6 TWh/y, and 3.4 TWh/y if poly c-Si, mono c-Si and CIGS technologies are assumed, respectively. This equals 3-5 % of the national electricity consumption (120 TWh according to the CBS 2018). Assuming that 15% of the electricity consumption goes to street lighting, solar highways solely could power up to 36% of the national demand. This would significantly reduce the consumption of fossil fuels and the CO2 impact in the Dutch energy sector.

6.3.1. Evaluation of traffic shading on irradiation and DC yield potential

Traffic shading has also been analyzed for the case of A12 and A16. It resulted that on average solar road modules are covered by vehicles almost 240 hours per year, with some points reaching a peak of 450 hours. A map of this value was generated for the two case studies of the A16 and A12 and can be found in Section 5.4 and in Appendix D. The reduction of irradiation potential resulted to be on average of 27 kWh/m^2/y, with peaks of 57 kWh/m^2/y. In percentages, irradiation reduction caused by traffic stays around 3% with isolated maximum values up to 6.8%. As a consequence, DC yield potential is reduced on average by 4 kWh/m^2/y in the same locations, with peaks of almost 9 kWh/m^2/y. Per cent reduction of energy output remains below 3% of the annual yield, with some isolated cases where it rises to 7%. According to the results, traffic did not show to drastically decrease the potential of solar highways. Nevertheless, losses caused by traffic shading are comparable with inverter conversion losses (around 5%) and need therefore to be taken into consideration.

In addition, it is interesting to observe which are the situations in which traffic generates the highest losses. In fact, this information might be helpful to decide where to place the solar road. For this purpose, the case of the interchange Knooppunt Lunetten on the A12 and the bridge Van Brienenoordbrug on the A16 were further analyzed. The aim was to give an example of two characteristic road sections in which the shape and function of the road normally increase the traffic and consequently the traffic shading. In general, interchanges are used to deviate the routes of vehicles into different directions and they mainly connect roads of different dimensions and types. At the entrance of an interchange (called ramp), vehicles with lower driving speed are injected into the flow of a high-speed road (a highway for example). This can be a cause of congestion because the flow of cars suddenly increases and the average speed decreases on the point. This is the case at Knooppunt Lunetten, where the line after a ramp shows a traffic coverage time of 402 h/y, with a reduction of the irradiation potential up to 50 kWh/m^2/y (around 5% of the annual irradiation) and consequently DC yield reduction of 8 kWh/m^2/y (almost 6% of the annual generation). Bridges also increase traffic shading, due to the fact that they are the connecting point between two sides of a river or of another crossing highway. To make the construction of a bridge effective, many

roads are directed to few bridges. This increases the flow of cars and consequently the traffic shading. In the analyzed case of Van Brienenoordbrug the traffic coverage time reaches 416 h/y, causing a reduction of the irradiation potential up to 57 $kWh/m^2/y$ (around 6% of the annual irradiation). Consequently, the DC yield decreases by 8 $kWh/m^2/y$ (almost 6% of the annual generation).

7

Recommendations

Referring to the scarce literature and data collection regarding the performance of solar roads, it can be noticed that the energy output provided by test installations are significantly lower than the results obtained with the model presented here. This is due to the fact that the model is still very optimistic in estimating the performance of the modules. The numbers given represent the optimal potential of each location analyzed. However, future development of the model will need to take into account many other relevant aspects. The most important, based on the experience of TNO and Wattway by Colas, seemed to be the delamination of the ASL. Further improvement of the technology will decrease this effect, but an efficiency drop due to surface wear should be accounted for in the model. Studies should be conducted in order to evaluate its actual impact on the performance of the PV modules. Another very important aspect is considered to be soiling and accumulation of dirtiness on the road surface. This also has not been implemented in the model yet and represent therefore another source of discrepancy with real data. In addition, the materials and building elements of solar roads should be further studied to implement a more accurate temperature model.

7.1. Suggestions for the model improvement

For the improvement of the research project here presented, the following recommendations are made.

- In the model presented in this report, solar roads are assumed to have 0° tilt angle. However, this is not exactly the case for roads in reality. For reasons such as drainage purposes but also driving comfort in turns, roads are built with varying inclinations. A study of the average inclination along a road section and the implementation of the obtained value as the tilt angle for the solar road modules could further improve the model output.

- The AoI correction factor presented in this report was for the improvement of 0° tilted modules. To extend the correction to other tilt angles different orientations need to be considered as well.

- In order to obtain single road points, they need to be selected from the whole Hectopunten map. This is a very time-consuming process that would need to be addressed differently in order to reduce the time of extraction of a solar road potential. In addition, the superposition of the Hectopunten map and the LiDAR data does not account for the difference of height between for example two roads that cross each other. The same point that represents the road that passes below will be projected at the top of the road passing above. This will result in a wrong estimation of the potential. In the case of this project, these points were manually removed. However, this process was very time-consuming. The model could be improved by accounting for the difference of height between two following points. The algorithm should detect that two consecutive

points have a height different that overcome a fixed threshold. In this case, the height of the wrong displaced point could be corrected. Figures 7.1a and 7.1b give two examples of cases in which the data needed to be manually removed.

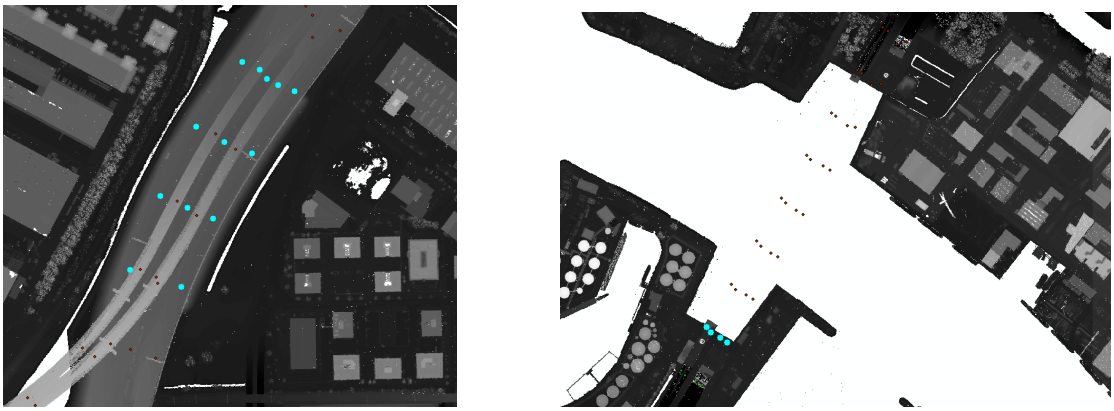

(a) The injecting road and the main road below are at different level (heights). The red points should not be considered together with the points marked in light blue.

(b) Points representing a going in an underpassage below a canal. The points marked in light blue are already in a tunnel and, together with the points represented above water, should not be considered.

Figure 7.1: Examples of manual corrections of the Hectopunten map

- LiDAR data do not show the real shape of objects, but only the one that can actually be detected from above. For modules placed on the ground, this can represent a large error in representing the light that can reach the solar road surface. Figure 7.2 shows that part of the sun path passes below the tree planted along the SolaRoad in Krommenie. However, the skyline extraction methods applied until now in PV system modelling do not account for this area of the sky, as represented by the red skyline profile in the figure. It may be possible to evaluate the impact of this underestimation on the irradiation potential.
- Interpolation is a critical point for solar irradiation. On a regional scale, many studies can be found regarding the evaluation of different interpolation methods. However, when the scale is reduced, like in the case of the research study here presented, the results are too location-dependent to be interpolated with the same methodologies. Therefore, a deeper study of the most suitable interpolation methods for solar road irradiation and DC yield potential should be conducted.
- The traffic shading model provides an estimated DC yield loss due to vehicles shading that does not consider the cells interconnection nor the geometry of the modules. Frequency of hot spots formation in the modules due to traffic jam, together with the consequences in terms of output losses, should be further analyzed.
- The traffic shading model accounts only for the direct shade of a vehicle passing on the cell. It does not account for the shadow that vehicles project on the road surface due to their height. This shadow changes shape and area every moment of the day, depending on the altitude of the sun. This extension of vehicles' shadow on road surface could be introduced in future versions of the model. Additionally, different vehicles dimensions could also be considered. This could be modelled using the direct LiDAR points distributed along the road surface, which could give a resolution of data of around 1 m^2. However, this requires a very large computational power and it is extremely time-consuming. Therefore, this approach is suggested for only small selected areas.
- It is interesting to know if the traffic coverage time could be more quickly correlated to an irradiation reduction on the road surface. Figure 7.3 shows the scatter graphs of the correlation between traffic coverage time and per cent irradiation reduction in

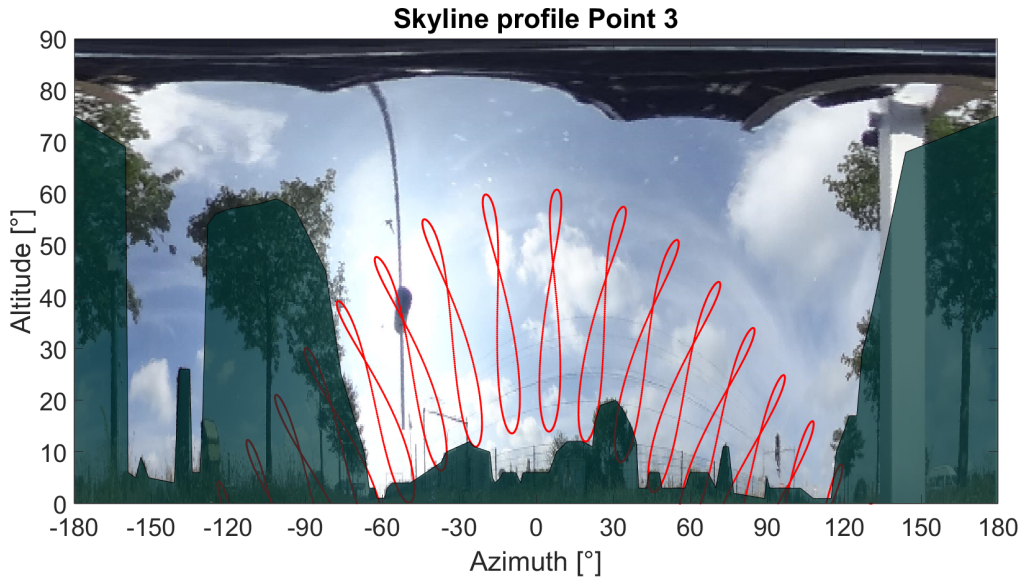

Figure 7.2: Skyline profile of Point 3 (RD coordinates: 112.841, 500.877) along the TNO SolaRoad. The extraction of the skyline profile was obtained with an Horicatcher picture and the software Meteonorm.

the respective points for the A12 and A16. Correlation coefficients of 0.86 and 0.78 are obtained, respectively. This means that the data are strongly correlated and that a linear function can represent the increase of percentage irradiation reduction with the increase of traffic coverage time.

The collection of more data from other roads could bring to a more accurate and solid understanding of this correlation. It would then be possible to provide a quick method to estimate how the traffic can impact on the percentage reduction of irradiation in a location. In fact, only providing flow and speed data is possible to estimate the annual traffic coverage time of a point. Given the slope of the linear regression that correlates the traffic coverage time with the irradiation reduction, the impact of traffic on the solar road potential could be easily estimated.

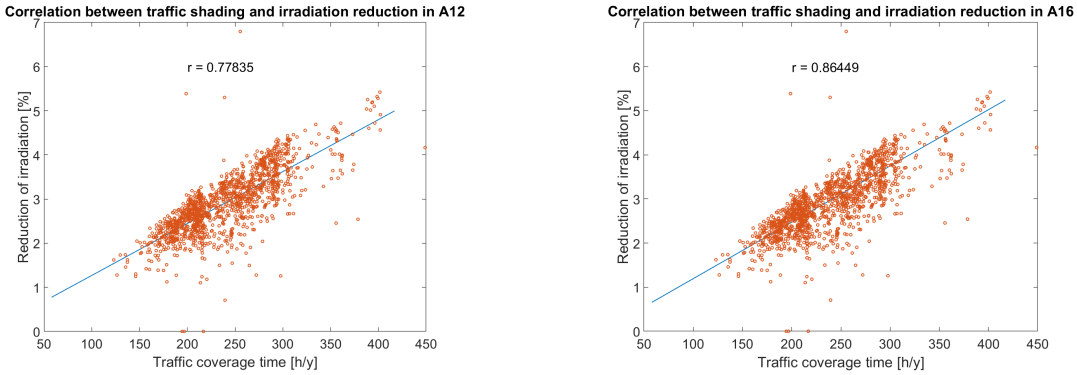

Figure 7.3: Scatter graphs that represent the correlation between the traffic coverage time and the per cent irradiation reduction for A12 (left) and A16 (right).

- Eventually, the suitability of the applied temperature model to represent thermal exchange in the thin glueable technology needs to be critically investigated. From the results, the module temperature does not seem to be sufficiently responsive to ground and ambient temperature when compared with the TNO SolaRoad model. Further research into the materials and building methods should be conducted in order to improve the model inputs.

7.2. Further development of the model with soiling effect

The third major environmental factor that affects power losses in photovoltaic modules is the so-called soiling effect [55]. It is referred to soiling losses when the transmitted light of a module is reduced due to shading or refraction caused by snow, dirt, dust, sand, biological deposit, bird droppings and more, deposited on the array surface. These losses can reduce the system annual yield up to 20 % [44] and increase therefore its LCOE.

In case of solar roads, the soiling effect is expected to have a significant impact on the effective power conversion for three main reasons: (1) the proximity to an intense source of particulate matter (PM) such as cars and other vehicles, (2) the horizontal position that decrease the action of natural cleaning agents like rain, and (3) the roughness of the surface, which increases the capture and adhesion of dirtiness.

In built-up environments, the sources of dust are several: combustion processes, which include emission of pollutants and ash, industrial processes vehicular movements and agricultural activities majorly contribute to suspended particles in the atmosphere [55]. The contribution of some of them is given in Table 7.1.

Table 7.1: Contribution of different sources to outdoor PM concentration [11]

Source	Range of outdoor air [μ g/m^3]
Cooking	2 - 3
Wood burning	1 - 4
Soil dust	1 - 23
Industry, heating	4 - 6
Traffic emission (mostly diesel)	5 - 17
Secondary PM (SO_4^{2-}, NO_3^-, NH_4^+)	11 - 22

These particles are transported by the wind and adhere to the module surface. While transportation mainly depends on the environmental conditions, the adhesion process involves also the module tilt and orientation and its surface characteristics [55].

Module tilt: In case of solar roads, where modules are assumed to have a tilt of 0°, the deposition mechanism of gravitational settling is dominant and result in a high rate of dust deposition [29]. However, the gravitational settling velocity is directly proportional to the squared diameter of the particle. We can, therefore, conclude that for solar roads the deposition rate will be particularly high for larger particles, whereas small particle will tend to adhere to surfaces with higher tilt through the mechanism of dust diffusion [29].

PV technology: The soiling of the module surfaces influence its spectral transmission. Power losses depend, therefore, on the bandgap of the applied PV technology. The experiments conducted in [54] show that for a fixed dust coverage, the soiling losses were 7% higher for a-Si in respect with conventional c-Si modules. Amorphous silicon absorbs light with larger wavelengths, while crystalline silicon cells work for shorter wavelengths. We can, therefore, conclude, that for larger wavelength soiling losses due to spectrum modifications are higher with respect to shorter wavelengths.

Module surface: Module textured surfaces aim to increase the absorbed light, reducing reflection losses. However, dust particles and other sources of soiling are more easily trapped by these surfaces, increasing the soiling ratio of the module. Additionally, the cleaning processes, both artificial and manual, are made less efficient in removing the dust particles from the trap sites. This aspect is important to be considered in the case of solar roads because their surfaces are made rougher than a conventional PV module to recreate the anti-skid conditions of asphalt.

Wind speed: In [29], it is stated that the dust accumulation is a result of the difference between the rate of deposition and rate of removal by the wind. At very low tilt angle, as in the case of solar roads, the limitation of the air boundary layer decreases the removal of dust

carried by the wind. However, the dust removal rate is directly proportional to the diameter of the particles. As stated before, solar roads will more likely be affected by large size dust particles, which however will more easily be removed by the wind as well.

Rainfall: At low tilt, light rainfall (<20 mm) can cause the formation of dust spots and facilitate the cementation of dust particles on the module surface. In an experiment conducted in California by Kimber et al. in 2006, it has been observed that a minimum of 20 mm of rainfall is required to effectively clean optimally tilted PV modules [15].

Relative humidity and dew frequency: Humid conditions and dew formation increases dust adhesion as wet surfaces attract more dust particles [29].

In [44], two types of soil shading are recognized: soft shading and hard shading. Soft shading refers to the uniform accumulation of light dust or fine pollution on the surface. This causes an overall reduction of the short circuit current. Hard shading takes place instead when a solid such as local accumulated dust shades the module, creating the condition of partial shading. In this situation, if bypass diodes are applied to maintain the current constant, a drop of voltage occurs.

All this considered, in order to account for soling losses in the solar road model here presented, further studies regarding soiling accumulation in order to define the angular soiling coefficient a_r for solar roads need to be conducted. Based on the literature review and the personal observation of the pilot project of TNO SolaRoad in Krommenie, operating since 2014, it is firmly believed that soiling losses account for a high reduction of solar roads generation potential. Therefore, it is therefore highly recommended to focus on modelling the soiling losses for further research on the topic of solar road potential estimation.

In addition to that, pollution and haze should also be taken into consideration. The introduction in the model of spectral dependence irradiance would then be needed.

7.3. Solar road feasibility studies

Now that the potential of solar roads can be simulated in an effective, quick and accurate way, it is important to address a different aspect of the technology in order to assess the feasibility of a solar road installation. In fact, as already mentioned in Section 4.1, not only the irradiation and DC yield potential are determinant when evaluating solar road projects, but also the following aspects should be further studied and considered:

- **Dynamic shading:** the effect of dynamic shading on the efficiency of the maximum power point tracker should be further researched. In [73], Y. Haoyuan et al. developed a MATLAB-based model that accounts for the dynamic characteristics of a photovoltaic (PV) module under a dynamic shadow with different degrees of shading. They observed that shadows with different trajectories (such as initial point, speed and path) could differently change the power-voltage curve of the investigated module.

- **Noise generation:** if solar road modules substitute the porous asphalt of conventional road surfaces, a higher vehicle noise generation should be accounted for. This can restrict the number of sites available for solar roads installation, especially in urban areas;

- **Grid connection:** the possibility to connect solar roads to the grid should be verified for each location. Additionally, the placement of inverters along the solar road installation should be taken into account, together with all the consequences of costs, social acceptance, space availability, etc.;

- **Road surface deterioration:** from the solar roads pilot projects that are running around the world, it has been observed that the ASL tends to delaminate with time and usage. This causes a decrease of conversion efficiency that needs to be taken into account when modelling solar roads output. Further studies and data collection are still needed. The evaluation of the impact on road safety needs to be researched as well;

- **Costs:** solar road applications are still significantly more expensive than conventional modules. An accurate assessment of investment capital, maintenance costs and payback time needs to be addressed in order to correctly evaluate solar road projects. In addition, a study of the energy payback time of the technology should be conducted: if a solar road requires more energy to be produced than the one that it generates during its lifetime, is it still reasonable to build a solar road system?

Bibliography

[1] URL http://desktop.arcgis.com/en/arcmap/10.3/manage-data/las-dataset/what-is-lidar-data-.htm.

[2] A13 busiest national motorway in the netherlands. Technical report, Centraal Bureau voor de Statistiek, . URL https://web.archive.org/web/20170123212801/https://www.cbs.nl/NR/rdonlyres/25CE3592-A756-42B7-BABF-C3E4C4E9375B/0/a13busiestnationalmotorwayinthenetherlands.pdf.

[3] Trends in the netherlands. Technical report, Centraal Bureau voor de Statistiek, .

[4] Energy consumption down in 2018. Technical report, Centraal Bureau voor de Statistiek, . URL https://www.cbs.nl/en-gb/news/2019/16/energy-consumption-down-in-2018.

[5] Urban mobility lab demonstrator. URL https://dittlab.tudelft.nl/index.php/applications-demos.

[6] Inductive loops. URL http://support.diamondtraffic.com/knowledgemanager/questions/23/Inductive+Loop+Guide.

[7] Net electricity generation, eu-28, 1990-2017. Technical report, European Commission. URL https://ec.europa.eu/eurostat/statistics-explained/index.php/Electricity_production,_consumption_and_market_overview.

[8] Published solar data. Technical report, . URL https://www.homerenergy.com/products/pro/docs/latest/published_solar_data.html.

[9] Light measurement handbook. basic principles. URL http://www.dfisica.ubi.pt/~hgil/Fotometria/HandBook/ch06.html.

[10] Energy report. transition to sustainable energy. Technical report, Ministry of Economic Affairs.

[11] Guidelines for concentration and exposure-response measurement of fine particulate matter for for use in epidemiological studies. URL https://apps.who.int/iris/bitstream/handle/10665/67338/a76621.pdf?sequence=1&isAllowed=y.

[12] URL https://www.pdok.nl.

[13] A. Calcabrini et al. A simplified skyline-based method for estimating the annual solar energy potential in urban environments. *Nature Energy*, ??:??, 2019. doi: https://doi.org/10.1038/s41560-018-0318-6.

[14] A. Carr and T. Pryor. A comparison of the performance of different pv module types in temperate climates. *Solar Energy*, (76):285–294, 2004.

[15] A. Kimber et al. The effect of soiling on large grid-connected photovoltaic systems in california and the southwest region of the united states. In *2006 IEEE 4th World Conference on Photovoltaic Energy Conference*, volume 2, pages 2391–2395, May 2006. doi: 10.1109/WCPEC.2006.279690.

[16] A. S. Dezfooli et al. Solar pavement: A new emerging technology. *Solar Energy*, 149: 272–284, 2017.

[17] A. Sabán. El primer experimento con carretera solar en francia ha sido un fracaso: pavimento deterioriorado, ruidoso y poco eficiente. URL https://www.xataka.com/energia/primer-experimento-carretera-solar-francia-ha-sido-fracaso-pavimento-\deterioriorado-ruidoso-poco-eficiente#comments.

[18] A. Saifuddin et al. Energy harvesting from pavements and roadways: A comprehensive review of technologies, materials, and challenges. *International Journal of Energy Research*, 55, 2019.

[19] A. Shekhar et al. Harvesting roadway solar energy-performance of the installed infrastructure integrated pb bike path. *IEEE Journal of Photovoltaics*, 8:1066–1073, 2018. doi: 10.1109/JPHOTOV.2018.2820998.

[20] A. Smets et al. *The physics and engineering of photovoltaic conversion and systems*. UIT Cambridge, Cambridge, England, 2016.

[21] C. A. Gueymard. Turbidity determination from broadband irradiance measurements. a detailed multicoefficient approach. *Journal of Applied Meteorology*, 37, 1998. doi: https://doi.org/10.1175/1520-0450(1998)037<0414:TDFBIM>2.0.CO;2.

[22] C. A. Gueymard. Direct solar transmittance and irradiance predictions with broadband models. part i: detailed theoretical performance assessment. *Solar Energy*, 74:355–379, 2003. doi: https://doi.org/10.1016/S0038-092X(03)00195-6.

[23] C. Efthymiou et al. Development and testing of photovoltaic pavement for heat island mitigation. *Solar Energy*, 130:140–160, 2016. doi: http://dx.doi.org/10.1016/j.solener.2016.01.054.

[24] D. L. King et al. Performance model for grid-connected photovoltaic inverters. *Tech. Rep. SAND2007-5036 (Sandia National Laboratories)*, 2007.

[25] D. T. Reindl et al. Evaluation of hourly tilted surface radiation models. *Solar Energy*, 1 (45):9–17, 1990.

[26] Paul Denholm and Robert M. Margolis.

[27] DuPont™. Dupont™ tedlar® polyvinyl fluoride (pvf) films. URL http://www.dupont.com/products-and-services/membranes-films/pvf-films/brands/tedlar-pvf-films/uses-and-applications/tedlar-solar-energy-applications.html. Last accessed 16th January 2019.

[28] E. van Gastel and M. de Jonge Baas. Bam infra stopt proef met zonnewegdek: 'potentie aanwezig, maar verdere ontwikkeling nodig'. URL https://solarmagazine.nl/nieuws-zonne-energie/i18509/bam-infra-stopt-proef-met-zonnewegdek-potentie-aanwezig-maar-\verdere-ontwikkeling-nodig.

[29] A. Sayyah et al. Energy yield loss caused by dust deposition on photovoltaic panels. *Solar Energy*, 107:576–604, 2014. doi: 10.1016/j.solener.2014.05.030.

[30] F. Lindberg et al. Solar energy on building envelopes-3d modelling in a 2d environment. *Solar Energy*, 115:369–378, 2015. doi: http://dx.doi.org/10.1016/j.solener.2015.03.001.

[31] Gerry Julian Faturrochman. Design optimization of bifacial photovoltaic noise barriers usign a high granularity energy yield modelling approach, 2017.

[32] Tomotoshi Funabashi. A gis approach for estimating optimal sites for grid-connected photovoltaic (pv) cells in nebraska, 2011.

[33] Bill Holdsworth. Renewable energy roads. *Renewable Energy Focus*, pages 58–60, 2003.

[34] J. A. Ruiz-Arias and C. Gueymard. Solar resource for high-concentrator photovoltaic applications. In *Green Energy and Technology*, page 261–302. Munich, Germany, 2015.

[35] J.E. Hays and J.A. Davies. Calculations of the solar radiation incident on an inclined surface. *Proc. of First Canadian Solar Radiation Data Workshop*, 1980.

[36] G. T. Johnson and I. D. Watson. The determination of view-factors in urban canyons. *Journal of Climate and Applied Meteorology*, 23:329–335, 1984.

[37] Lee Kang-Won Wayne and J. Correia Andrew. A pilot study for investigation of novel methods to harvest solar energy from asphalt pavements, March 2010. URL http://www.doc88.com/p-5099938367770.html. Last accessed 14th January 2019.

[38] Kasten, Fritz and Young, Andrew T. Revised optical air mass tables and approximation formula. *Applied Optics*, 28(22):4735–4738, 1989.

[39] F. Lindberg and C. S. B. Grimmond. Continuous sky view factor maps from high resolution urban digital elevation models. *Climate Research*, 42:177–183, 2010. doi: 10.3354/cr00882.

[40] F. Lindberg and C. S. B. Grimmond. The influence of vegetation and building morphology on shadow patterns and mean radiant temperatures in urban areas: model development and evaluation. *Theor. Appl. Climatol.*, 105:311–323, 2011. doi: 10.1007/s00704-010-0382-8.

[41] John W Lund. Pavement snow melting, Jan 2005.

[42] M. K. Fuentes. A simplified thermal model for flat-plate photovoltaic arrays.

[43] M. Keijzer. *A multi-surface reflected irradiance model for pyranometer corrections and PV yield calculations in complex urban geometries*. Master of science, TU Delft, Delft, The Netherlands, 2019.

[44] M. R. Maghami et al. Power loss due to soiling on solar panel: A review. *Renewable and Sustainable Energy Reviews*, (59):1307–1316, 2016. URL http://dx.doi.org/10.1016/j.rser.2016.01.044.

[45] M. S. Wu et al. Economic feasibility of solar-powered led roadway lighting. *Renewable Energy*, 34:1934–1938, 2009.

[46] M. Vázquez and A. Hanslmeier. *Ultraviolet Radiation in the Solar System*. Springer-Verlag, 2006.

[47] M. Zaaijer and A. Viré. Introduction to wind turbines: physics and technology, November 2017.

[48] Meindel, Aden B. and Meinel, Marjorie P. *Applied solar energy. An introduction*. Addison-Wesley publishing company, University of Arizona, USA, 1979.

[49] N. E. Ligterink. On-road determination of dutch driving behavior for vehicles emissions. URL http://www.emissieregistratie.nl/erpubliek/documenten/Lucht%20(Air)/Verkeer%20en%20Vervoer%20(Transport)/Wegverkeer/TNO%20(2016)%20On-road%20determination%20of%20Dutch%20driving.pdf.

[50] Sara Najem. Solar potential scaling and the urban road network topology. *Physical Review*, 95, 2017. doi: 10.1103/PhysRevE.95.012323.

[51] Thomas Nordmann and Luzi Clavadetscher. Pv on noise barriers. *Journal of Progress in photovoltaics: research and applications*, 12:485–495, 2004. doi: 10.1002/pip.566.

[52] Andrew Northmore. Innovative pavement design: Are solar roads feasible?, 2012.

[53] P. Bellucci at al. Assessment of the photovoltaic potential on noise barriers along national roads in italy. In *3rd World Conference on Photovoltaic Energy Conversion*. Osokn, Japan, 2003.

[54] P. Nepal. Accurate soiling ratio determination with incident angle modifier for pv modules. *IEEE Journal of Photovoltaics*, 2018.

[55] P. Nepal. *Effect of Soiling on the PV Panel kWh Output*. Master, TU Delft, Delft, The Netherlands, March 2018.

[56] Rebecca Pool. Sunshine highways. *Engineering & Technology*, pages 54–57, 2011.

[57] Pultarova, Tereza. Welcome to the world's first solar road. *Engineering & Technology*, page 10, 2017.

[58] PV Performance-Modeling Collaborative. Modeling steps. URL https://pvpmc.sandia.gov/modeling-steps/. Last accessed 25th January 2019.

[59] R. Perez et al. Modeling daylight availability and irradiance components from direct and global irradiance. *Solar Energy*, 5(44):271–289, 1990.

[60] Carlo Ratti and Paul Richens. Raster analysis of urban form. *Climate Research*, 31: 297–309, 2004. doi: 10.1068/b2665.

[61] Darren Robinson. Urban morphology and indicators of radiation availability. *Solar Energy*, 80:1643–1648, 2006. doi: https://doi.org/10.1016/j.solener.2006.01.007.

[62] Solar Roadways. URL http://www.solarroadways.com. Last accessed 20th December 2018.

[63] SolaRoad. Pilot projects. URL https://www.solaroad.nl/portfolio/.

[64] D. G. Stey. The calculation of view factors from fisheye□lens photographs: Research note. *Atmosphere-Ocean*, 3:254–258, 1980. doi: https://doi.org/10.1080/07055900.1980.9649091.

[65] TNO. Solar energy from roads, 2010.

[66] TNO. Solaroad, 2011.

[67] Martin Treiber and Dirk Helbing. An adaptive smoothing method for traffic state identification from incomplete information. 32:343–360, 2002. doi: 10.1007/978-3-662-07969-0{\textunderscore}33.

[68] V. K. Kumaravel. *Energy yield modelling and validation of SolaRoad*. Master of science, TU Delft, Delft, The Netherlands, 2016.

[69] V. Prasanth et al. Green energy based inductive self-healing highways of the future. 2016.

[70] Wattway. URL http://www.wattwaybycolas.com/en/.

[71] Wikipedia. 'motorways in the netherlands' - wikipedia, the free encyclopedy, 2019. URL https://en.wikipedia.org/wiki/List_of_motorways_in_the_Netherlands. [Last visit: 6th August 2019].

[72] Y. A. Cengel and A. J. Ghajar. *Heat and mass transfer: Fundamentals & applications*. McGraw-HIll, New York, NY, 4 edition, 2011. ISBN 978-0-07-339812-9.

[73] Y. Haoyuan et al. Dynamic modeling of partial shading on photovoltaic arrays. *IEEE Journal of Photovoltaics*, 2015. URL https://www.researchgate.net/publication/283356703.

[74] Z. Rajab et al. Economic feasibility of solar powered street lighting system in libya. In *Word Sense Disambiguation: Algorithms and Applications*. IEEE, Benghazi, Libya, 2017.

A

Actuele Hoogtebestand Nederland (AHN3)

Figure A.1 depicts in which year each region of the Netherlands was provided with full LiDAR data AHN3. As it can be observed, at the time in which this research project has been conducted (2019), the Nord-East region of Groeningen did not have available LiDAR data yet and it was therefore impossible to complete the solar road map for that area.

Figure A.1: Years in which LiDAR measurements have been conducted for each region of the Netherlands (source: Esri Nederland, Community Map Contributors)

B

Sensitivity analysis

B.1. Azimuth step angle

Table B.1: Results of the sensitivity analysis for azimuth step angle increase

Step angle [°]	1	2	5	10	20
Calculations [-]	32400	16200	6480	3240	1620
Mean deviation	0	0.2%	1.29%	3.7%	7.6%
Std	0	2.1%	4.0%	4.5%	8.1%

B.2. Points density

Table B.2: Results of the sensitivity analysis for points density on road length

Relative distance	**N_{points}**	**Mean(Irr)**	**Max(Irr)**	**Min(Irr)**	**Dev from mean**	**Dev from max**
[m]	**[-]**	**[kW/m^2]**	**[kW/m^2]**	**[kW/m^2]**	**[%]**	**[%]**
1	14666	782	1003	0	-	-
10	1466	783	987	5	-0.13	1.6
20	733	784	987	13	-0.26	1.6
50	293	784	987	5	-0.26	1.6
100	147	785	987	13	-0.38	1.6
200	73	793	954	13	-1.41	4.89
500	28	769	955	13	1.66	4.79
1000	14	799	955	13	-2.17	4.79

Table B.3: Results of the sensitivity analysis for points density on road width

Relative distance	**N_{points}**	**Mean(Irr)**	**Max(Irr)**	**Min(Irr)**	**Dev from mean**	**Dev from max**
[m]	**[-]**	**[kW/m^2]**	**[kW/m^2]**	**[kW/m^2]**	**[%]**	**[%]**
5	15	742	925	406	-	-
15	4	782	878	649	-5.39	5.08
20	2	764	878	649	-2.96	5.08

B.3. AM correction factor

Table B.4: Improvement of the coefficient of determination in the model, after applying the AM correction factor

R^2 - Antofagasta [°]	0	20	45	70	90
Original model	0.9821	0.9764	0.978	0.9871	0.992
AM correction	0.9920	0.9809	0.9773	0.9855	0.9895

R^2 - Delft [°]	0	20	45	70	90
Original model	0.9712	0.975	0.982	0.9872	0.9882
AM correction	0.9887	0.9846	0.986	0.9889	0.9889

R^2 - Reykjavik [°]	0	20	45	70	90
Original model	0.9704	0.9774	0.9817	0.9845	0.9853
AM correction	0.9935	0.9873	0.9875	0.9885	0.9877

R^2 - Bata [°]	0	20	45	70	90
Original model	0.9839	0.9836	0.983	0.9904	0.9928
AM correction	0.9938	0.989	0.9833	0.9902	0.9922

C

Irradiation and DC yield maps

C.1. Irradiation potential of solar highways in the Netherlands

(a) (b)

Figure C.1: Jenks Natural Breaks classification for (a) irradiation and (b) DC yield potential expressed in kWh/m^2/y.

Table C.1: Statistics of SVF along highways in the Netherlands

Road	Number of points	Avg SVF	Max SVF	Min SVF	StD
A1	2678	0.90	0.99	0.00	0.12
A10	891	0.88	0.99	0.06	0.13
A12	3255	0.89	0.99	0.00	0.12
A13	357	0.89	0.99	0.09	0.11
A15	3608	0.91	0.99	0.01	0.13
A16	2960	0.88	0.99	0.02	0.16
A17	655	0.91	0.99	0.02	0.14
A18	449	0.91	0.99	0.25	0.10
A2	6153	0.89	0.99	0.00	0.14
A20	891	0.86	0.99	0.07	0.14
A200	94	0.95	0.99	0.71	0.04
A22	144	0.81	0.99	0.05	0.17
A27	2388	0.90	0.99	0.02	0.12
A28	3503	0.90	0.99	0.01	0.12
A29	661	0.91	0.99	0.02	0.14
A30	349	0.92	0.99	0.01	0.09
A31	384	0.98	0.99	0.04	0.06
A32	1340	0.96	0.99	0.27	0.06
A38	34	0.88	0.99	0.67	0.08
A4	2808	0.92	0.99	0.07	0.12
A44	414	0.89	0.99	0.18	0.11
A5	378	0.97	0.99	0.28	0.06
A50	3026	0.90	0.99	0.00	0.14
A58	2876	0.91	0.99	0.00	0.14
A59	2089	0.92	0.99	0.00	0.11
A6	2166	0.94	0.99	0.09	0.09
A65	397	0.78	0.99	0.00	0.18
A67	1519	0.87	0.99	0.00	0.16
A7	3439	0.94	0.99	0.02	0.10
A73	2681	0.93	0.99	0.00	0.11
A74	28	0.92	0.99	0.62	0.08
A76	592	0.89	0.99	0.20	0.12
A77	202	0.93	0.99	0.01	0.10
A79	350	0.86	0.99	0.24	0.12
A8	200	0.91	0.99	0.06	0.12
A9	1058	0.92	0.99	0.04	0.11

Table C.2: Statistics of irradiation potential of solar highways in the Netherlands

Road	Number of points	Average Irr [kWh/y/m^2]	Max Irr [kWh/y/m^2]	Min Irr [kWh/y/m^2]	StD [kWh/y/m^2]
A1	2678	896.67	1023.39	0.34	137.32
A10	891	881.29	1022.52	27.17	161.91
A12	3255	794.54	1004.42	2	151
A13	357	773	979.03	38.39	140.51
A15	3608	835.67	1015.26	3.83	160.65
A16	2960	804.84	1014.77	6.3	183.78
A17	655	830.53	1000.18	7.13	164.96
A18	449	885.7	980.5	191.97	114.79
A2	6153	809.87	1009.89	0.57	162.51
A20	891	763.16	997.59	38.22	172.74
A200	94	982.68	1020.71	549.56	57.31
A22	144	820.04	1015.83	22.06	191.07
A27	2388	916.72	1025.73	7.34	146.74
A28	3503	774.14	970.06	3.39	148.87
A29	661	834.65	1016.48	8.25	176.3
A30	349	898.09	980.97	4.61	101.31
A31	384	1002.19	1025.62	14.45	71.72
A32	1340	941.19	981.26	115.55	74.9
A38	34	875.45	1012.13	523.72	114.74
A4	2808	856.26	1020.27	29.99	156.79
A44	414	916.64	1023.2	260.73	122
A5	378	999.05	1023.81	116.91	64.77
A50	3026	899.91	1025.58	1.25	162.92
A58	2876	938.38	1025.57	0.99	153.61
A59	2089	932.07	1025.73	1.33	135.07
A6	2166	932.29	1025.76	38.82	103.49
A65	397	775.61	1021.93	1.74	215.21
A67	1519	889.72	1025.6	0.43	185.84
A7	3439	850.2	978.94	8.08	135.5
A73	2681	946.61	1025.9	0.66	125
A74	28	953.17	1021.58	782.53	53.62
A76	592	904.1	1024.18	109.18	142.99
A77	202	957.04	1024.24	2.59	118.99
A79	350	887.88	1024.62	118.84	142.87
A8	200	933.27	1022.21	43.94	137.13
A9	1058	938.1	1025.29	19.53	132.49

C.2. DC yield potential of solar highways in the Netherlands

Table C.3: TNO SolaRoad DC yield coefficients for South-West Netherlands

PV Technology	$\mathbf{d_1}$	$\mathbf{d_2}$	$\mathbf{d_3}$	$\mathbf{d_4}$	$\mathbf{d_5}$	**Sum**
0° Tilt	**[kW/m^2]**	**[kW/m^2]**	**[kW/m^2]**	**[kW/m^2]**	**[kW/m^2]**	**[kW/m^2]**
mono c-Si	105	24	-13	77	0	193
poly c-Si	83	21	-11	61	0	154
CIGS	55	15	-8	40	0	102

Table C.4: Statistics of DC yield potential of solar highways in the Netherlands with mono c-Si

Road	Avg DC yield [kWh/m^2/y]	Max DC yield [kWh/m^2/y]	Min DC yield [kWh/m^2/y]	StD [kWh/m^2/y]	Road length [km]	Tot DC yield [MWh/y]
A1	176.7	200.5	0.1	27.0	157.0	416,222.7
A10	172.6	200.3	5.2	31.9	32.0	82,857.6
A12	155.4	196.8	0.4	29.8	137.0	319,244.3
A13	151.1	191.8	7.4	27.7	17.0	38,522.9
A15	163.5	198.9	0.7	31.6	204.0	500,248.8
A16	155.1	197.6	1.2	35.7	58.0	134,928.3
A17	162.5	195.9	1.4	32.5	39.0	95,039.1
A18	175.1	193.7	37.8	22.7	20.0	52,530.0
A2	158.4	197.8	0.1	32.0	212.0	503,648.4
A20	149.2	195.4	7.4	34.0	39.0	87,264.5
A200	192.6	200.0	107.0	11.4	1.0	2,888.3
A22	160.6	199.0	4.2	37.5	8.0	19,276.8
A27	179.6	201.0	1.4	28.9	109.0	293,613.3
A28	153.0	191.7	0.7	29.5	187.0	429,052.8
A29	163.3	199.1	1.6	34.7	13.0	31,839.6
A30	177.5	193.8	0.9	20.0	18.0	47,935.8
A31	196.4	200.9	2.8	14.1	65.0	191,451.0
A32	186.0	193.9	22.5	14.8	41.0	114,390.0
A38	171.5	198.3	102.0	22.6	1.5	3,858.1
A4	187.9	199.9	5.8	30.8	125.0	352,331.3
A44	179.6	200.5	51.0	24.0	28.0	75,432.0
A5	195.7	200.6	22.5	12.7	14.0	41,105.4
A50	176.9	200.9	0.2	31.9	100.0	265,410.0
A58	183.9	200.9	0.2	30.2	140.0	386,085.0
A59	182.6	201.0	0.3	26.6	75.0	205,413.8
A6	183.7	201.0	7.5	20.2	102.0	281,076.3
A65	151.9	200.2	0.3	42.3	22.0	50,120.4
A67	174.3	200.9	0.1	36.5	78.0	203,919.3
A7	168.0	193.4	1.6	26.8	240.0	604,836.0
A73	185.5	201.0	0.1	24.6	114.0	317,119.5
A74	186.8	200.1	153.3	10.5	2.0	5,603.7
A76	177.1	200.7	21.1	28.1	27.0	71,733.6
A77	187.5	200.7	0.5	23.4	10.0	28,126.5
A79	174.0	200.7	22.9	28.1	18.0	46,969.2
A8	182.8	200.3	8.5	27.0	10.0	27,426.0
A9	183.8	200.9	3.8	26.0	96.0	264,643.2

Table C.5: Statistics of DC yield potential of solar highways in the Netherlands with poly c-Si

Road	Avg DC yield [kWh/m^2/y]	Max DC yield [kWh/m^2/y]	Min DC yield [kWh/m^2/y]	StD [kWh/m^2/y]	Road length [km]	Tot DC yield [MWh/y]
A1	140.1	160.6	0.1	21.5	157.0	329,982.6
A10	138.3	160.5	4.2	25.5	32.0	66,403.2
A12	124.5	157.6	0.3	23.8	137.0	255,929.7
A13	121.1	153.6	5.9	22.2	17.0	30,885.6
A15	131.0	159.3	0.6	25.3	204.0	400,951.8
A16	124.3	158.3	1.0	28.6	58.0	108,158.4
A17	130.2	157.0	1.1	26.0	39.0	76,172.9
A18	138.1	152.8	29.7	17.9	20.0	41,430.0
A2	127.0	158.5	0.1	25.6	212.0	403,732.8
A20	119.6	156.5	5.9	27.3	39.0	69,960.2
A200	154.3	160.2	85.9	9.0	1.0	2,313.9
A22	128.8	159.4	3.4	30.0	8.0	15,452.4
A27	143.9	161.0	1.1	23.1	109.0	235292.9
A28	120.6	151.2	0.5	23.3	187.0	338,198.9
A29	130.9	159.5	1.3	27.8	13.0	25,519.7
A30	140.0	152.8	0.7	145.8	18.0	37,808.1
A31	157.3	160.9	2.2	11.3	65.0	153,367.5
A32	146.7	152.9	17.7	11.7	41.0	90,220.5
A38	137.4	158.9	81.8	18.1	1.5	3,092.2
A4	134.6	160.1	4.6	24.7	125.0	252,318.8
A44	143.9	160.6	41.1	19.2	28.0	60,446.4
A5	156.8	160.7	17.9	10.2	14.0	32,928.0
A50	140.9	160.9	0.2	25.6	100.0	211,335.0
A58	147.3	160.9	0.2	24.1	140.0	309,351.0
A59	146.3	161.0	0.2	21.3	75.0	164,598.8
A6	145.7	161.0	6.0	16.3	102.0	222,905.7
A65	121.8	160.4	0.3	33.9	22.0	40,180.8
A67	139.7	160.9	0.1	29.2	78.0	163,413.9
A7	132.5	152.5	1.2	21.2	240.0	476,892.0
A73	148.6	161.0	0.1	19.6	114.0	254,088.9
A74	149.7	160.3	122.9	8.3	2.0	4,490.1
A76	141.9	160.7	16.9	22.5	27.0	57,485.7
A77	150.2	160.7	0.4	18.7	10.0	22,534.5
A79	139.4	160.8	18.3	22.5	18.0	37,643.4
A8	146.5	160.4	6.8	21.6	10.0	21,976.5
A9	147.3	160.9	3.0	20.8	96.0	212,054.4

Table C.6: Statistics of DC yield potential of solar highways in the Netherlands with CIGS

Road	Avg DC yield [kWh/m^2/y]	Max DC yield [kWh/m^2/y]	Min DC yield [kWh/m^2/y]	StD [kWh/m^2/y]	Road length [km]	Tot DC yield [MWh/y]
A1	91.5	104.7	0.0	14.1	157.0	215,529.6
A10	90.2	104.7	2.7	16.6	32.0	43,310.4
A12	81.2	102.8	0.2	15.5	137.0	166,907.1
A13	79.0	100.2	3.8	14.5	17.0	20,142.5
A15	85.5	103.9	0.4	16.5	204.0	261,507.6
A16	81.1	103.3	0.6	18.6	58.0	70,539.6
A17	84.9	102.4	0.7	17.0	39.0	49,678.2
A18	90.3	99.9	19.4	11.7	20.0	27,078.0
A2	82.8	103.4	0.1	16.7	212.0	263,304.0
A20	78.0	102.1	3.9	17.8	39.0	45,624.2
A200	100.6	104.5	56.0	5.9	1.0	1,509.2
A22	84.0	104.0	2.2	19.6	8.0	10,080.0
A27	93.9	105.0	0.7	15.1	109.0	153,477.5
A28	78.9	98.8	0.3	15.2	187.0	221,258.4
A29	85.4	104.0	0.8	18.1	13.0	16,643.3
A30	91.5	99.9	0.5	10.3	18.0	24,710.4
A31	102.6	105.0	1.4	7.3	65.0	100,025.3
A32	95.9	99.9	11.7	7.6	41.0	58,966.2
A38	89.6	103.6	53.4	11.8	1.5	2,016.9
A4	87.8	104.4	3.0	16.1	125.0	164,568.8
A44	93.9	104.7	26.8	12.5	28.0	39,425.4
A5	102.3	104.8	11.7	6.6	14.0	21,474.6
A50	92.0	105.0	0.1	16.7	100.0	137,955.0
A58	86.1	105.0	0.1	15.8	140.0	180,768.0
A59	95.4	105.0	0.1	13.9	75.0	107,347.5
A6	95.2	105.0	3.9	10.6	102.0	145,579.5
A65	79.4	104.6	0.2	22.1	22.0	26,208.6
A67	91.1	105.0	0.0	19.1	78.0	106,587.0
A7	86.6	99.7	0.8	13.8	240.0	311,868.0
A73	96.9	105.0	0.1	12.8	114.0	165,733.2
A74	97.6	104.6	80.2	5.5	2.0	2,928.6
A76	92.6	104.8	11.0	14.7	27.0	37,494.9
A77	98.0	104.8	0.3	12.2	10.0	14,698.5
A79	90.9	104.9	11.9	14.7	18.0	24,551.1
A8	95.6	104.6	4.5	14.1	10.0	14,332.5
A9	96.0	104.9	2.0	13.5	96.0	138,297.6

D

Traffic shading model output

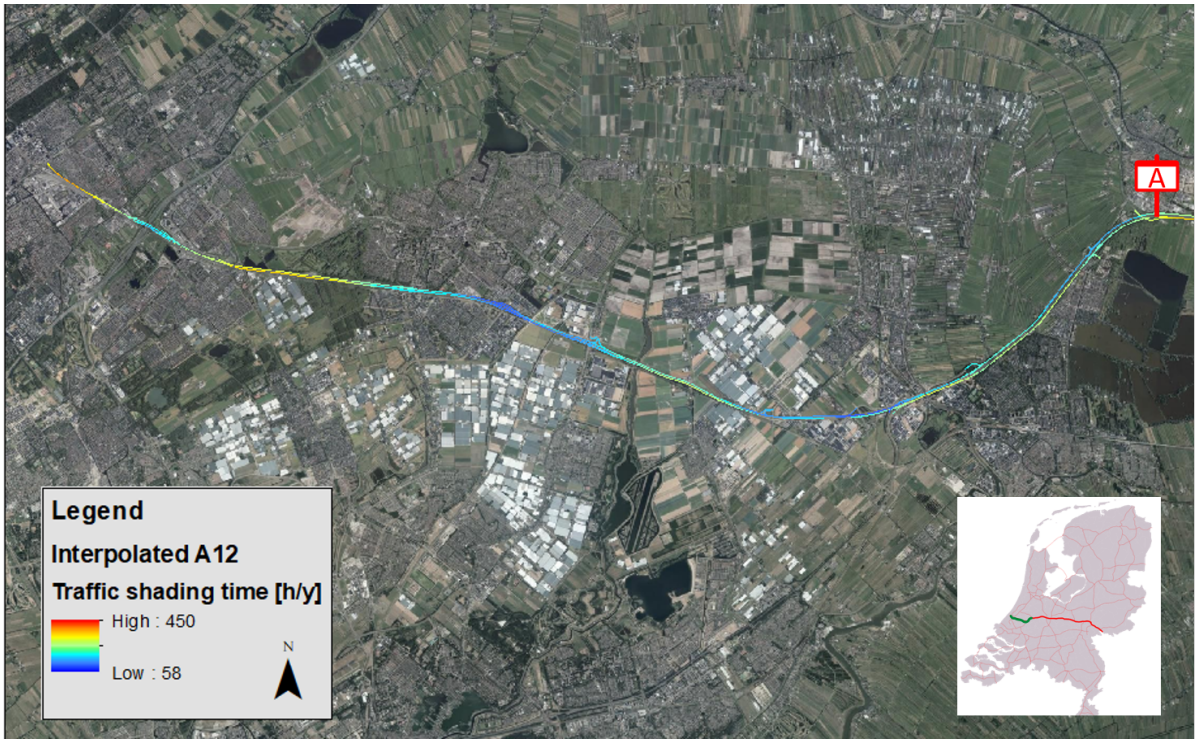

Figure D.1: Traffic coverage time map of A12 - Section A

Figure D.2: Traffic coverage time map of A12 - Section A-B

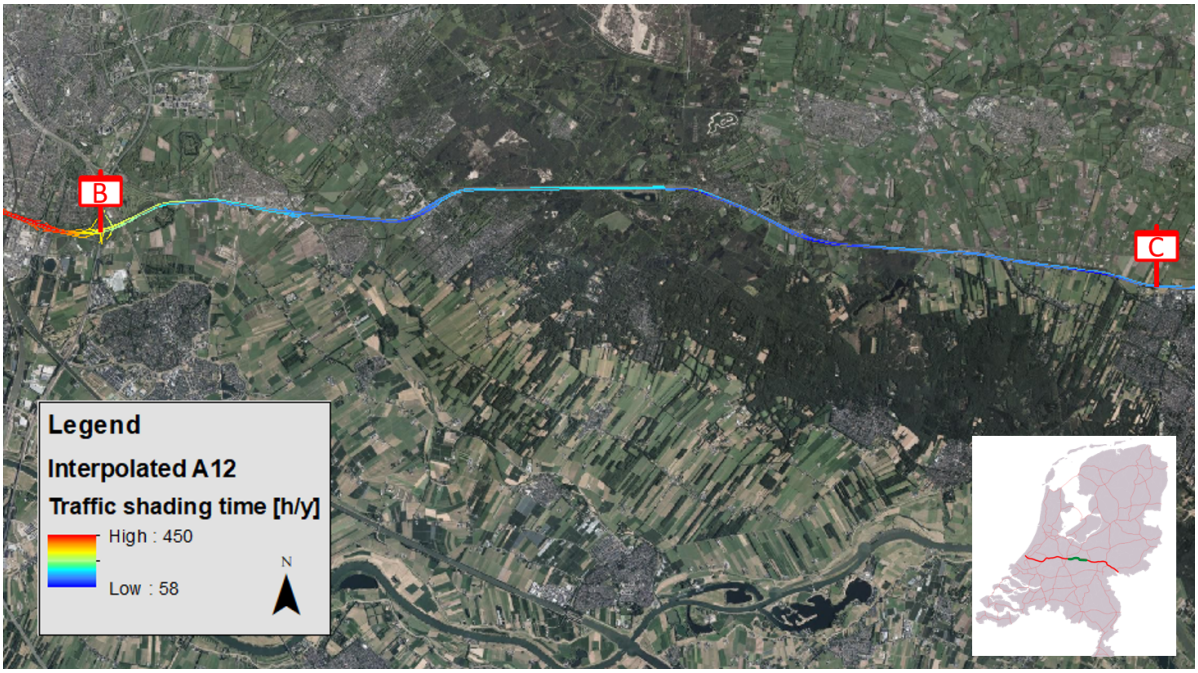

Figure D.3: Traffic coverage time map of A12 - Section B-C

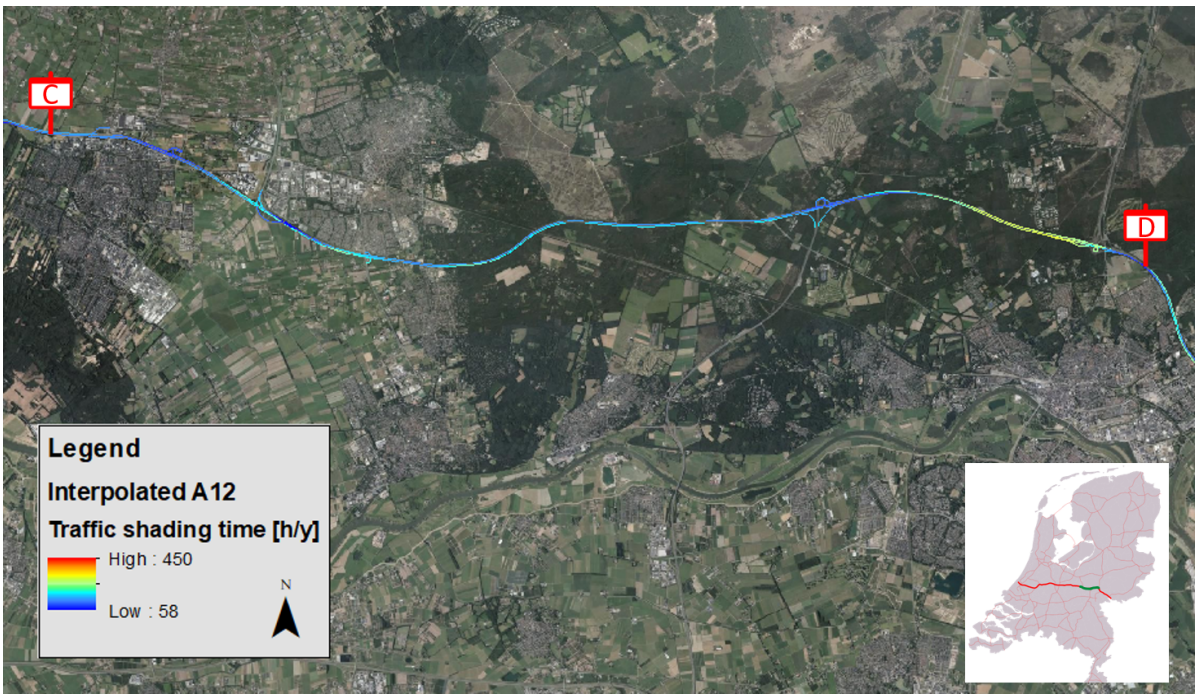

Figure D.4: Traffic coverage time map of A12 - Section C-D

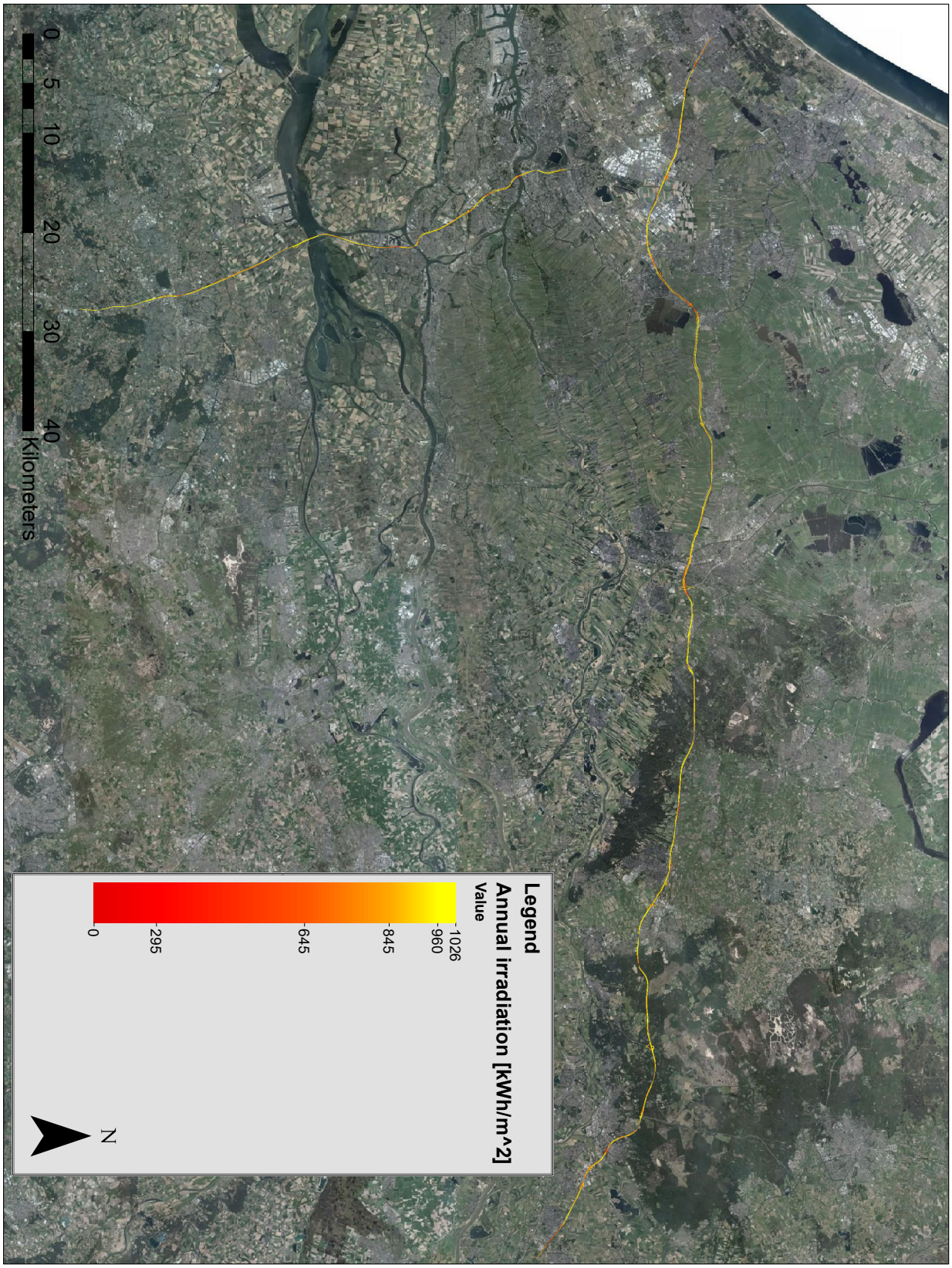

Figure D.5: Irradiation potential map for A12 and A16 after the introduction of traffic shading

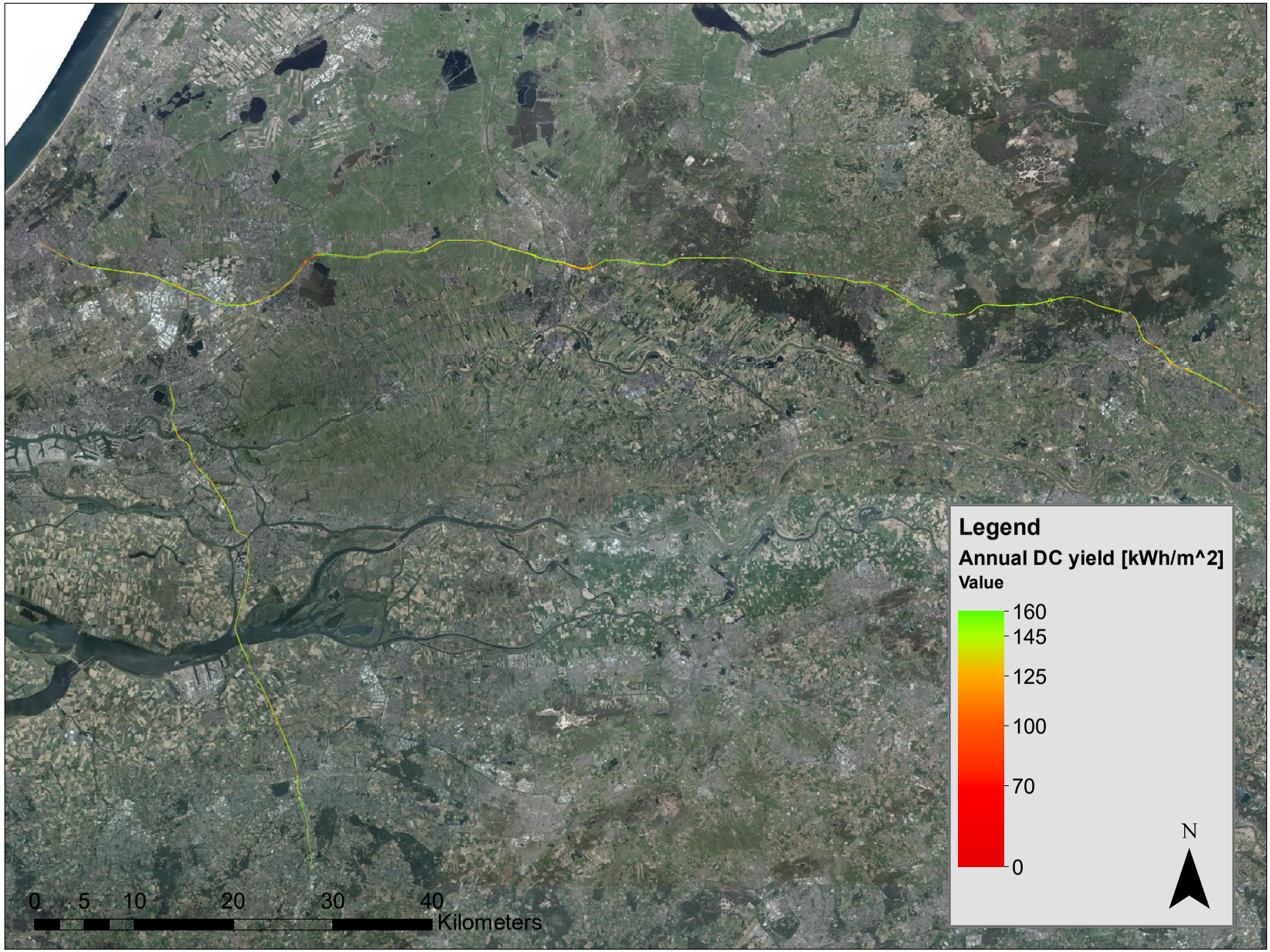

Figure D.6: DC yield potential map for A12 and A16 after the introduction of traffic shading

E

Temperature model

Table E.1 reports the assumptions made for the three PV technologies applied in the model. The modules are the ones assumed in the simulation conducted by A. Shekhar and V. Kumaravel in [19]. Table E.2 summarizes the assumptions made for the glueable technology analyzed in this research. The choice of the materials and the thickness is inspired by the solar road concept of Wattway by Colas and is based on literature review and personal communications. The glueable solar road technology assumed in the temperature model is depicted in Figure 2.4 and it is composed by the following elements:

- On the top a 2 mm ASL of silicone is placed, which is made rough by incorporated sand particles in order to recreate the skid resistance of an asphalt road. The thermal properties of the anti ASL are the ones specified in the work of V. Kumaravel [68].
- A 1.8 mm thick foil of PVC is assumed to encapsulate the PV cells and build the core of the solar road module. The thermal behavior is simulated using the thermal properties of PVC specified in the work of Y. Cengel and A. Ghajar [72].
- On the back of the modules, a 3 mm thick PVF foil is assumed, using the thermal properties of DuPont™Tedlar® (PVF) films [27].
- Eventually, a 0.3 m thick layer of asphalt is assumed, referring to the material properties given in [72].

Table E.1: Assumptions for the three PV technology simulated, where κ_T is the temperature correction factor for efficiency [20].

	Mono c-Si	**Poly c-Si**	**CIGS**
η_{eff}	20%	16%	10.5%
κ_T	-0.0035/%	-0.003/%	-0.0025/%
A_{cell} [m^2]	0.015	0.015	0.014
n_{cell}	67	67	72
$V_{OC,cell}$ [V]	0.68	0.67	0.68
V_{OC} [V/m^2]	45.3	44.7	45.3

Table E.2: Assumptions taken in the temperature model for solar road

	Absorptivity [%]	**Thermal Conductivity [W/mK]**	**d [mm]**	**Specific heat c_p [J/kgK]**	**Reference material**
ASL	0.1	0.45	2	710	Silicone
Encapsulant	0.1	0.15	1.8	842	Tedlar/PVC
Backsheet	0.1	0.15	3	1063	Tedlar/PVF
Asphalt	-	0.65	300	920	Asphalt

F

Manual

Materials on hand before starting:

- List of the roads to be processed.
- A folder for each road where you will save all the tiff/shape image and the excel files related to that road only.
- Go to pdok.nl and download the 'Hectopunten' and 'maximum Snelheiden' maps.
- MATLAB installed with the IEModel.mat file and correlated functions
- ArcMap 10.5.1 installed (or other versions). Please, make sure that you have the license for 'Spatial Analyst' and '3D Analyst'

F.1. Procedure 1 - Road cut

1. Pick up a road from the excel list of roads and colour its cells in yellow/orange. In this way, you know that someone is working on it.
2. Find the road on https://www.rijkswaterstaat.nl/wegen/wegenoverzicht/index.aspx. You need to know the exact begin and end of the road and be able to visually find them again on LiDAR.
3. Go to Pdok.nl > AHN3 > Downloads.
4. Find in the map the subunits that include the road you want to analyse.
5. For each subunit: click on it > download (choose the desired resolution. Best one: 0.5-meter raster DSM).
6. You will be asked to save the image. Choose "save as" and name the subunits with a number starting from 1 (then 2,3,4, etc).
7. Extract the zipped files and name them as well with numbers starting from 1. It is itself not relevant to maintain any spatial order of the tiff images when you enumerate them.
8. Open ArcMap 10.5.1. If you are using other versions, the names of the commands and their path given in this manual might change.
9. Add the LiDAR images from the road folder.
10. Click on the globe icon (full extent) and then zoom to the area represented by the LiDAR maps.
11. Activate the Hectopunten map and recognize the road that you want to cut.

12. Click on select features > select by polygon.
13. Select in a big area the entire road. This will help you to work with less data than the entire map of Hectopunten.
14. Right-click to Hectpunten and choose Selection > Create layer from selected features.
15. You obtain a layer with ONLY the selected points called 'Hectopunten selection'.
16. Now deselect the Hectpunten layer and leave the 'Hectopunten selection' selected.
17. Exclude the following points in your selection:
    (a) In an injection of another road to the highways you are analysing, exclude the points that are still on the other road (Figure F.1a gives an example).
    (b) When there is an underpass underwater, exclude the points that are positioned on the water (Figure F.1b gives an example).
    (c) When there is a crossing point you need to exclude the points of the road above (if your road is going below another one) or the points of the road below (if your road is going above the other one).
    (d) In general, try to include only the points that are on the same road level.

(a) (b)

Figure F.1: (a) case of an injection in which the two roads are on different level, (b) case of a water underpassage.

18. For each time you conclude a selection:
    (a) Right click on 'Hectopunten selection' > Selection > Create layers from selected features. You will have a layer called 'Hectopunten selection selection X' (X = a number)
    (b) Clear the selection and move forward to the next section.
19. In this way complete the whole road.
20. Now you have a lot of 'Hectopunten selection selection X'. You need to merge them together in one single layer. Click on ArcToolbox > Data Management > General > Merge (double click):
    (a) In Input Datasets drag all the 'Hectopunten selection selection' (NOT the 'Hectopunten selection' and NOT the Hectopunten).
    (b) Check if all the numbers are there (remember that the 1 is not there, is simply called 'Hectopunten selection selection').
    (c) In Output Dataset, change the name of the file with the name of the road.
    (d) Press OK and wait until the whole road automatically appears in the map.
21. Now you have a layer with the name of the road. Go quickly through the road again to see if you want to change something, for example, delete a point. In this case:

(a) Go to Customize > Toolbars > Editor.
(b) In the Editor Toolbar click on Editor > Start Editing.
(c) Choose the layer of the merged road and press OK then Continue.
(d) Click on the black arrow and then click on the point that you want to delete.
(e) Press the Delete button on your keyboard.
(f) In the Editor Toolbar click on Editor > Stop editing.
(g) Save the changes.

22. Now you need to save the road layer. You do it by exporting the layer as a shapefile in your server/external memory. Right-click on the road layer and press Data > Export Data > Give a name and a folder to the exported data (it will be in the format of shapefile).
23. Answer YES to the message that asks you to save the layer.
24. Now you have two roads layers with the same name. The one in the folder called Default.gdb is NOT saved in your server and you can delete it. All the layers called "selections" can also be deleted because now you merged them in one layer alone.
25. Well done! You are finished with this road. Now put the LiDAR data and the ArcGIS layer of the road in the same folder with the name of the road.
26. Go to the excel file with the list of the roads and colour the cells of the respective road in green so you will know that this road is done.

F.2. Procedure 2 - Generation of road buffer

In order to give the shape of the road to the interpolated values, a buffer that represents the road surface is needed.

1. Open ArcMap.
2. Add Data>'maximum Snelheiden' (if the layer is not already added in your ToC).
3. Choose Selection>Select by location.
4. In the list of the objects to be selected, choose 'maximum Snelheiden'.
5. As selecting objects, choose the road points of the road for which you want to create the buffer.
6. Define a search distance (suggested: not higher than 10 m). In this way, the software will select the lines of 'maximum Snelheiden' that are in a range of max the search distance from the roads points.
7. Save the layer as 'AX_line' and export the data to save it in your server (see point 14. procedure 1).
8. Go to Geoprocessing>Buffer.
9. Select the 'AX_line' and choose the width of the buffer. To represent the whole Netherlands a buffer of 200 is recommended. Otherwise, for the visualization of single roads, the Buffer can vary from 15 to 20 m, depending on the width of the road.
10. You can now choose different buffer options.
11. Save the buffer as 'AX_BufferY' (with Y = the width of the buffer. It is useful to have it written).
12. Press OK.
13. The road is now represented with its Buffer. If you want you can now save the layer on your server by exporting the data (see point 14 in procedure 1).

F.3. Procedure 3 - Extract potential and represent road output in ArcMap

1. Pick up a road and run it in the MATLAB code IEModel.mat filling the following input:
   (a) roadsname (it is the name of the road and needs to be written as a string, ex. 'A1');
   (b) numtif (it is the number of TIFF images that contain the road. They are numbered in each file of the road. Write here how many they are);
   (c) M.tech (specify the PV technology if you want to run the DC yield output as well);
   (d) climate (choose if the North or South coefficients need to be used. Write 'South' or 'North');
   (e) Change the name of the road in roads_array *(needs to be fixed to be automatic)*;
   (f) Change the name of the road in cd *(needs to be fixed to be automatic)*;
2. After you made all these changes you can RUN the code.
3. Move the generated excel file into the right folder. It will be named in the following way:
   - Irradiation excel file: ex. 'A16'
   - Poly c-Si DC yield file: ex. 'A16_poly'
   - Mono c-Si DC yield file: ex. 'A16_mono'
   - CIGS DC yield file: ex. 'A16_CIGS'
4. Open the excel file and create a new first row above the data (ADD the row, don't DELETE the first row of data). Call the first column X, the second Y and the third
   - Irr (if it is the irradiation file)
   - DC (if it is the DC yield file)

   It is very important that you name the columns, otherwise ArcMap will not recognize them.
5. Save the excel file.
6. Open ArcMap.
7. Select Add Data.
8. Find the excel file, click on it, click on 'Sheet1$' and press Add. Now the excel file is loaded on ArcMap.
9. To give this file a spatial reference, ArcMap needs to recognize the coordinates and the Z values to represent. Click on File > Add Data > Add XY Data. Choose the 'Sheet1$' and combine the X Field with the column X, the Y Field with the column Y and the Z field with
   - the column Irr if it is an irradiation file
   - the column DC if it is a DC yield file
10. Press OK. ArcMap will then probably tell you that the table does not have object ID-Field. It means that the file is just represented in the ArcMap file but is not an object yet. Press OK.
11. Now your layer is represented in the Table Of Contents and also in the map. To make your layer an object that you can modify and save, right-click on the layer and choose Data > Export Data. Choose the folder where you want to save the shapefiles of the results and name it as in point 2.
12. Answer YES when ArcMap asks you if you want to display the saved layer.

13. The new layer is now represented and is a full spatial object in ArcMap. Right-click on the old layer and remove it.
14. Right-click on the new layer and choose Properties > Symbology > Quantities > Graduated colours.
15. In the box Value choose
    - Irr (if it is the irradiation file)
    - DC (if it is the DC yield file)
16. Automatically the classification of the data will be displayed. You can change it in Classify > Method. It is important to you define the same classification for all the roads that you are going to represent. Click on Classify and choose the number of classes, colour and values for your classification.
17. Write down the statistics of the road in an excel file (you find them in the upper-right part of the Classification window). These data describe the statistics of the results for the single roads and can be very useful for the analysis.
18. Press OK and again OK. Now the road is displayed with the classification of the outputs.
19. To represent the interpolated values, go to the ArcToolbox > 3D Analyst Tools > Raster Interpolation > Natural Neighbor (or another method of your choice).
20. Give the following input:
    - Input point: layer of the road points.
    - Z value: Irr (if it is the irradiation file), DC (if it is the DC yield file).
    - Give a name to the output raster.
    - Output cell size (suggested is 30)
21. Press OK and wait. It can take some time.
22. The interpolation is now displayed on the map. To cut only the road go again to ArcToolbox > Data Management Tools > Raster > Raster Processing > Clip. Another method is to use 'Extract by Mask' but I suggest to use Clip because it is faster and also represent the roads better once you zoom out to see the whole map.
23. Give the following input:
    - Input raster: interpolation raster layer of the road.
    - Output extent: the buffer of the road (see procedure 2 to know how to create it).
    - Tick on 'Use Output Input Features for Clipping Geometry'.
    - Give a name to your output raster.
24. Press OK and wait. It can take some time.
25. The clipped road is now displayed. If you want to change colour or classification, follow step 13. For interpolated values, you should choose Stretched and then define the Type.